Toward Scalable Processing of Porous Carbon Nanocomposites and Functional Nanomaterials

Matthew B. Lim

A dissertation

submitted in partial fulfillment of the

requirements for the degree of

Doctor of Philosophy

University of Washington

2018

Reading Committee:

Peter Pauzauskie, Chair

Guozhong Cao

Devin MacKenzie

Program Authorized to Offer Degree:

Materials Science and Engineering

University of Washington

Abstract

Toward Scalable Processing of Porous Carbon Nanocomposites and Functional Nanomaterials

Matthew B. Lim

Chair of the Supervisory Committee:
Asssociate Professor Peter J. Pauzauskie
Materials Science and Engineering

Porous carbon materials, such as carbon aerogels, feature a combination of high surface area, electrical conductivity, and mechanical stability that has triggered interest in loading them with functional nanomaterials. Carbon aerogels are often derived from resorcinol–formaldehyde (RF) gels, which traditionally rely on base-catalyzed aqueous reactions that take long times at high temperatures (12+ hours, 80+°C), posing a bottleneck to scale-up. To address this issue, I present an alternative acid-catalyzed gelation process in acetonitrile, requiring just 2 hours at <45°C, en route to graphene– and transition metal dichalcogenide (TMD)–carbon aerogel composites. Both of these composites exhibit superior performance as supercapacitor electrodes versus plain carbon aerogels, and the graphene aerogel is also shown to enhance adsorption of an important lipophilic biomolecule, Coenzyme Q_{10}, for possible drug loading applications. Additionally, to explore the possibility of tailoring the microstructure of such aerogel composites, I present optoelectronic tweezers (OET) as a viable means to align, manipulate, and pattern particles of graphene oxide—the precursor to graphene in our aerogel composites—in water using low-intensity light. With an eye toward OET patterning for another important nanomaterial, I also report a simple hydrothermal synthesis to obtain large yields of palladium nanowires (PdNWs), whose ultra-high aspect ratio

greatly facilitates OET manipulation relative to more uniform geometries. Finally, going back to porous carbon composites, I take on a different approach to accelerating synthesis by investigating a solvent-free preparation of the polymer precursor based on bisphenol A and hexamethylenetetramine, which eliminates the need for time-consuming solvent exchange and supercritical drying. Beyond synthetic insights, I demonstrate that carbons produced by this approach can serve as scaffolds to stabilize nanoscale silicon for high-capacity lithium-ion battery anodes.

Table of Contents

Abstract ... 3
Table of Contents ... 5
List of Figures ... 8
List of Tables ... 13
List of Equations ... 14
Acknowledgments ... 15
Chapter 1. Introduction ... 16
1.1. Overview of Porous Carbons and Carbon Aerogels ... 16
1.2. Motivation and Outline of this Thesis ... 17
1.3. Supercapacitors ... 21
1.4. Lithium-Ion Batteries ... 23
1.5. Other Applications of Carbon Aerogel Composites ... 25
Chapter 2. Rapid Sol–Gel Synthesis of Graphene Aerogels ... 26
2.1. Introduction ... 26
2.2. Materials and Methods ... 29
2.2.1. Aerogel Synthesis ... 29
2.2.2. Microstructural and Chemical Characterization ... 30
2.2.3. Peptide Loading ... 31
2.2.4. Supercapacitor Fabrication and Testing ... 32
2.3. Results and Discussion ... 33
2.3.1. Microstructural Analysis of Pyrolyzed Aerogels ... 33
2.3.2. Spectroscopic Analysis of Aerogels Pre- and Post-Pyrolysis ... 37
2.3.3. Peptide Loading ... 43
2.3.4. Electrochemical Testing Results ... 44
2.4. Conclusion ... 48
Chapter 3. Crystalline Loading of Coenzyme Q_{10} within Graphene and Amorphous Carbon Aerogels Derived from RF Chemistry ... 50
3.1. Introduction ... 50
3.2. Materials and Methods ... 51
3.3. Results and Discussion ... 53
3.3.1. Aerogel Pore Structure ... 53
3.3.2. CoQ_{10} Loading Experiments ... 54
3.3.3. Crystallinity of the Adsorbed CoQ_{10} ... 57
3.4. Conclusion ... 58
Chapter 4. Rapid Sol–Gel Synthesis of Composite TMD–Carbon Aerogels ... 60
4.1. Introduction ... 60
4.2. Methods ... 62
4.2.1. Aerogel Synthesis ... 62

4.2.2. Microstructural and Chemical Characterization 63
4.2.3. Supercapacitor Fabrication and Testing 64
4.3. Results and Discussion 65
4.3.1. Microstructural Analysis of Pyrolyzed Aerogels 65
4.3.2. Spectroscopic Analysis 69
4.3.3. Electrochemical Testing Results 71
4.4. Conclusion 78
Chapter 5. Patterning of Graphene Oxide with Optoelectronic Tweezers 80
5.1. Introduction 80
5.2. Theory of OET 83
5.2.1. Dielectrophoresis Force 83
5.2.2. Evaluation of Clausius–Mossotti Factor 85
5.2.3. Stokes Drag Force 87
5.2.4. Other Negligible Forces 89
5.3. Experimental Methods 90
5.3.1. OET Manipulation 90
5.3.2. In-Situ Thermometry 92
5.4. Results and Discussion 93
5.4.1. Single-Particle Manipulation 93
5.4.2. Multi-Particle Manipulation 96
5.4.3. In-Situ Thermometry 98
5.5. Conclusion 100
Chapter 6. Copper- and Chloride-Mediated Synthesis and OET Trapping of Palladium Nanowires 102
6.1. Introduction 102
6.2. Materials and Methods 104
6.2.1. Synthesis 104
6.2.2. Characterization 106
6.2.3. OET Manipulation 107
6.3. Calculation of the Clausius–Mossotti Factor for a Pd Nanowire 107
6.4. Results and Discussion 111
6.4.1. Synthetic Studies 111
6.4.2. Characterization of Cu-Mediated PdNWs 115
6.4.3. OET Manipulation of Pd Nanowires 120
6.5. Conclusion 122
Chapter 7. Rapid, Solvent-Free Approach to Porous Carbons and their Nanocomposites with Silicon for Electrochemical Energy Storage 123
7.1. Introduction 123
7.2. Materials and Methods 125
7.2.1. Synthesis of Carbons and Composites 125

7.2.2. Characterization 126
7.2.3. Lithium-Ion and Supercapacitor Electrode Fabrication and Testing 127
7.3. Results and Discussion 130
7.3.1. Pore Structure 130
7.3.2. Compositional Analysis 132
7.3.3. Chemistry of Resin Curing and Pyrolysis 139
7.3.4. Lithium-Ion Anode Characterization 142
7.3.5. Supercapacitor Characterization 145
7.4. Conclusion 146
Chapter 8. Conclusions 147
References 149

List of Figures

Figure 1.1. Schematic diagram showing charging and discharging mechanism in a supercapacitor. 22

Figure 2.1. Diagram of our graphene aerogel preparation process. First, GO sheets are dispersed within acetonitrile. Resorcinol, formaldehyde, and hydrochloric acid are added to this solution, which, upon further sonication, results in rapid gelation that encapsulates the GO. This gel is washed with ethanol, dried with supercritical CO_2, and pyrolyzed in argon to form the graphene aerogel. 29

Figure 2.2. SEM images of the same location at different magnifications in a) GO-RFA-P, b) RFA-P. c) Nitrogen adsorption/desorption isotherms (pressure relative to 1 atm) for the aerogels. d) Non-localized density functional theory (NLDFT) pore size distribution plots for the aerogels. 33

Figure 2.3. Raw X-ray diffractogram of the as-received GO (top), bulk GO-RFA-P with polynomial curve representing presumed background (middle), and background-subtracted diffractogram of GO-RFA-P (bottom). 35

Figure 2.4. (a) FTIR spectra and (b) Raman spectra of the pyrolyzed and unpyrolyzed GO-RFA, along with GO for reference. Deconvoluted carbon regions of Raman spectra of (c) GO-RFA-P and (d) GO showing I, D, D″, and G bands with D-to-G peak intensity and peak area ratios. 37

Figure 2.5. C1s XPS spectrum showing deconvoluted peaks, and C/O ratios, calculated from survey spectrum, of (a) RFA-U, (b) RFA-P, (c) GO-RFA-U, (d) GO-RFA-P, (e) GO..... 41

Figure 2.6. Carbon aerogel samples immersed in sfGFP-Car15 solution (a) immediately after inserting aerogels; (b) 12 h after inserting aerogels showing loss of green color for solution containing GOA, but not for solution containing RFA. Scale bar in both images = 1 cm. 43

Figure 2.7. Coin cell testing results of the pyrolyzed GO-loaded RF aerogels and plain RF aerogels. a) Equivalent circuit diagram of the supercapacitor. b) EIS Nyquist plots (inset shows more detail of high to mid frequency range). c) Cyclic voltammograms (sweep rate 20 mV s^{-1}). d) Rate capability plot obtained from galvanostatic charge–discharge tests. Solid lines show trend in gravimetric capacitance while dashed lines show trend in areal capacitance. 45

Figure 3.1. (a) Ball-and-stick model and (b) space-filling model of CoQ_{10} showing dimethoxybenzoquinone moiety and 10 mono-unsaturated trans-isoprenoid units in the side chain. Carbon atoms are dark gray, hydrogen atoms are light gray, and oxygen atoms are red. 51

Figure 3.2. (a) Nitrogen sorption isotherms with BET surface area, and (b) BJH pore size distributions of GOA and RFA. 53

Figure 3.3. Carbon aerogel samples immersed in 1 mg mL^{-1} CoQ_{10}/acetonitrile solution (~5 mg of aerogel in 3 mL of solution) (a) immediately after inserting aerogels; (b) 12 h after inserting aerogels showing lightening of bulk solution. (c) UV-vis spectrum of GOA over 12 h in 0.1 mg mL^{-1} CoQ_{10} solution showing decrease in intensity of absorption band centered at 273 nm. (d) Plot of sorption capacity of CoQ_{10} in aerogels over time as derived from UV-vis measurements. 54

Figure 3.4. Pseudo first-order and pseudo second-order kinetic fits for CoQ_{10} adsorption on (a, b) GOA and (c, d) RFA..... 56

Figure 3.5. XRD patterns of as-received CoQ_{10} powder and carbon aerogels. Inset shows full intensity scale of CoQ_{10} diffraction pattern for same range of 2θ (10–50°). For aerogels, solid lines denote aerogels loaded with CoQ_{10} and dotted lines denote their unloaded counterparts. .. 57

Figure 4.1. Outline of the synthetic process for composite TMD carbon aerogels. a) Initially, sonication driven cavitation drives TMD sheets apart and enhances dispersion within acetonitrile. Resorcinol, formaldehyde, and hydrochloric acid are added to this solution, which causes rapid sol-gel formation upon further sonication. b) This gel is washed with ethanol, dried with supercritical CO_2, and pyrolyzed in argon. c) Finally, the material is processed into a supercapacitor by grinding it with carbon black additive (Ketjenblack) and PTFE tape, rolling and punching it into electrodes that are assembled into a symmetric coin cell with a cellulose separator. e) 3D X-ray computed tomography image of a coin cell after 10,000 charge–discharge cycles. 62

Figure 4.2. TEM images of MA-17 (a, b), WA-17 (c, d), and RFA (e, f). Panels e and f are characteristic of the gels as synthesized, while panels a, b, c, and d demonstrate the presence of exfoliated sheets. Insets in the TEM images (a and c) show electron diffraction of the TMD sheets dispersed in the aerogel. 66

Figure 4.3. XRD patterns of MA-17 and WA-17. Vertical solid lines show the corresponding XRD peaks and relative intensities of 2H-MoS_2 and 2H-WS_2 from the International Centre for Diffraction Data cards. 67

Figure 4.4. a) Nitrogen sorption isotherms with BET surface area and b) BJH pore size distribution of pyrolyzed aerogel with different mass loadings of TMD. 68

Figure 4.5. a) FTIR transmittance data of MA-17 and WA-17. b) Low-resolution Raman spectrum of WA-17. (c, d) Higher-resolution Raman spectra showing characteristic bands of MoS_2 (c) and WS_2 (d) dispersed within the carbonized RF matrix of the aerogel for samples synthesized from 17 mg mL^{-1} TMD dispersions. For each RF-supported TMD, the bulk Raman spectra is displayed offset for comparison. Vertical dotted lines represent peak centers of the in plane (E^1_{2g}) and out of plane (A_{1g}) modes of the exfoliated TMD's to emphasize the shift from their bulk counterparts due to exfoliation. 70

Figure 4.6. Electrochemical characterization of the pyrolyzed aerogels with different TMD mass loadings fabricated into coin cell supercapacitors, including a) equivalent circuit diagram, b) Nyquist plots from EIS (inset shows more detail of high–mid frequency range), c) cyclic voltammograms at sweep rate 20 mV s^{-1}, and d) specific volumetric capacitance as a function of applied current density from galvanostatic tests. 73

Figure 5.1. Schematic diagram of an optoelectronic tweezers (OET) device. 81

Figure 5.2. a) Simulation of the electric field E (arrows) and ∇E^2 (color plot) in the GO suspension near the OET substrate for an applied bias of 7 V_{pp}, 500 kHz and an illuminated region 5.8 μm in diameter. b) Calculated values of the real Clausius–Mossotti factor of GO in water at 500 kHz for a range of particle thicknesses and diameters. 85

Figure 5.3. Trapping and translation of a single GO particle. The location of the laser spot used as the trap is indicated by the solid circle. a) No bias is applied to the OET device and the particle is in Brownian motion. b) Voltage (5 V_{pp}, 500 kHz) is turned on and the basal plane aligns with the electric field. c) HeNe laser is moved close to particle to induce trapping. d) The particle has fallen into the trap, and, e) follows the light as it is moved down in the field of view. (scale bar in each panel = 5 μm) 93

Figure 5.4. Maximum trapping speed of GO particles at different voltages at 500 kHz. Solid lines denote experimentally measured values while dashed lines denote theoretical maximum speeds based on DEP and drag force analysis. Insets show optical microscope images of each particle with circumscribing circle and diameter above (scale bar = 10 μm). 94

Figure 5.5. Multi-particle aggregation. (a) A bias (20 V_{pp}, 500 kHz) is applied to the OET device and a focused laser beam creates a trap. (b) In less than one minute, all the nearby GO particles are trapped in the spot (scale bar = 10 μm). (c) Raman spectrum of GO suspension in OET device with (blue) and without (black, green) bias of 20 V_{pp}, 500 kHz. 97

Figure 5.6. Large-scale patterning of GO with a digital projector. a) An array of four illuminated dots in projected onto the suspension. b) Bias of 20 V_{pp}, 100 kHz is applied, GO aligns with the electric field, and each dot traps nearby particles, which follow the dots as they are slowly moved closer together. c) The dots have converged and the particles are now locally aggregated. 98

Figure 5.7. Thermometry of GO suspension in OET device with $NaYF_4:Yb^{3+},Er^{3+}$ nanocrystals. a) Plot of $\ln(R1/R2)$ as a function of applied voltage (frequency = 500 kHz). b) Calibration data collected with temperature-controlled sample chamber from room temperature (23.6°C)–50°C.98

Figure 5.8. Steady-state temperature plot of OET device obtained from finite-element simulations, at level of a-Si:H surface, illuminated with HeNe laser (power 3.49 μW, spot diameter 5.8 μm) at bias of 13 V_{pp}, 500 kHz. 100

Figure 6.1. Calculated values of the real Clausius–Mossotti factor ($Re(f^*_{CM})$) of a Pd nanowire in water at 500 kHz for a range of particle lengths and diameters. 110

Figure 6.2. SEM images of hydrothermally synthesized Pd nanoparticles (a) without additives, with MW 29000 PVP, for 2 h; (b) without additives, with MW 29000 PVP, for 6 h; (c) with $Cu(OAc)_2$ and MW 29000 PVP for 6 h; (d) with CuSO4 and MW 29000 PVP for 6 h; (e) with NaCl, $Cu(OAc)_2$, and MW 55000 PVP for 2 h; (f) with only NaCl and MW 55000 PVP for 2 h; (g) with Cu(OAc)2, NaCl, and MW 29000 PVP for 2 h. Scale bar = 1 μm (a–f); 500 nm (g). (h) Schematic of ideal PdNW with penta-twinned cross-section, <011> growth direction, and surface coating. 111

Figure 6.3. Cu Kα XRD pattern of PdNWs synthesized with $Cu(OAc)_2$ and MW 29000 PVP for 6 h. Si (111) peak is from the silicon wafer on which the nanowires were deposited. 115

Figure 6.4. Bright field TEM images of (a) an aggregate of PdNWs; (b) a single PdNW. (c) Enlarged and rotated image of area outlined in (b), showing lattice fringes and moiré pattern. (d) FFT of (c). (e) Background-subtracted SAED pattern (left) with integrated intensities (right) of a cluster of PdNWs. 117

Figure 6.5. (a) XPS survey spectrum of oxygen plasma-treated PdNW dispersion on Si substrate. $I3p_{1/2}$ binding energy at 932 eV overlaps with potential $Cu2p_{3/2}$ peak (inset). (b) High-resolution XPS spectrum of Pd3p (left) and Pd3d (right) regions with deconvoluted peaks. 118

Figure 6.6. Trapping and translation of a single PdNW in water with OET. Arrows indicate the location of the nanowire, and the circular outline indicates the location of the laser spot used as the trap. a) No applied bias, nanowire is in Brownian motion. b) Voltage (5 V_{pp}, 500 kHz) is turned on, axis of the nanowire aligns with the electric field, and it moves toward the trap. c) The nanowire has fallen into the trap. d) The nanowire follows the position of the trap as the trap is moved right. 120

Figure 6.7. Aggregation of PdNWs in water with OET. (a) An illuminated circle ~86 μm in diameter is projected onto the OET device using an ordinary digital projector. (b) PdNW suspension before illumination and application of bias. (c) PdNW suspension after illumination and application of 20 V_{pp}, 500 kHz bias for 5 min (bias off and projected image removed). 121

Figure 7.1. (a) Pore size distributions for the carbon scaffolds from nitrogen sorption. Particle size distributions for (b) BHC and BHC-S and (c) BHAGC and BHAGC-S, obtained from laser scattering measurements. 130

Figure 7.2. SEM-EDS characterization of carbons and composites. SEM image with corresponding elemental maps of C, Si, and O for (a) BHC-S, (b) BHAGC-S. (c) Lower-magnification SEM image with elemental maps of P, Al, and N for BHAGC-S. Arrow labeled '1' denotes a region of concentrated P, Al, and N that is quantified in Table 7.2. 132

Figure 7.3. (a) XRD patterns of carbons and composites. Bright-field TEM images of (b) BHC, (c) BHC-S, (d) BHAGC with inset showing embedded graphite with interlayer spacing of 0.34 nm, (e) BHAGC-S. 134

Figure 7.4. Raman spectra of carbons, composites, and 4124 graphite additive with deconvoluted carbon regions showing I, D, D″, and G bands. 136

Figure 7.5. Baseline-corrected FTIR absorbance spectra of carbons and composites..... 138

Figure 7.6. (a) TGA weight loss curve of a BPA-HMT resin (3:2 molar ratio) from heating to 950°C at 15.8°C/min under CO_2. (b) FTIR spectra of 3:2 BPA-HMT mixture prior to curing, after curing, and after heating the cured resin to 250°C, 350°C, and 600°C at the same ramp rate under CO_2..... 140

Figure 7.7. Lithium-ion half-cell performance of composites. (a) Reversible delithiation capacity (solid lines) and Coulombic efficiency (dashed lines) versus cycle plot. (b) Capacity retention versus cycle plot. Differential capacity plots at selected cycles for (c) BHAGC-S and (d) BHC-S. 142

Figure 7.8. Supercapacitor performance of BHC. (a) Gravimetric capacitance as a function of applied current density from galvanostatic tests. (b) Cyclic voltammogram at sweep rate 20 mV/s. 145

List of Tables

Table 3.1. Kinetic Parameters for CoQ_{10} Adsorption on Aerogels..... 56

Table 4.1. Summary of pyrolyzed TMD aerogel composite properties. 78

Table 6.1. Summary of hydrothermally synthesized 1D Pd nanostructures. Particle dimensions were measured from SEM images with sample size = 50 particles..... 111

Table 7.1. Specific surface area and pore volume of carbons and Si–C composites..... 130

Table 7.2. Elemental quantifications from EDS of carbons and composites..... 132

List of Equations

(2.1) 36

(2.2) 39

(2.3) 44

(2.4) 47

(3.1) 55

(3.2) 55

(3.3) 55

(5.1) 83

(5.2) 84

(5.3) 84

(5.4) 84

(5.5) 86

(5.6) 86

(5.7) 86

(5.8) 86

(5.9) 88

(5.10) 89

(5.11) 90

(6.1) 107

(6.2) 107

(6.3) 108

(6.4) 109

Acknowledgments

First, I thank my advisor, Peter Pauzauskie, for his valuable advice and guidance throughout my graduate studies at UW. His intellectual curiosity and enthusiasm for research are admirable. I also want to thank my fellow members in Pauzauskie Group, past and present, for their consistent support of me (particularly during this trying time of thesis preparation!), assistance with the research efforts described herein, keen insight, and just being fun people to talk to in general. Additionally, I gratefully acknowledge EnerG2 and Group14 Technologies—particularly Aaron Feaver, Leah Riley, and Rick Costantino—for giving me valuable opportunities to perform research in an industrial setting through internships and collaborations, which, among other things, have opened my eyes to practical constraints and challenges of materials design. I am also indebted to the UW Clean Energy Institute for partial financial support of my graduate studies through a CEI Graduate Fellowship. Finally, I would like to thank the rest of my supervisory committee members for all their constructive input on my studies, and of course, my family for their unwavering devotion, and love for me throughout my nearly 27 years of existence.

Chapter 1. Introduction

1.1. Overview of Porous Carbons and Carbon Aerogels

High-surface-area, porous carbon materials have been studied extensively in the scientific literature. Such materials not only feature exceptionally high surface area, which can be well over 1000 $m^2 g^{-1}$, but also hydrophobicity and high electrical conductivity, making them useful for such diverse applications as gas separation and storage,[1] water purification through adsorption or capacitive deionization,[2,3] catalyst supports,[4] electrochemical energy storage,[5] and drug delivery.[6] Typically, porous carbons are produced by a bottom-up approach, where an organic polymeric or biomass precursor is pyrolyzed at high temperatures (>600°C) in an inert environment to carbonize the material. The precursor itself may be porous, or the precursor may be "activated" to promote extensive pore formation—either by impregnation of the precursor with chemicals such as strong acids prior to pyrolysis, or by subjecting the material to steam or carbon dioxide at high temperatures during or after pyrolysis.[7]

Carbon aerogels are one type of porous carbon, and are formed by carbonization of a porous polymeric aerogel. In turn, this polymeric aerogel is obtained from supercritical drying of a polymeric gel, in which the gel is loaded into a high-pressure autoclave and soaked in a fluid (usually liquid CO_2), which is then brought past its critical point to become a supercritical fluid, and finally vented off. Since supercritical fluids have no surface tension, this technique allows the liquid component of the gel to be extracted while avoiding capillary forces that would normally cause the porous solid matrix of the gel to collapse under ambient drying conditions. Thus, the resulting solid has a very low bulk density, high surface area, and high pore volume. Pyrolysis of this polymeric aerogel drives off oxygen moieties, carbonizing the material and opening up additional pores, yielding the carbon aerogel.

Although several different polymerization strategies exist for aerogels, this thesis predominantly explores resorcinol–formaldehyde (RF) sol–gel chemistry. This method has been especially popular among researchers, given the large porosity (>80%), large specific surface area (SSA, 400–1200 $m^2 g^{-1}$), high electrical conductivity (25–100 S cm^{-1}), low thermal conductivity (~0.03 W $m^{-1} K^{-1}$), low density, and mechanical strength of the resulting carbons, as well as the ease of tailoring these properties based on reagent concentrations.[8–11] First demonstrated for aerogel synthesis by Pekala in 1989,[12] resorcinol and formaldehyde in the presence of a basic catalyst (typically Na_2CO_3) in water undergo an addition–condensation reaction. More specifically, under the basic conditions, resorcinol is deprotonated to the resorcinol anion, and electron donation from the 4 and 6 ring positions to the carbon of formaldehyde leads to addition of hydroxymethyl groups (–CH_2OH) to the aromatic ring.[13] Condensation then proceeds via H^+, which causes the hydroxymethyl derivative to lose its OH group to form a benzylic carbocation, which in turn undergoes an electrophilic reaction with another aromatic ring or hydroxymethyl group to form methylene or methylene ether bridges respectively.[14] Successive reactions initially form highly cross-linked clusters of the polymer, 7–10 nm in diameter, which then aggregate to form a stiff, pearl string-like network that eventually fills the solution volume to become a monolithic gel.[9]

1.2. Motivation and Outline of this Thesis

While carbon aerogels derived from RF alone have many potential applications, there is also strong interest in combining them with various functional nanomaterials to create porous carbon nanocomposites for added versatility. Dispersing such materials throughout the porous aerogel matrix can be a way to use them in nanoparticulate rather than bulk form, which maximizes their interfacial area and may also be desired in light of the size and shape dependence of material

properties at the nanoscale. Moreover, the carbon aerogel can act as a high-surface-area, electrically conductive, and mechanically robust support for the nanomaterials, which is desirable for energy storage and catalytic applications, where a large number of active sites and fast charge transport is needed, especially when the nanomaterial is not inherently conductive. In addition, for sorption applications, carbon aerogels are already useful because of their high porosity and hydrophobicity, but they could be further decorated with nanoparticles to target specific pollutant species. As another example, the same approach could be applied for drug loading applications to increase the affinity of the aerogel for a particular pharmaceutical or improve biocompatibility.

In principle, such porous carbon nanocomposites can be made relatively easily. One way is to disperse the nanomaterial additive of interest with the RF precursor solution such that it is effectively cross-linked into the polymer matrix and uniformly distributed throughout the gel. The additive-containing gel can then be supercritically dried and pyrolyzed as usual. Alternatively, for materials that are less thermally stable, a standard RF carbon aerogel can be made first, and the additive can be bound to the aerogel through solution-phase impregnation and subsequent drying.

Either way, however, standard synthesis protocols for RF gels, using alkaline catalysts in water, require long times at elevated temperatures: Zhang et al. used an overnight cure at 120°C,[15] Worsley et al. used a 12–72 hour cure at 85°C,[16] while the original process as introduced by Pekala stipulates even longer gelation times of up to 7 days at 85°C.[12] These requirements greatly inhibit the economical scalability and commercial potential of RF aerogels and RF-derived carbon aerogels. Moreover, even if gel formation times are shortened, the need for supercritical drying remains, which is itself is a time-consuming procedure, as it can take several days for the liquid CO_2 to penetrate fully into the pores of the gel, depending on its size. Also, the costs associated with liquid CO_2 and the pressure vessel for large volumes can be prohibitive.

Besides synthetic time and cost concerns, loading porous carbons with nanomaterial additives by simple mixing with the polymer precursors or solution-phase impregnation, does not allow for any control over the orientation and arrangement of the nanomaterial particles within the polymer or carbon matrix. Such capability would be particularly important for anisotropic nanomaterials that may have better properties for a desired application along one direction or surface over another, and would allow for creation of "textured" nanocomposites with superior performance relative to nanocomposites with randomly oriented additive particles. Even for isotropic nanomaterials, precise positioning would enable tailoring of species transport within the pores of the composite, which would be useful for catalytic and energy storage applications.

Against this backdrop, the overarching goal behind my thesis research was to investigate ways to improve the processing of porous carbon nanocomposites and the functional nanomaterials that can be incorporated into them. First, to address the problem of long gelation times, I employ a unique alternative approach to RF polymerization with hydrochloric acid as the catalyst and acetonitrile (CH_3CN) rather than water as the solvent. This method was introduced in 2007 by Mulik and Leventis,[17] who reported that gels could form within only 10 minutes at 80°C, or 2 hours at room temperature, with the final RF aerogels chemically indistinguishable from base-catalyzed samples. The significant acceleration of the process stems from increasing the electrophilicity of formaldehyde by the addition of HCl, rather than increasing the electron-donating ability of the aromatic ring substituents as in the base-catalyzed route; furthermore, the use of acetonitrile prevents cross-aldol condensation equilibria that would otherwise slow the reaction.[17]

Building on this promising finding, my research shows the rapid production and characterization of carbon aerogel composites from RF precursors with functional nanomaterial

additives, using this acid-catalyzed technique. Chapter 2 focuses on graphene-loaded aerogels obtained by dispersing graphene oxide (GO) in acetonitrile and adding the RF precursors, followed by pyrolysis of the dried aerogel to reduce the GO to graphene sheets. These aerogels are evaluated as supercapacitor electrodes, showing a marked improvement in rate capability compared to electrodes made from additive-free RF carbon aerogels. Chapter 3 demonstrates the versatility of the graphene aerogels by studying them as a host material for an important lipophilic biomolecule, Coenzyme Q_{10}, via solution-phase adsorption. Chapter 4 goes back to supercapacitor applications, but examining aerogels loaded with nanosheets of transition metal dichalcogenides (TMDs), specifically WS_2 and MoS_2, which are shown to improve the capacitance per unit volume. Beyond synthesis and electrochemical testing, the physical and chemical makeup of the TMD- and graphene-loaded aerogels is probed extensively.

As a possible means for patterning these nanomaterials within an RF gel *in situ*, Chapter 5 introduces and demonstrates optoelectronic tweezers (OET) on graphene oxide. OET is a dielectrophoresis-based, non-contact technique to manipulate particles in liquids using focused light. The light intensity requirements are low enough that particles can be manipulated with light from a digital projector, making it simple to pattern them over a large scale. In addition, as a dielectrophoresis-based technique, OET causes anisotropic particles such as GO to align in bulk.

To explore another important nanomaterial that could be patterned with OET and integrated into a carbon aerogel in future work, Chapter 6 covers a hydrothermal method to synthesize large yields of palladium nanowires (PdNWs). Palladium is widely used as a hydrogen sensing and storage medium, and as a heterogeneous catalyst for industrially valuable processes. The nanowires reported here feature the highest aspect ratios yet reported for solution-grown palladium nanocrystals, greatly facilitating their manipulation with OET, as we also demonstrate.

Finally, Chapter 7 returns to porous carbons, but addressing the issue of scalable processing by an alternative avenue. Instead of accelerating the polymer formation time, the need for drying is eliminated altogether by employing the solvent-free polymerization of bisphenol A (BPA) with hexamethylenetetramine (HMT). In addition to examining the chemical changes behind curing and pyrolysis with this system, I show that porous carbons produced from BPA-HMT precursors can serve as good supercapacitor electrodes, similar to the RF carbon aerogels, and that they can be combined with nanoscale silicon to form a composite anode for lithium-ion batteries with high capacity and rate capability.

The following three sections present some background information on the energy storage applications of the porous carbon nanocomposites studied in this thesis, as well as their other notable applications not covered herein.

1.3. Supercapacitors

Supercapacitors are rechargeable electrochemical energy storage devices that share characteristics with both batteries and conventional capacitors. Supercapacitors, like batteries, consist of two parallel electrodes that are separated by an electrolyte solution. But in contrast to batteries, which store energy through redox reactions in the electrode bulk, supercapacitors store energy electrostatically, like conventional capacitors. During charging of a supercapacitor, when a voltage is applied across the two electrodes, ions in the electrolyte will migrate toward the electrode of opposite polarity, forming electrical double-layer structures at the interface with each electrode (Figure 1.1). Because the potential drop is largely confined to this narrow region, which ranges from 0.1 to 10 nm thick, the corresponding electric field strength is in the thousands of kV per mm, allowing supercapacitors to store up to 10000 times more charge per unit mass than conventional electrolytic capacitors.[18] Compared to batteries, supercapacitors still have inferior

charge storage capability—energy density < 10 Wh/kg versus ~150 Wh/kg for lithium-ion batteries[19]—but 2–3 orders of magnitude greater power as well as practically unlimited cycle life, since they do not face the performance-limiting factors of reaction kinetics, ion transport through bulk electrode material, and accompanying volume changes that are characteristic of batteries.[20] These properties make supercapacitors useful for repetitive pulse-power applications, such as cold engine startup and laser power supplies.

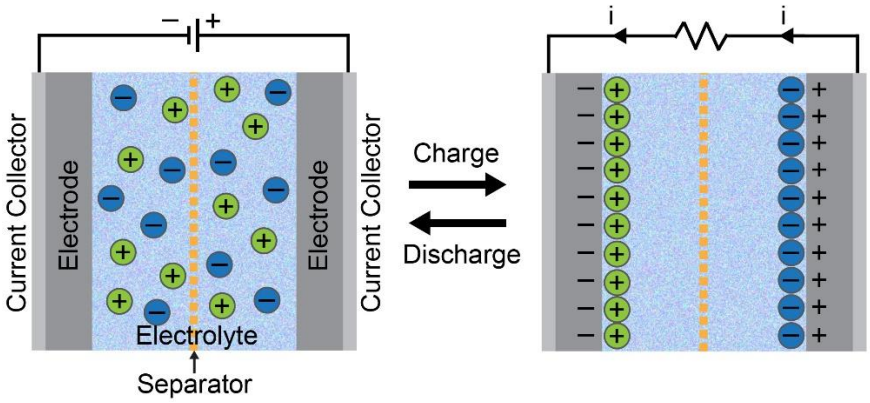

Figure 1.1. Schematic diagram showing charging and discharging mechanism in a supercapacitor.

Considering the operating principle of a supercapacitor, its capacity is largely a function of its electrodes' interfacial area, making carbon aerogels are well-suited for such an application. Furthermore, the interconnected pore structure and high electrical conductivity of carbon aerogels impart good rate capability by enabling facile ionic and electronic transport respectively. Numerous reports have been published to date evaluating RF-based carbon aerogels for supercapacitor electrodes, and studying the effect of precursor concentrations and pyrolysis temperature.[21–24] For example, Li et al. used Na_2CO_3-catalyzed as the RF polymerization catalyst and a resorcinol to catalyst molar ratio of 1500 to prepare carbon aerogels with specific capacitance as high as 184 F/g, low electrical resistance of 0.3 Ω, and small current leakage of 0.17 mA.[21]

Going off the positive results achieved with RF-based carbon alone, more recent research has focused on creating composites of RF carbon with various nanomaterials, such as

graphene,[25,26] carbon nanotubes,[27] manganese oxide,[28] and ruthenium oxide,[29] to further increase electrical conductivity, power capability, and specific capacitance. Manganese and ruthenium oxides, for example, can enhance capacitance via pseudocapacitance, whereby they participate in rapid, reversible redox reactions with adsorbed electrolyte ions.[30,31] This work focuses on loading RF carbon aerogels with two-dimensional nanomaterials—graphene and transition metal dichalcogenides (TMDs)—to enhance their supercapacitor performance. The unique properties of these materials that lend themselves to supercapacitor applications are discussed in the introductions to Chapters 2 and 4.

1.4. Lithium-Ion Batteries

Lithium-ion batteries, in contrast to supercapacitors, work by the movement of lithium ions that undergo chemical intercalation at each electrode, meaning that they reversibly insert into each electrode and undergo redox reactions that result in structural changes in the electrode material. During discharge, the anode is oxidized and Li ions are released into the electrolyte. Electrons travel through the external circuit and the Li ions travel through the electrolyte toward the cathode, where reduction occurs and the Li intercalates. The reverse processes occur when the battery is charged. Considering this mechanism, the charge and discharge rates of a lithium-ion battery are limited by diffusion of lithium through the host material and reaction kinetics, although the amount of charge that can be stored per unit mass is typically far greater than in a supercapacitor due to the formation of chemical compounds with lithium. Also, the lifespan of batteries tends to be shorter than supercapacitors owing to side reactions that can irreversibly consume lithium and degrade the electrode with repeated charge–discharge cycling.

The most common anode material in commercial lithium-ion batteries is graphite, which has a theoretical gravimetric capacity of 372 mAh/g. However, silicon has gained considerable

attention as a next-generation anode material due to its nearly 10-fold higher theoretical capacity of 3580 mAh/g.[32] Unfortunately, bulk silicon experiences large volume changes over 300% during lithiation, leading to capacity fade and failure through cracking and/or delamination.[32] Furthermore, the low electronic conductivity of silicon limits the power density of the system. Mechanical degradation can be mitigated by reducing the size of the silicon to the nanoscale, as it has been found that crystalline silicon particles with diameter below ~150 nm can withstand the strain at complete lithiation without fracturing; for amorphous silicon, this size limit can be as large as 870 nm.[33,34] Thus, one alternative electrode architecture, which is pursued in this thesis, is to disperse nanoscale silicon within a porous carbon matrix. The large pore volume allows for incorporation of large amounts of silicon, while accommodating the lithiation-induced expansion with minimal stress. In addition, the carbon matrix is interconnected and electrically conductive, allowing for rapid charge transport.

Numerous approaches to synthesize such a silicon–porous carbon nanocomposite have been reported, several of which use phenolic resins, e.g. RF, as the carbon source. Xu et al., in particular, polymerized RF in a dispersion of silicon nanoparticles, along with a triblock copolymer that self-assembled with the RF polymer and served as a sacrificial template during subsequent pyrolysis to form a mesoporous structure surrounding the silicon.[35] Wang et al. reported a similar soft-templating method, but employing a phenol–formaldehyde resin.[36] In another method, Wang et al. used a macro/meso-porous silica monolith as a hard-template for phenol–formaldehyde polymerization; the composite was then carbonized, the silica etched away with HF, and the mesopores filled with silicon by chemical vapor deposition of diiodosilane.[37] The composites studied herein are also made through a silane decomposition process onto the porous carbon, but,

as mentioned earlier, using a different phenolic resin based on bisphenol A and hexamethylenetetramine as the carbon precursor.

1.5. Other Applications of Carbon Aerogel Composites

The need for porous, mechanically robust, and electrically conductive supports is not limited to energy storage devices, and has led to a broader interest in loading carbon aerogels with functional nanomaterials. As one example, the superhydrophobicity of graphene sheets (water contact angle of 155°) can be combined with the large pore volume and thermal stability of carbon aerogels to create recyclable sorbents for oil and organic solvents, which could prove useful for environmental contaminant cleanup.[38,39] Such aerogels can be further decorated with nanoparticles to target specific pollutant species, such as α-FeOOH for arsenic removal and Fe_3O_4 for phosphate removal.[40,41]

Additionally, carbon aerogels provide ideal supports for electrocatalysis given their large interfacial surface area yielding numerous active sites, electrically conductive network, and chemical stability. Abdelwahab et al. investigated cobalt-doped carbon aerogels as cathodes for the reduction of CO_2 to hydrocarbons, noting that they had better faradaic efficiency than cobalt sheet despite containing a significantly lower amount of cobalt.[42] In another report, transition metals incoporated into a carbon aerogel were noted to catalyze the photodegradation of 1,3,6-naphthalentrisulfonic acid (NTS) without altering the textural and chemical properties of the aerogel, making it promising candidate for water purification.[43] TiO_2, a well-known photoactive material, has also been loaded into RF-based aerogels, exhibiting rapid and efficient photocatalytic decomposition of phenol and methylene blue from aqueous solution.[44]

Chapter 2. Rapid Sol–Gel Synthesis of Graphene Aerogels[1]

2.1. Introduction

Graphene, a two-dimensional (2D) structure of carbon atoms bonded in a hexagonal lattice, has attracted considerable attention within the scientific community for its outstanding properties, including its electrical and thermal conductivity (1738 S m^{-1} and ~$5 \cdot 10^3$ W m^{-1} K^{-1} respectively),[45–48] intrinsic carrier mobility (>$2 \cdot 10^5$ cm^2 V^{-1} s^{-1}),[49,50] theoretical surface area (~2600 m^2 g^{-1}),[51] mechanical strength (~118 GPa), and elastic modulus (~1 TPa).[52] A three-dimensional (3D) graphene assembly with properties that approach those of the individual 2D sheets would significantly expand the usability of this remarkable material, but its realization has proven to be a challenge. In early studies, such a structure was derived from an aqueous dispersion of graphene oxide (GO), an oxidized and exfoliated derivative of graphite that is colloidally stable in water. This dispersion can be chemically reduced and dried, or dried and thermally reduced, to form a physisorbed graphene macroassembly, held together by van der Waals forces.[53–55] Owing to the weak nature of these bonds, however, the electrical conductivity, stiffness, and surface area of these materials are vastly inferior to graphene sheets.

Covalently bonded graphene assemblies offer comparatively higher electrical conductivity and Young's modulus, but are not as well studied. Chen et al. used chemical vapor deposition of methane onto a sacrificial nickel foam template,[56] and Li et al. grafted alkylsilanes with pyrrole onto GO, followed by free radical polymerization and hydrothermal reduction.[57] However, the former process is wasteful and challenging to make into a form factor other than a thin sheet due to limitations in vapor transport, whereas the latter process requires relatively expensive chemicals

[1] This chapter is based on "Ultrafast sol–gel synthesis of graphene aerogel materials", published in *Carbon* **95**, 616-624 (2015) by Matthew B. Lim, Matthew Hu, Sandeep Manandhar, Avery Sakshaug, Adam Strong, Leah Riley, and Peter J. Pauzauskie.

and the hydrothermal process is not readily scalable. As an alternative route, Worsley et al. showed that aqueous GO suspensions can be covalently cross-linked by means of resorcinol–formaldehyde (RF) sol-gel chemistry.[16,58] After pyrolysis to remove the oxygen groups, the carbon aerogel featured a sp^2-crosslinked graphene network, maintaining a high surface area of ~600 m^2/g and bulk electrical conductivity more than two orders of magnitude higher than previously reported graphene assemblies.

This so-called "graphene aerogel" lends itself to diverse potential uses that harness the ultra-porous character of the polymeric skeleton in tandem with the properties of graphene. As previously mentioned, RF-based aerogels have already been studied extensively as supercapacitor electrodes,[15,21–24,59–61] and the conductive graphene network would further minimize series resistance as well as enhance specific capacitance beyond that contributed from the highly porous aerogel microstructure. This is due to the extremely high surface area of graphene itself, ~2600 $m^2\ g^{-1}$, which corresponds to a theoretical capacitance as high as ~550 F g^{-1}.[48] Beyond supercapacitors, graphene aerogel is a promising candidate for counter electrodes in dye-sensitized solar cells because of its good catalytic activity toward the reduction of tri-iodide ions, chemical and environmental stability, high specific surface area providing numerous active sites for the reduction reaction, and large pore volume enabling rapid mass transport of the redox species.[62,63] The latter three of these properties also make graphene aerogel a material of interest for electrocatalyst supports for the oxygen reduction reaction in fuel cells. The use of GO as a precursor offers a secondary benefit for this purpose by enabling strong adhesion with oxide catalyst nanoparticles, owing to the oxygenated functional groups of GO.[64] Finally, beyond energy-related applications, graphene aerogel is of interest as an adsorbent for oils and other non-polar liquids, owing to the superhydrophobic nature of the graphene sheets.

In light of a previous report that GO forms a stable colloidal dispersion in acetonitrile,[65] we sought to rapidly synthesize graphene aerogels adapting the method of Mulik and colleagues, as described earlier.[17] The gel preparation process, described in detail in Section 2.2.1, hinges on sonication of the GO–acetonitrile dispersion, followed by a second sonication after addition of the RF–catalyst reaction mixture, to achieve the rapid gelation. Self-supporting, monolithic wet GO–RF gels were obtained within only 2 hours at near-ambient conditions, with no external heat input apart from the minimal heat generated by the ultrasonic waves, which represents a major step toward scalable and cost-effective production of graphene aerogels. Following synthesis and carbonization of both plain RF aerogels (RFA) and GO-loaded RF aerogels (GO-RFA), we characterized their microstructure and chemical composition, and confirmed the strong presence of graphitic material in the carbonized GO-RFA with X-ray diffraction along with a unique peptide adsorption experiment. In addition, to illustrate a potential application of the carbonized aerogels, we tested their performance as electrodes for coin-cell supercapacitors. In line with expectations of the positive effect of graphene on electrochemical properties, the carbonized GO-loaded aerogels exhibit 25% greater areal capacitance, higher rate capability, and lower operational resistive components than their plain RF counterparts, indicating that our time-efficient synthesis of such materials could enhance the affordability of high-power energy storage.

2.2. Materials and Methods

2.2.1. Aerogel Synthesis

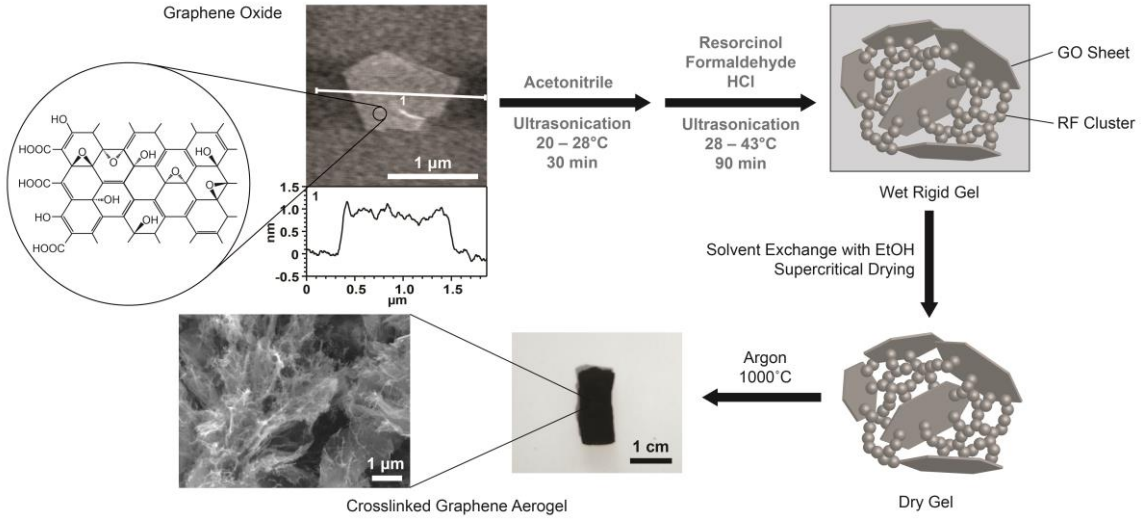

Figure 2.1. Diagram of our graphene aerogel preparation process. First, GO sheets are dispersed within acetonitrile. Resorcinol, formaldehyde, and hydrochloric acid are added to this solution, which, upon further sonication, results in rapid gelation that encapsulates the GO. This gel is washed with ethanol, dried with supercritical CO_2, and pyrolyzed in argon to form the graphene aerogel.

Our procedure for making graphene aerogels is outlined in Figure 2.1. For the GO-RFA, commercially obtained multilayer GO (Cheap Tubes Inc., 2–4 layers, total thickness < 3 nm) was suspended in acetonitrile (AN) in the desired concentration and dispersed by sonication at ambient conditions for 30 minutes using a bath sonicator with power of 70 W and frequency of ~42 kHz. For the RFA, this step was omitted. Although the sonicator was initially at room temperature, the energy of the ultrasonic waves caused the bath to heat up gradually from 20° to 28°C over this time interval. Then, resorcinol (R), formaldehyde (F, 37% w/w aqueous solution, methanol-stabilized), and hydrochloric acid catalyst (C, 37% w/w) were added to the GO suspension to achieve the weight ratio R:GO = 2:1 and the following molar ratios: R:F = 1:2, R:C = 8.4:1, R:AN = 1:76. The mixture was further sonicated, with a solid gel forming within 30 minutes, at which time the temperature of the bath had risen to 35°C. The wet gel was maintained under sonication for an additional hour, with the bath temperature rising to 43°C in this time, to increase the

mechanical rigidity of the gel before extracting it from the reaction vessel. The gel was then washed with ethanol (4 times over 48 hours) to remove all acetonitrile from the pores of the gel network, and dried in supercritical CO_2 in an autoclave so as to prevent collapse of the solid matrix and keep the porous structure intact. The dried gel was subsequently pyrolyzed under flowing argon gas (0.4 L/min) at 1000°C for 4 hours in a quartz tube furnace. Hereafter, the pyrolyzed GO-RFA and pyrolyzed RFA are denoted GO-RFA-P and RFA-P respectively, and their unpyrolyzed counterparts are denoted GO-RFA-U and RFA-U.

2.2.2. Microstructural and Chemical Characterization

Nitrogen sorption isotherms of GO-RFA-P and RFA-P were collected at 77 K in the range of relative pressures of P/P_0 = 0.01–1 using a Micromeritics TriStar II 3020 analyzer. To ensure removal of pre-adsorbed species, samples were heated in vacuum to 400°C for at least 8 hours prior to analysis. Surface area and pore size distributions were obtained by the Brunauer–Emmett–Teller (BET) and non-localized density functional theory (NLDFT) methods, respectively. The relative pressure range of P/P_0 = 0.03–0.11 was used for multipoint surface area calculations. The surface morphology of the aerogels was investigated using a FEI Sirion field-emission scanning electron microscope (SEM) with 5 kV accelerating voltage. X-ray diffraction (XRD) measurements were performed on flat sections of the bulk GO-RFA-P that were affixed to a (100) silicon wafer substrate with double-sided tape. The measurement system was a Bruker D8 Discover X-ray diffractometer equipped with a General Area Detector Diffraction System (GADDS) using a Cu K_α radiation source ($\lambda_{K\alpha}$ = 1.54 Å). Measurements were conducted over 2θ = 10° to 60° with step size 0.05°.

Fourier transform infrared spectroscopy (FTIR) of the aerogels was performed on a Bruker VERTEX 70 Spectrometer using the KBr pellet in transmission mode. The IR spectrum of GO

was obtained by the attenuated total reflectance (ATR) technique using the same spectrometer with an integrated Bruker PLATINUM ATR accessory (Unit A225/Q1). Raman spectroscopy was performed using 532 nm (2.33 eV) laser excitation, with the back-scattered light being analyzed with an Acton Research Corporation SpectraPro–500i spectrometer with a liquid nitrogen-cooled CCD detector.

X-ray photoelectron spectroscopy (XPS) was conducted using a Surface Science Instruments M-Probe with monochromatic Al K_α radiation. Samples were dropcasted on a Si wafer. A low-energy electron flood gun was employed due to the insulating nature of some samples (GO and the unpyrolyzed aerogels). Acquired spectra were deconvoluted with Hawk Data Analysis 7 software (Service Physics, Inc.). The energy calibrations were made against the C1s peak of adventitious carbon (~285 eV) as a reference. Mixed Gaussian–Lorentzian curves (>80% Gaussian) were used for each of the C1s subpeaks, with each spectrum having a constant full width at half maximum (FWHM) for all peaks except for the higher-energy O–C=O and $\pi \rightarrow \pi^*$ peaks, which have been shown to be much broader by Ganguly et al.[66]

2.2.3. Peptide Loading

Previously, Coyle, Rolandi, and Baneyx isolated the dodecapeptide Car15 (RTYLPLPWMAAL) for its ability to bind preferentially to sp^2-hybridized carbon versus sp^3-hybridized carbon.[67] Pyrolyzed aerogel samples were added to microcentrifuge tubes containing 0.5 mL of a 10 μM solution of sfGFP-Car15, a variant of superfolder green fluorescent protein (sfGFP) fused to the N-terminus of Car15, in Tris-HCl buffer (20 mM, pH 7.5). The amounts of aerogels were such that they had an approximately equivalent surface area of ~2.5 m^2. The aerogels were incubated in the sfGFP-Car15 solution at room temperature for 12 hours.

2.2.4. Supercapacitor Fabrication and Testing

A mixture of 70 wt% aerogel, 20 wt% PTFE tape (binder), and 10 wt% Timcal SUPER P conductive carbon black was ground together in a mortar and pestle, with acetone to aid dispersion, until the mixture had completely amalgamated. The amalgam was repeatedly flattened with a glass rolling pin to a ~150 μm thick sheet, from which 0.5 inch diameter electrodes were punched and dried under vacuum at 195°C for 8 hours. Supercapacitor devices were assembled with CR2325 coin cell casings in an argon glove box. A symmetric two-electrode configuration was employed, with a rayon separator and tetraethylammonium tetrafluoroborate (TEABF4) electrolyte (1 M in acetonitrile).

Electrochemical testing was performed on a Bio-Logic VMP3 potentiostat/galvanostat with EC-Lab control software. The coin cells were first conditioned over 5 galvanostatic charge–discharge cycles between 0.1 and 2.7 V, one cycle at 1 mA and four at 10 mA, to ensure complete electrolyte permeation. This was followed by 6 more galvanostatic cycles between 0.1 and 2.7 V at 1, 5, 10, 25, 50, and 100 mA. This corresponds to gravimetric current densities of 0.078, 0.39, 0.78, 1.95, 3.90, and 7.78 A g^{-1} for the GO-RFA-P and 0.067, 0.34, 0.67, 1.68, 3.36, and 6.71 A g^{-1} for the RFA-P (normalized to the mass of aerogel in the electrode). Immediately following rate testing, electrochemical impedance spectroscopy (EIS) was conducted at 2.0 V using 10 mV sinusoidal amplitude between 400 kHz and 10 mHz. Cyclic voltammetry (CV) was then performed, sweeping between 0 and 2.7 V at 20 mV s^{-1}.

2.3. Results and Discussion

2.3.1. Microstructural Analysis of Pyrolyzed Aerogels

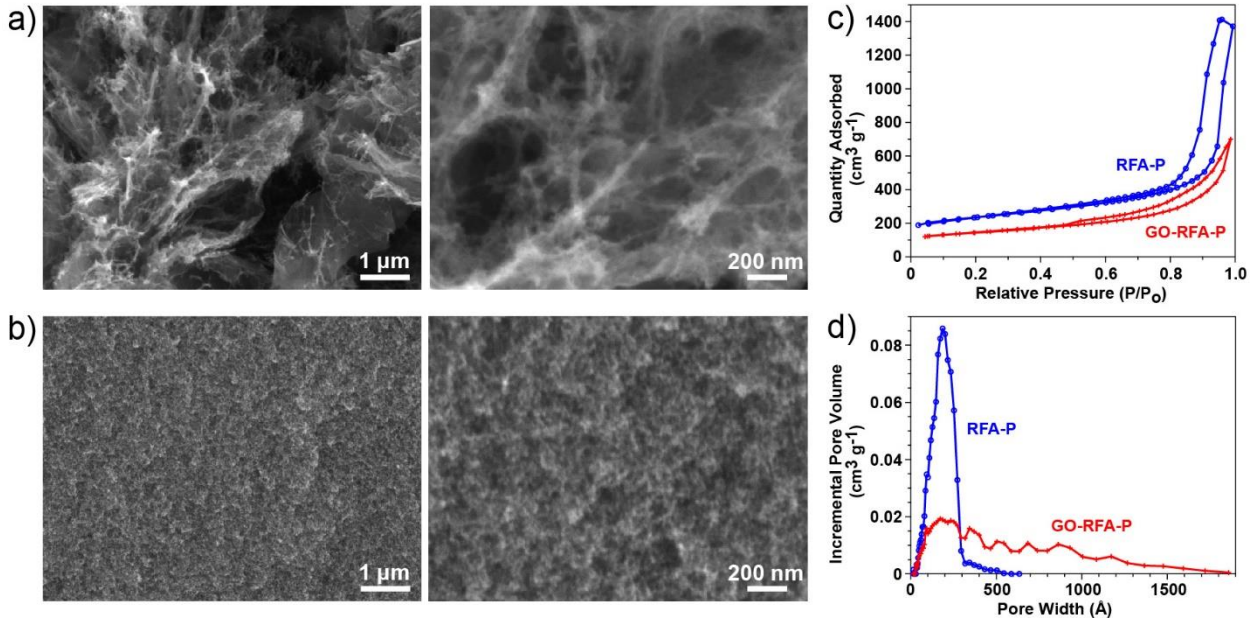

Figure 2.2. SEM images of the same location at different magnifications in **a)** GO-RFA-P, **b)** RFA-P. **c)** Nitrogen adsorption/desorption isotherms (pressure relative to 1 atm) for the aerogels. **d)** Non-localized density functional theory (NLDFT) pore size distribution plots for the aerogels.

SEM images of the GO-RFA-P (Figure 2.2a) revealed an assembly of randomly oriented, presumably graphite or graphene sheets, on the order of several microns across, embedded in an irregular network of carbonized chains of RF condensate. In addition, the network is finer on the surface of the graphitic sheets than in the bulk of the aerogel. This is because smaller RF particles form on the surface of GO sheets than in the bulk solvent due to the presence of negatively charged O^- and COO^- groups on the GO surface, which locally accelerates the deprotonation of resorcinol, the first step in the RF polymerization mechanism.[68] In contrast to the GO-RFA-P, images of the RFA-P without GO reveal a sponge-like rather than a filamentous morphology (Figure 2.2b). The RF network is more uniform in density and has finer pores and features. At higher magnification, the RFA-P appears to consist of numerous small, uniformly sized (<20 nm) beadlike particles joined in a disordered array, interspersed with similarly sized voids.

Nitrogen sorption isotherms, from which pore structure and surface area can be determined, are plotted in Figure 2.2c for the RFA-P and GO-RFA-P. The shapes of the hysteresis loop for the two aerogels agree with their microstructural features as observed with SEM. The Type H3 hysteresis loop (IUPAC classification) in the sorption isotherm of the GO-RFA-P is commonly associated with slit-shaped pores or aggregates of plate-like particles, the latter of which is representative of the incorporated GO.[69] The sorption isotherm of the RFA-P shows Type H1 hysteresis, which is characteristic of materials having well-defined cylindrical pores or spheroidal particles of approximately the same size.[69] Additionally, both total adsorption and the size of the hysteresis loop for the GO-RFA-P were smaller than that of the RFA-P, suggesting that the GO-RFA-P has lower surface area and pore volume. In support of this claim, the BET surface areas were measured to be 542 m^2 g^{-1} for GO-RFA-P and 745 m^2 g^{-1} for RFA-P, whereas the pore volume, as calculated from the maximum N_2 loading on the isotherm, is 1.08 cm^3 g^{-1} for GO-RFA and 2.19 cm^3 g^{-1} for RFA-P.

The slightly lower surface area of the GO-RFA-P compared to the RFA-P is reflective of the broader pore size distribution of the former (Figure 2.2d). Much of the pore volume of the RFA-P is confined to pores of 0–300 Å wide, with a peak width of 186 Å, and no pores of greater width than about 550 Å. The GO-RFA-P, while having a similar peak pore width (172 Å), exhibits a tail in its distribution that is more than four times longer, spanning from the peak pore width to 1850 Å. This is consistent with our SEM observation of a less dense RF network in the GO-RFA-P. Additionally, the prevalence of macropores in the GO-RFA-P can be corroborated with an earlier study on unpyrolyzed GO–RF gels by Guo et al., who noted an increase in RF particle size to > 50 nm as well as a lessening of RF polymer formation within the bulk liquid as GO loading was increased to a level (2 wt%) similar to our aerogels.[68] They ascribed this behavior to the

presence of negatively charged O^- and COO^- groups on solvated GO which accelerate the deprotonation of resorcinol. Zhao et al., in studying the polymerization of phenol–formaldehyde with GO, suggested that phenol adsorbs favorably on GO via π–π stacking interactions, which also enables the formation of ester bonds through the reaction of carboxyl groups on the edge of GO sheets with hydroxymethyl groups on hydroxymethylated derivatives of phenol.[70] It is likely that such processes also occur in the RF system, given the similar structure of resorcinol to phenol and the presence of similar hydroxymethyl derivatives during the reaction.

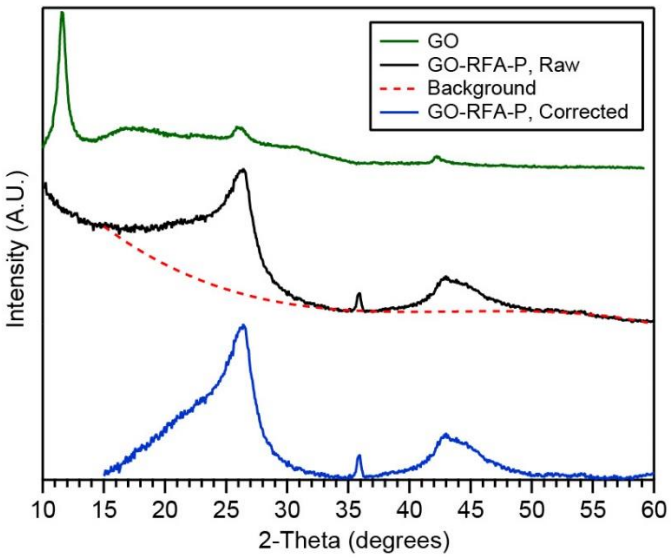

Figure 2.3. Raw X-ray diffractogram of the as-received GO (top), bulk GO-RFA-P with polynomial curve representing presumed background (middle), and background-subtracted diffractogram of GO-RFA-P (bottom).

The graphitization of the GO during pyrolysis is confirmed by XRD (Figure 2.3). The raw GO powder has its primary peak at $2\theta=11.6°$, representing the (002) basal plane with an interlayer spacing of 7.6 Å, more than twice that of pure graphite (3.35 Å) due to the introduction of oxygen moieties that expand the lattice. Although a graphitic peak ($2\theta=26.6°$) is also present in the GO powder, it is broad and weak. On the other hand, in GO-RFA-P, the lower-angle peak has disappeared while the graphitic peak remains and becomes the most prominent peak, suggesting decomposition of the oxygen functionalities and conversion of GO to graphite. The weaker,

broader peak centered on 2θ = 44° originates from the (101) planes of graphite. A third weak but sharp peak at 2θ = 36.0° suggests the presence of a small amount of beta silicon carbide (β-SiC), whose intense (111) diffraction peak occurs at this angle.[71] This likely originated from our use of a quartz tube furnace for GO-RFA pyrolysis. At temperatures of 1000°C or greater, silica undergoes a solid-state reaction with carbon to form silicon carbide and carbon monoxide.[72,73]

The in-plane size and thickness of the graphitic crystallites in the aerogel can be quantified from the (002) graphitic peak of the background-subtracted XRD pattern using the Scherrer equation:

$$L_{a,c} = \frac{k_{a,c}\,\lambda_{K\alpha}}{\beta \cos\theta} \quad \textbf{(2.1)}$$

where $L_{a,c}$ is the apparent crystallite size perpendicular and parallel to the *c*-axis (i.e., in-plane and out-of-plane) respectively, $k_{a,c}$ is a particle shape- and direction-dependent factor (1.84 for L_a and 0.91 for L_c), θ is the position of the (002) peak (13.2°), and β is the full width at half-maximum (FWHM) of the (002) peak in 2θ (radians) units.[74] The β parameter was corrected for instrumental broadening using the expression $\beta = \sqrt{\beta_m^2 - \beta_{Si}^2}$, where β_m is the measured FWHM of the (002) peak for the aerogel and β_{Si} is the FWHM of the (111) peak of a standard single-crystal silicon wafer, which was obtained experimentally. This silicon peak was chosen since it occurs at a 2θ value (28.5°) very close to the (002) graphitic peak. The in-plane crystallite size calculated by this method was 3.5 nm. This is within the same order of magnitude as the crystallite size calculated from the Raman spectrograph of the aerogel (9.9 nm, see Section 2.3.2) and therefore suggests that the micron-scale sheets observed in Figure 2.2a are polycrystalline. The calculated crystallite thickness was 1.7 nm, corresponding to 6 carbon layers. It should be noted, however, that both of

these dimensions are likely to be underestimates of the true values due to the broad hump underlying the (002) peak, which comes from the amorphous carbon matrix of the aerogel.

2.3.2. Spectroscopic Analysis of Aerogels Pre- and Post-Pyrolysis

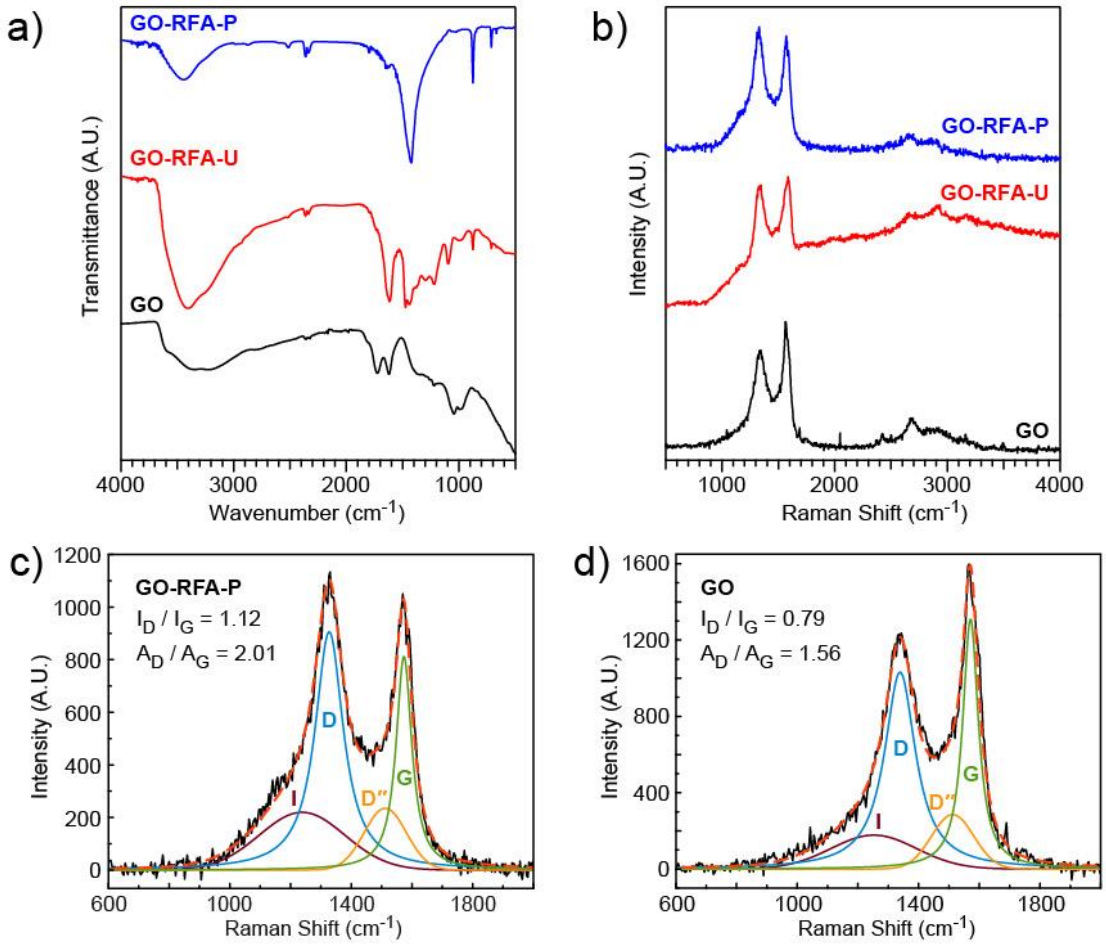

Figure 2.4. (**a)** FTIR spectra and (**b)** Raman spectra of the pyrolyzed and unpyrolyzed GO-RFA, along with GO for reference. Deconvoluted carbon regions of Raman spectra of **(c)** GO-RFA-P and **(d)** GO showing I, D, D″, and G bands with D-to-G peak intensity and peak area ratios.

Vibrational modes present in the bonds of the GO-RFA were investigated with FTIR and Raman spectroscopy (Figure 2.4). IR spectra of GO reference powder and of the GO-RFA before and after pyrolysis are presented in Figure 2.4a. Characteristic absorbances were assigned from the literature.[75] The two small bands at 2360 and 2340 cm^{-1} do not originate in the analyzed material, but correspond to carbon dioxide from the atmosphere. Most importantly, comparison of the

spectra of the two aerogels confirms the thermal decomposition of the oxygen-containing functional groups in GO. The absorption bands of the epoxy C–O–C stretch at 1221 cm^{-1} and the alkoxy C–O stretch at 1095 cm^{-1} are present in GO-RFA-U but not in GO-RFA-P. Additionally, both GO powder and GO-RFA-U display the carboxylic acid C=O stretch around 1730 cm^{-1} (though only a shoulder in the latter due to convolution with a more intense adjacent band), while the corresponding band in GO-RFA-P (again appearing as a shoulder) is significantly weaker.

Interestingly, both GO-RFA-U and GO-RFA-P, in addition to GO powder, display the broad absorption band starting at 3700 cm^{-1} of the hydrogen bonded O–H stretch. However, in the GO and GO-RFA-U, this band stretches all the way to 2500 cm^{-1}, encompassing the characteristic O–H absorption frequencies of both alcohols (3600–3000 cm^{-1}) and carboxylic acids (3000–2500 cm^{-1}), while in GO-RFA-P the band only goes to 3050 cm^{-1}; furthermore, this O–H band is significantly more intense in GO-RFA-U than in GO-RFA-P. These observations suggest that pyrolysis resulted in near-complete removal of the carboxyl groups that are abundant on the edge planes of pristine GO, but only partial removal of the alcohols. This conclusion agrees with more detailed investigations of the structural evolution of GO during thermal reduction, which have established that the carboxyl groups become highly unstable at temperatures above 400°C.[66] The continued existence of the alcohol O–H band in the carbonized gel can be explained by the reaction of basal plane epoxides around 400°C with adjacent hydroxyl groups to form phenol groups, which have been shown to survive even at 1000°C,[66] the temperature at which our GO-RFA was pyrolyzed. It is thermodynamically difficult to completely pyrolyze C–OH, mainly because of its position within the interlayer spacing between intact conjugated domains.[76,77]

The presence of aromatic rings in both the unpyrolyzed and pyrolyzed GO-RFA, originating from the GO and RF condensate, is evident from the aromatic C=C stretching bands:

an intense band at 1425 cm^{-1} and much weaker band at 1630 cm^{-1} for the GO-RFA-P; the two sharp bands at 1440 cm^{-1} and 1615 cm^{-1} for the GO-RFA-U; and a single sharp band at 1620 cm^{-1} for the GO. The occurrence of only a single peak in GO for this type of vibration may be a result of convolution, as suggested by the steady drop in transmission from 1500 cm^{-1} to 1400 cm^{-1}, the range where the second peak was observed in the two aerogel samples. The slight shift of the C=C bands following pyrolysis may reflect the accompanying reduction in the extent of aromatic substitution in the material as well as the change in nature of the substituents, from epoxy, carboxyl, and phenol groups to phenol groups alone. Interestingly, the sharp aromatic C–H out-of-plane bending bands visible at 879, 712, and 667 cm^{-1} in GO-RFA-U appear to be at similar positions in GO-RFA-P, indicating that the substitution pattern remains largely the same.[78,79] Additionally, there are no observable absorption bands attributable to C≡N (2260–2240 cm^{-1}), C=N (1690–1650 cm^{-1}), or C–N (1350–1000 cm^{-1}) in the GO-RFA-P, suggesting complete removal of acetonitrile and any nitrogen-containing species.

Raman spectra of the GO-RFA before and after pyrolysis are shown in Figure 2.4b. The peak centered at about 1570 cm^{-1} denotes the G band which is associated with the doubly degenerate (iTO and LO) phonon mode with E_{2g} symmetry at the Brillouin zone center.[80] The peak at 1330 cm^{-1} is the disorder-induced D band, attributed to A_{1g} modes at the zone boundary that consist only of C-C bond stretching motions.[81] The peak intensity ratio of these two bands, I_D/I_G, can be used as a rough measure of disorder in the carbon, where a higher I_D/I_G indicates a higher fraction of disordered and/or defective carbon.[82,83] Additionally, the peak area ratio of the bands, A_D/A_G, is inversely proportional to the in-plane size L_a of the graphitic sp^2 crystallites in the sample, which can be approximated by:[84]

$$\boldsymbol{L_a\ (\mathrm{nm}) = \frac{560}{E_l^4}\left(\frac{A_D}{A_G}\right)^{-1}} \qquad \textbf{(2.2)}$$

where E_l is the excitation laser energy in eV, which for our Raman measurement is 2.33 eV (λ = 532 nm).

To determine the peak intensity and area ratios, the spectra of GO-RFA-P and GO were deconvoluted into 4 subpeaks (Figure 2.4c, d); deconvolution was not possible for GO-RFA-U due to the strong background fluorescence characteristic of polymeric samples. In addition to the major D and G bands, there is a D″ band at 1510 cm^{-1} associated with amorphous sp^2 carbon, and an I band at 1240–1250 cm^{-1} associated with ionic impurities, or carbon–carbon stretching modes of polyene-like structures.[85] Following the method of Vallerot et al., Lorentzian functions were used to fit the D and G bands, whereas Gaussian functions were used for the I and D″ bands.[86]

GO-RFA-P has both a markedly higher I_D/I_G and A_D/A_G than GO. Using Equation 2.2 on A_D/A_G gives L_a = 9.5 nm for GO-RFA-P and 12.2 nm for GO; the former is on the same order of magnitude as the crystallite size of 3.5 nm obtained from the XRD data of GO-RFA-P (see Section 2.3.1). These changes appear to be brought about by pyrolysis rather than gelation, as the D peak in GO-RFA-U appears to be lower than the G peak, similar to GO but opposite to GO-RFA-P. The reduction in graphitic domain size and increase in disorder during pyrolysis may be attributed to the breakage of chemical cross-links between GO sheets that were originally formed during gelation, in the same manner that the breakage of methylene and methylene ether bridges between individual aromatic rings has been observed for pyrolysis of pure RF gels.[87] This would leave the sheets with dangling bonds that could then form interplanar sp^3 bridges as described by Milev et al.,[88] reducing the extent of each individual graphitic domain and increasing the number of edge defects.

XPS was performed on both unpyrolyzed and pyrolyzed aerogels, along with the as-received GO, to analyze the relative composition of elements and carbon functional groups. The

C1s core-level spectra and C/O atomic ratios, as calculated from the survey spectra, are depicted in Figure 2.5. Interestingly, the C/O ratio of GO is very close to both RFA-U and GO-RFA-U, making it difficult to ascertain from this information alone whether the GO chemically incorporated into the larger RF framework or was simply an inert additive for GO-RFA-U. However, the C1s spectra do in fact suggest chemical changes in the GO during gelation, as the spectrum of GO-RFA-U appears very similar to that of RFA-U, consisting of a single broad hump, whereas the spectrum of the GO has a distinct two-peaked structure.

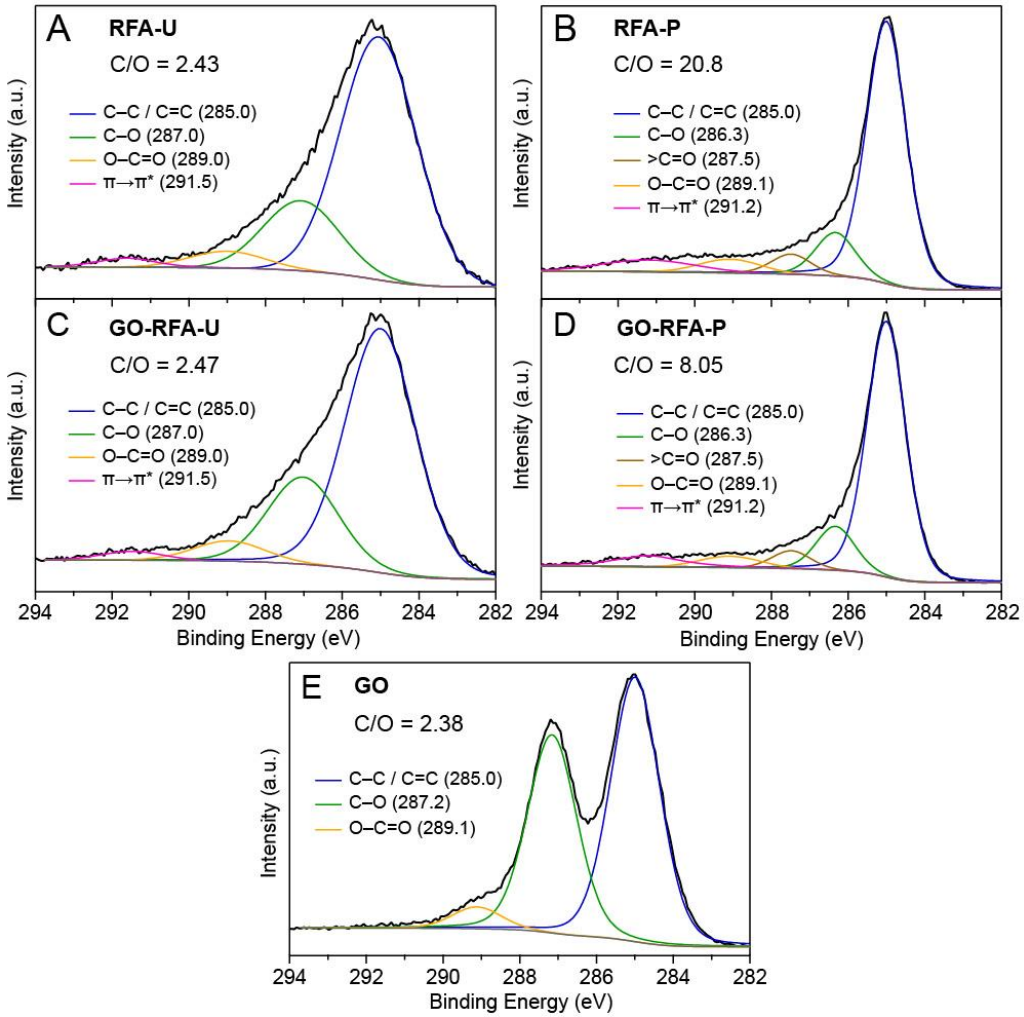

Figure 2.5. C1s XPS spectrum showing deconvoluted peaks, and C/O ratios, calculated from survey spectrum, of **(a)** RFA-U, **(b)** RFA-P, **(c)** GO-RFA-U, **(d)** GO-RFA-P, **(e)** GO.

Deconvolution of the unpyrolyzed aerogel spectra gives four sub-peaks centered at 285.0, 287.0, 289.0, and 291.5 eV, which correspond respectively to C–C / C=C bonding, C–O (alkoxy and epoxy), O–C=O (carboxyl and ester), and the $\pi \rightarrow \pi^*$ (HOMO–LUMO) shake-up satellite peak characteristic of sp^2-hybridized carbon. The first three of these peaks also appear in the deconvoluted spectrum of GO, but the C–O peak is much more prominent and slightly up-shifted (287.2 eV). This is consistent with other XPS analyses of GO and illustrates the abundance of epoxide surface groups on GO, which have a higher C1s binding energy than C–OH groups that are predominant in RF polymer. It should also be noted that the oxygenated carbon subpeaks comprise 45% of the total C1s peak area in pure GO, but only 30% and 26% of the total C1s peak area in GO-RFA-U and RFA-U respectively. Considering the substantial amount of GO loaded into the former (almost a third of the combined mass of resorcinol and formaldehyde), one would expect the GO to more significantly increase the fraction of carbon–oxygen groups in GO-RFA-U relative to RFA-U, but this is not the case, indicating that the GO was partially reduced during gelation.

To explain this observation, previous studies have shown that the polymerization of the related phenol–formaldehyde system can mediate the solution-phase reduction of GO, giving C1s XPS spectra similar to our unpyrolyzed aerogels.[70,89] Yuan et al. proposed that the phenolate anion opens the epoxide groups of GO through S_N2 nucleophilic attack, resulting in formation of the unstable phenoxonium ion, which is then converted to a C=C double bond by thermal elimination.[89] Zhao et al., in the same study showing preferential phenol–formaldehyde polymerization on GO sheets, proposed that phenol physisorbs onto the GO surface via π–π stacking and promotes removal of oxygen groups from GO, which simultaneously oxidizes the phenol to benzoquinone.[70]

XPS analysis of the pyrolyzed aerogels provide evidence for more significant loss of oxygen, with the measured C/O ratio of both samples exceeding 8. Interestingly, the pyrolyzed aerogels also exhibit strikingly similar C1s spectra to one another, with a sharper peak than their unpyrolyzed counterparts followed by a long tail toward higher binding energy. The spectra can be deconvoluted to the same four subpeaks previously described, but a fifth peak appears, centered at 287.5 eV and representing carbonyl (>C=O) groups. Physically, this can be explained by thermal decarboxylation of carboxylic acids or ester linkages (embodied by the O–C=O subpeak in the spectra of the unpyrolyzed samples, which remains as a minor peak in the pyrolyzed samples). The C–O peak remains the most prominent carbon–oxygen subpeak, consistent with our FTIR study that showed an obvious O–H band in GO-RFA-P, along with the aforementioned high thermal stability of phenol groups.

2.3.3. Peptide Loading

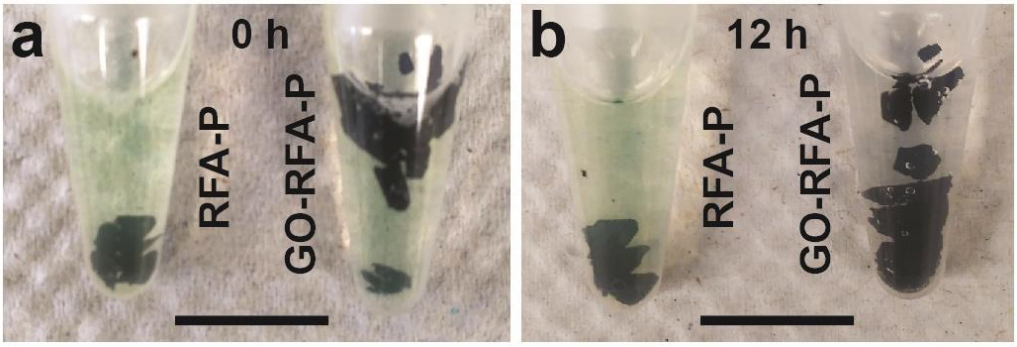

Figure 2.6. Carbon aerogel samples immersed in sfGFP-Car15 solution **(a)** immediately after inserting aerogels; **(b)** 12 h after inserting aerogels showing loss of green color for solution containing GOA, but not for solution containing RFA. Scale bar in both images = 1 cm.

As another confirmation of the predominance of graphitic material in GO-RFA-P relative to RFA-P, aerogel incubation experiments were performed in buffered aqueous solutions of superfolder green fluorescent protein (sfGFP) fused to the N-terminus of Car15, a peptide that binds specifically to sp^2 carbon.[67] After 12 h, the original light green coloration has disappeared for the

protein solution containing GO-RFA-P, whereas the color persists in the solution containing RFA-P (Figure 2.6), showing enrichment of sp^2 carbon in GO-RFA-P.

2.3.4. Electrochemical Testing Results

The specific gravimetric capacitances of a single GO-RFA-P or RFA-P electrode were evaluated from the galvanostatic discharge profiles at each current density using the following equation:[90]

$$C_{s,g} = \frac{8\, I \int_{t_1}^{t_2} V dt}{m_a\,(V_2 - V_1)^2} \qquad \textbf{(2.3)}$$

where I is the constant discharge current, m_a is the total mass of active material in both electrodes, ρ is the bulk density of the active material, and (t_1, V_1), (t_2, V_2) are two chosen points on the voltage–time curve. Our reported values use the full potential window of our discharge tests (2.7–0.1 V). The GO-RFA-P supercapacitor exhibited a maximum gravimetric capacitance of 54.1 F g^{-1}, which is slightly lower than the maximum of 64.6 F g^{-1} attained by the RFA-P supercapacitor. However, owing to the RFA-P's larger specific surface area, the performance improvement with the addition of GO becomes apparent when capacitance is normalized to area instead (0.100 F m^{-2} for GO-RFA-P versus 0.0867 F m^{-2} for RFA-P).

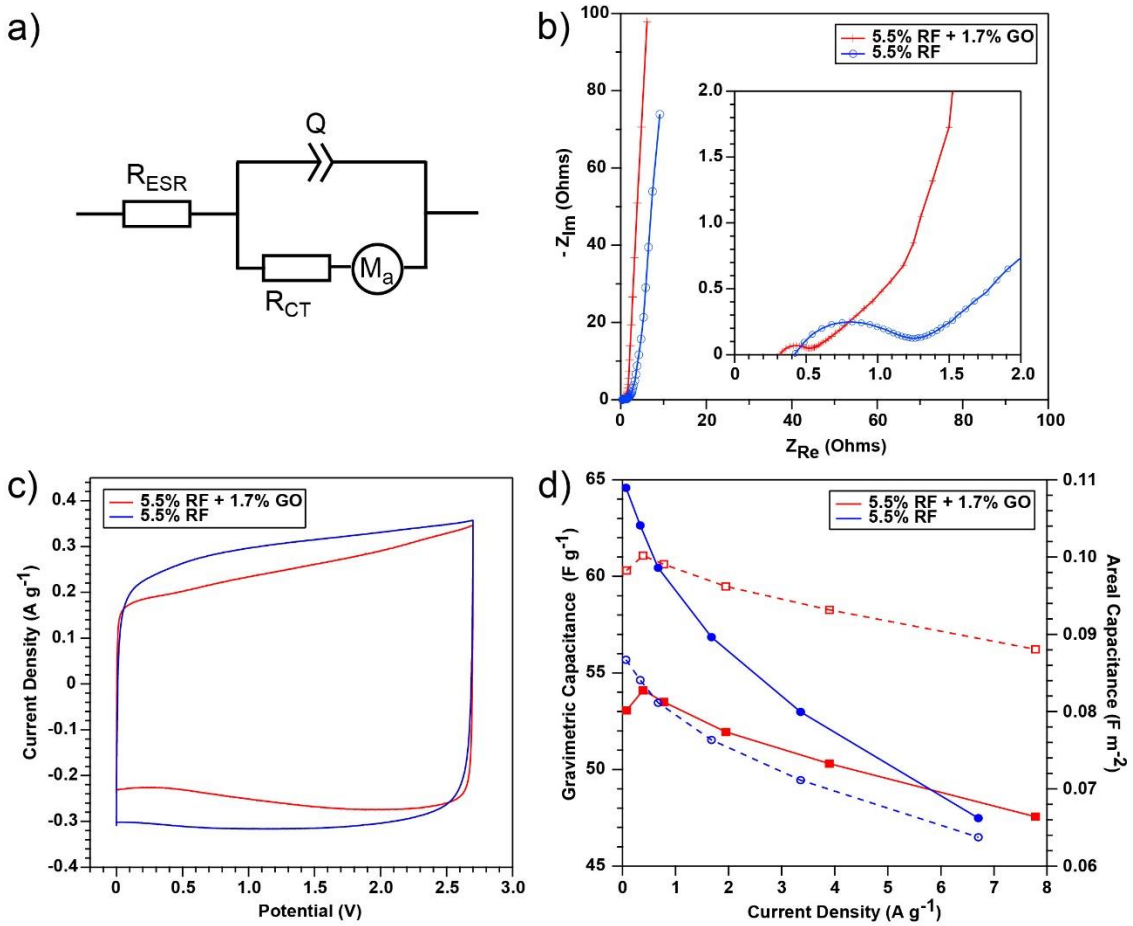

Figure 2.7. Coin cell testing results of the pyrolyzed GO-loaded RF aerogels and plain RF aerogels. **a)** Equivalent circuit diagram of the supercapacitor. **b)** EIS Nyquist plots (inset shows more detail of high to mid frequency range). **c)** Cyclic voltammograms (sweep rate 20 mV s^{-1}). **d)** Rate capability plot obtained from galvanostatic charge–discharge tests. Solid lines show trend in gravimetric capacitance while dashed lines show trend in areal capacitance.

Resistance is a key property of performance in assessing the viability of GO-RFA-P for supercapacitor applications. Since supercapacitors are designed for high power, manufacturers look for materials that can minimize system resistance. To inspect operational resistance in our aerogel devices, we fit the experimental EIS data, shown as Nyquist plots in Figure 2.7b, to the equivalent circuit in Figure 2.7a. This circuit consists of an equivalent series resistance R_{ESR} followed by a constant phase element Q in parallel to a charge transfer resistance R_{CT} and a finite linear diffusion element M_a. R_{ESR} comprises the resistances associated with the bulk electrolyte, bulk electrode, and "external" parts of the system such as the current collector, terminals, and

leads. It is represented in the Nyquist plot by the intercept of the curve with the real impedance axis in the high-frequency range (small magnitudes of real and imaginary impedance). R_{CT} comprises the resistances due to electron transfer at interfaces in the device and specific adsorption of ions onto the active material, and is measured as the diameter of the best-fit semicircle at mid to high frequencies. Although R_{CT} is typically associated with the kinetics of Faradaic reactions at the electrode–electrolyte interface, the lack of peaks or troughs in the CV sweeps (Figure 2.7c), as well as the lack of voltage plateaus in the galvanostatic discharge profiles, suggest that no such reactions occur under our testing conditions.

Aside from the resistive elements, the constant phase element (CPE) accounts for frequency dispersion of capacitance that arises from the inhomogeneities of porous and rough electrodes.[91] This causes a slight depression and angling of the semicircular arc that is characteristic of an R|C component. Finally, M_a is a particular mass-transport impedance where the diffusion layer has a finite thickness and a reflecting (non-permeable) boundary condition. This accounts for the resistance of electrolyte in pores and interfacial double-layer capacitance along pore walls.[92] In the Nyquist plot, M_a manifests as the kinked line following the semicircle, which deviates from the vertical line of an ideal capacitor. A related performance metric is the knee frequency f_k, which is the frequency at which the semicircle transitions into the sloped linear region in the Nyquist plot, corresponding to a local minimum of the phase angle. Physically, the knee frequency signifies the point below which ions can penetrate more easily into pores of the active material, covering its entire surface to produce capacitive behavior.

As seen in Figure 2.7b, the addition of GO lowered R_{ESR} by 24% (0.32 Ω compared to 0.42 Ω for the RFA-P). This reduction is hypothesized to be due mainly to the superior electrical conductivity of the cross-linked graphene framework of the GO-RFA-P versus the more

amorphous RFA-P. Improved electrical contact between the current collector and GO-RFA-P active material compared to RFA-P is a possible secondary factor, though less likely given the similar testing conditions and supercapacitor device preparation for the two materials. The Warburg region is slightly shorter for the GO-RFA-P, spanning about 0.66 Ω on the real impedance axis compared to 0.77 Ω for the RFA-P, which is also indicative of less obstruction of ion movement.[93] Additionally, R_{CT} was lowered by 72% (0.21 Ω compared to 0.81 Ω for the RFA-P), most likely due to the wider, more open pore structure of the GO-RFA-P as seen in Figure 2.2. With a greater mesoporous structure, the ions in the electrolyte can more easily access all pores in the active material, lowering the diffusion-related resistance; also, contact area at the electrode–electrolyte interface is increased, which is consistent with the higher capacitance per unit surface area of the GO-RFA-P. Finally, the capacitive region of the GO-RFA-P is observed to not only begin at a lower impedance value than the RFA-P, but also at a frequency almost seven times higher (f_k = 3930 Hz for GO-RFA-P versus 540 Hz for RFA-P), indicating enhanced specific power capability of the GO-RFA-P.[94] Furthermore, the steeper slope of this region and the shorter length of the preceding 45° Warburg region for the GO-RFA-P indicate closer-to-ideal capacitive behavior, as well as less ionic transport resistance during operation, which is also consistent with the GO-RFA-P's larger average pore size.[95]

The current–voltage plots from the CV sweeps (Figure 2.7c) can serve as an alternative method to measure specific capacitance, via the equation:[96]

$$\boldsymbol{C_{s,g\,(CV)} = \frac{4\,I}{m_a\,\mu}} \qquad \textbf{(2.4)}$$

where I is the current, m_a is the total mass of active material in both electrodes, and μ is the fixed scan rate (in this case 20 mV s^{-1}). Using the maximum discharge current as I, the gravimetric

capacitances derived from CV are 55.2 F g^{-1} for GO-RFA-P and 63.3 F g^{-1} for RFA-P, which are within 2% of the maximum values derived from galvanostatic discharge.

The pronounced rectangular shape of the CV curve for GO-RFA-P indicates near-ideal electric double-layer capacitance behavior. In contrast, the voltammogram for the RFA-P supercapacitor has somewhat rounded corners, indicating (in agreement with the EIS data) larger resistance to ion diffusion that causes the current to respond more slowly to changes in the direction of the voltage sweep.[97] Thus, in spite of the similar values of specific capacitance, CV demonstrates that the power capability of the GO-RFA-P supercapacitor is superior to that of the RFA-P.

Higher resistance, as seen in both the EIS Nyquist and CV plots, can be directly evidenced through observing the effect of increasing discharge current on specific capacitance (Figure 2.7d). At low current densities, RFA-P and GO-RFA-P both exhibit relatively high capacitances. However, as the rate is increased, the capacitance of the pure RFA carbons drop due to excessive resistance within the carbon. For the RFA-P, by the highest tested rate of 6.7 A g^{-1} the capacitance is only 73% of the capacitance at the lowest rate of 0.34 A g^{-1}. The graphene aerogel uniquely and dramatically increases the rate performance with 90% capacitance retention over an even wider range of current densities, 0.39 A g^{-1} to 7.8 A g^{-1}. It is believed that the performance improvement can be attributed to the increase in conductive pathways for both ions and electron mobility within the carbon in the presence of pyrolyzed GO.

2.4. Conclusion

To summarize this chapter, we have presented a method for the ultrafast synthesis of graphene aerogels based on the polycondensation of resorcinol, formaldehyde, and graphene oxide with HCl as the catalyst and acetonitrile as the solvent. This synthetic approach greatly reduces the gelation

time from many hours or even several days (using the traditional base-catalyzed route) to just 1–2 hours, making it easier to produce graphene aerogels on a large scale within reasonable time and potentially reducing their cost. Our graphene aerogels maintained the high surface area and porosity reported for plain RF-derived carbon aerogels, making them attractive candidates for applications such as supercapacitors, solar cells, catalyst supports, and oil sorption, which benefit from such characteristics as well as the intrinsic properties of graphene. As a vivid illustration of the favorable impact of graphene on supercapacitor performance, graphene aerogels synthesized by our rapid technique exceeded aerogels of plain carbonized RF in areal capacitance and power capability, suggesting that our work could accelerate the manufacture of high-performing energy storage devices. Conceivably, the capacitance of the graphene aerogels could be further improved by tailoring surface area and pore volume using CO_2 activation and varying the ratio of GO to RF; or by experimenting with aqueous electrolytes with smaller ion size, as opposed to the organic electrolyte used in this study. Future research efforts in rapid graphene aerogel synthesis will include aqueous synthetic techniques, which is less expensive, safer to use, and more environmentally friendly than current methods using acetonitrile.

Chapter 3. Crystalline Loading of Coenzyme Q_{10} within Graphene and Amorphous Carbon Aerogels Derived from RF Chemistry[2]

3.1. Introduction

In this brief chapter, we illustrate the usefulness of our rapidly synthesized graphene and amorphous carbon aerogels beyond electrochemical energy storage by evaluating them as host materials for lipophilic pharmaceuticals. The inherently low water solubility of such compounds presents a major hurdle to their delivery and bioavailability. Graphene aerogels offer a promising solution to this challenge due to their abundance of hydrophobic graphitic surfaces that are favorable to lipophilic molecule adsorption, as well as their porous morphology that allows them to load large concentrations of drugs, suppress their aggregation,[98] and prolong shelf life by hindering oxygen diffusion.[99] Furthermore, carbons derived from pyrolysis of RF polymers and graphene derived from pyrolysis of GO both show good biocompatibility from *in vitro* studies with human cells,[100,101] and aerogels can provide controlled delivery of drugs through mechanisms such as biodegradation,[102] swelling of the aerogel matrix,[103] thermal activation,[104] and changes in local pH.[105]

Molecular compounds can be loaded into the pores of the aerogel by mixing them with the gel precursors during synthesis (as we have just shown with GO), diffusion from solvents before or after supercritical drying, or diffusion from supercritical CO_2 during the drying process. Supercritical loading, in particular, can yield both amorphous and crystalline phases of the compound,[99,106] but it is expensive to scale up and limited by low drug solubility in supercritical

[2] This chapter is in preparation and will be published. It is comprised of work from myself, Sandeep Manandhar, and Jennifer L. Hanson, with valuable input from Xuezhe Zhou, Paden B. Roder, D. Scott Wilbur, Brittney Hellner, François Baneyx, and Peter J. Pauzauskie.

CO_2. Crystalline pharmaceuticals offer several advantages over their amorphous counterparts, including greater chemical stability and longer release times for oral or dermal delivery.[107]

In this study, we chose Coenzyme Q_{10} (CoQ_{10}) as a model drug for loading our graphene and carbon aerogels based on its polyunsaturated chemical bonding (Figure 3.1), ubiquity and importance for human health. It is synthesized in human tissue and mediates the production of cellular energy in the form of adenosine triphosphate (ATP),[108] acts as a stabilizing agent in cellular membranes,[109] and is a potent antioxidant.[110,111] Using a mild, low-cost, diffusion-based loading procedure, we show that CoQ_{10} binds preferentially and more quickly to the graphene aerogel, as hypothesized. In addition, the bound CoQ_{10} adopts an as-yet unreported crystalline phase that differs from bulk CoQ_{10}, not only offering the potential advantages of crystalline materials for drug delivery, but also a means to control the microstructure of this important lipophilic pharmaceutical. To our knowledge, this is the first reported demonstration of loading aerogels with crystalline pharmaceuticals outside of supercritical loading.

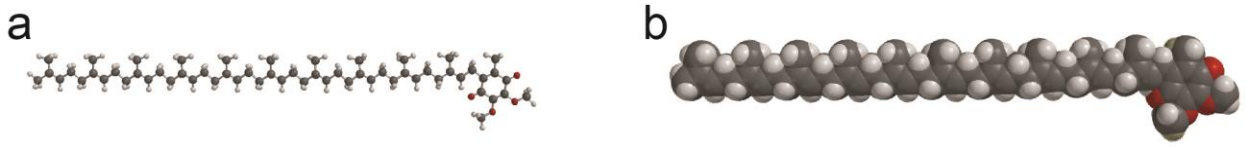

Figure 3.1. (a) Ball-and-stick model and **(b)** space-filling model of CoQ_{10} showing dimethoxybenzoquinone moiety and 10 mono-unsaturated trans-isoprenoid units in the side chain. Carbon atoms are dark gray, hydrogen atoms are light gray, and oxygen atoms are red.

3.2. Materials and Methods

Graphene and carbon aerogels were made by the same rapid, acid-catalyzed technique as the samples from Chapter 2, but with the precursor amounts adjusted to achieve a resorcinol to acetonitrile molar ratio of 1:200, and a resorcinol to GO mass ratio of 4:1; this corresponds to an initial GO dispersion of 2.6 mg mL^{-1} in aceotonitrile. The molar ratios of resorcinol to formaldehyde and resorcinol to HCl were kept similar to before, at 1:2 and 8:1 respectively.

Additionally, aerogel pyrolysis was conducted in nitrogen rather than argon. The pyrolyzed pure RF and GO-loaded RF aerogels used for this study are hereafter denoted **RFA** and **GOA** respectively.

CoQ_{10} loading for weight gain measurement was performed using a 1 mg mL^{-1} CoQ_{10} solution in acetonitrile, as CoQ_{10} had appreciable solubility in acetonitrile compared to other volatile solvents like methanol and hexane. A known mass of pyrolyzed aerogel was added to the CoQ_{10} solution in a polypropylene tube, and incubated at room temperature for 12 h. The solution infiltrated the aerogel pores and CoQ_{10} adsorbed onto the aerogel surface. This was evident from visual inspection, as the yellow solution became noticeably lighter (Figure 3.3a, b). The aerogel was then removed from the solution and air-dried at room temperature for at least 12 h. Drying at elevated temperature was avoided due to the low melting point of CoQ_{10} (49°C)[112] and possible degradation of CoQ_{10} crystals. The mass gain of the dried aerogel relative to the pre-incubated aerogel effectively represents the mass of CoQ_{10} loaded into the aerogel, since control immersion/drying experiments of **RFA** in pure acetonitrile gave less than 0.64% mass gain.

The adsorption of CoQ_{10} onto the aerogels was quantified in real-time *via* UV-vis spectroscopy, using a Thermo Scientific Evolution 300 spectrophotometer with a xenon lamp light source. Approximately 5 mg aerogel was added to 3 mL of 0.1 mg mL^{-1} CoQ_{10}–acetonitrile solution in a Nova Biotech 10 mm, 3.5 mL quartz cuvette. Before each measurement, the base line of the spectrophotometer was calibrated against solvent. Absorbance measurements were taken every 15 min for a total of 12 h. Concentrations and kinetic parameters were derived from the absorbance at 273 nm—where CoQ_{10} has a strong absorption band—using a standard curve of absorbance at 273 nm for solutions having various known concentrations of CoQ_{10}.

Nitrogen sorption isotherms were collected at 77 K using a Quantachrome Nova 2200e analyzer. To remove pre-adsorbed species, the aerogel samples were heated in vacuum at 200°C for at least 12 h prior to measurements, and immediately loaded in the analyzer thereafter. Specific surface area and pore size distributions were obtained by the Brunauer–Emmett–Teller (BET)[113] and Barrett–Joyner–Halenda (BJH)[114] methods respectively, using Quantachrome NovaWin software. XRD was performed identically to the description in Section 2.2.2.

3.3. Results and Discussion

3.3.1. Aerogel Pore Structure

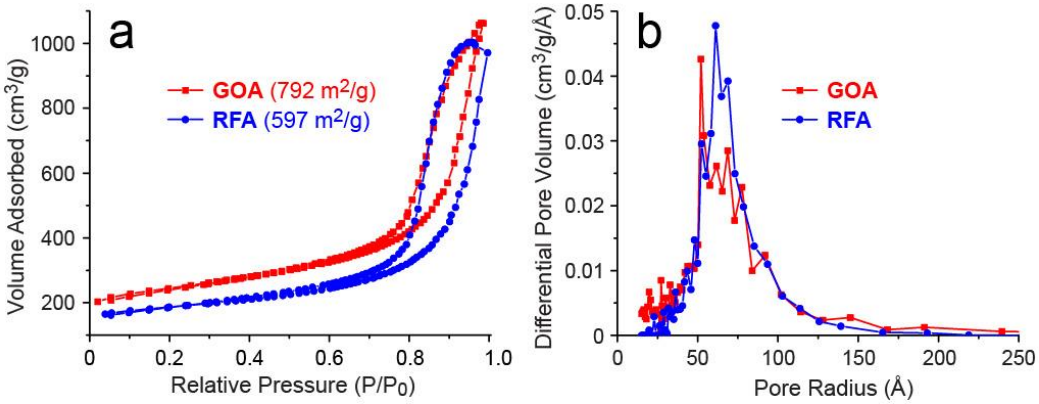

Figure 3.2. (a) Nitrogen sorption isotherms with BET surface area, and **(b)** BJH pore size distributions of **GOA** and **RFA**.

Nitrogen sorption analysis gave similar results to the aerogels used for supercapacitor testing (Section 2.3.1), with **RFA** showing a type H1 isotherm and **GOA** showing a type H3 isotherm (Figure 3.2a). The specific surface areas were also in a similar range to the previously described aerogels, but interestingly **GOA** had the higher surface area in this case, at 792 m^2 g^{-1} versus 597 m^2 g^{-1} for **RFA**. We hypothesize that this is because of the lower concentration of GO in these aerogels (R:GO = 4), which could allow GO to reinforce the RF polymeric matrix and mitigate pore collapse while not limiting polymer formation within the bulk liquid, as previously suggested for the aerogels with R:GO = 2 (Chapter 2).[68] Consistent with this idea, the GO-loaded aerogels exhibited less shrinkage after supercritical drying than the pure RF aerogels. Looking at the pore

size distributions (Figure 3.2b), **GOA** actually has a slightly smaller peak pore radius than **RFA** (52 Å and 61 Å respectively). However, **GOA** still has a greater fraction of large pores, with 19.1% of its pore volume coming from pores above 100 Å in radius, compared to 8.4% for **RFA**. The specific pore volumes of the two samples were similar—1.55 $cm^3\ g^{-1}$ for **RFA** and 1.64 $cm^3\ g^{-1}$ for **GOA**, based on the maximum N_2 loading from the isotherm.

3.3.2. CoQ_{10} Loading Experiments

From the incubation and drying experiments in 1 mg mL^{-1} CoQ_{10} solution, **GOA** gained significantly more weight than **RFA** (20.8±2.1% versus 11.9±2.7%). The larger uptake is mainly attributed to the abundance of π-conjugated sp^2 carbon surfaces in **GOA**, with which CoQ_{10} molecules can interact via π–π stacking;[115] however, the favorability of **GOA** for CoQ_{10} may also stem from hydrogen bonding between the carbonyl groups of CoQ_{10} and residual phenol groups on the pyrolyzed GO, which, as previously discussed, can survive the high-temperature treatment. Additionally, the presence of larger pores and more surface area per unit mass in **GOA** would also facilitate uptake of CoQ_{10} from solution.

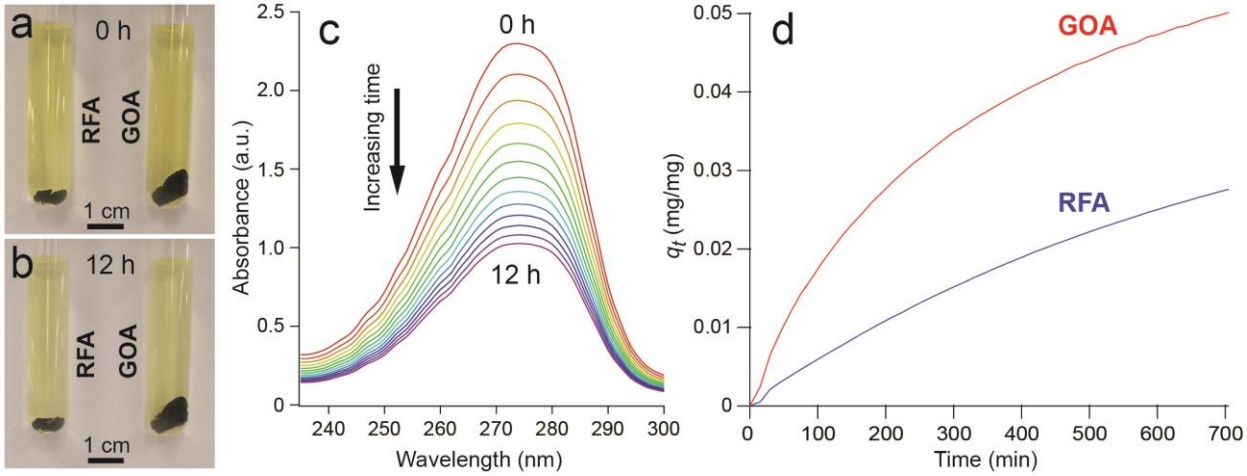

Figure 3.3. Carbon aerogel samples immersed in 1 mg mL^{-1} CoQ_{10}/acetonitrile solution (~5 mg of aerogel in 3 mL of solution) **(a)** immediately after inserting aerogels; **(b)** 12 h after inserting aerogels showing lightening of bulk solution. **(c)** UV-vis spectrum of **GOA** over 12 h in 0.1 mg mL^{-1} CoQ_{10} solution showing decrease in intensity of absorption band centered at 273 nm. **(d)** Plot of sorption capacity of CoQ_{10} in aerogels over time as derived from UV-vis measurements.

UV-vis measurements also attested to the uptake of CoQ_{10} by both aerogels, with the intensity of the 273 nm absorption band decreasing following addition of the aerogel (Figure 3.3c), indicating loss of CoQ_{10} from bulk solution. To examine the loading kinetics more closely, we fitted the measurements to both pseudo first-order and pseudo second-order models (Figure 3.4). The pseudo first-order rate expression of Lagergren is:[116]

$$\ln(q_e - q_t) = \ln(q_e) - k_1 t \quad (3.1)$$

where k_1 is the rate constant (per min) and q_e and q_t are the sorption capacities at equilibrium and at time t respectively (mg/mg). A straight line plot of $\ln(q_e - q_t)$ versus t fits experimental data to this model, which is generally valid for conditions far from saturation.[117] q_t was determined by:

$$q_t = V(C_0 - C_t)/m \quad (3.2)$$

where V is the volume of solution (mL), m is the mass of aerogel (mg), and C_0 and C_t are the initial CoQ_{10} concentration and concentration at time t respectively (mg/mL). q_e was determined by the same equation, using the concentration at the end of the experiment ($t \approx 12$ h). As seen in the plot of q_t versus time (Figure 3.3d), **GOA** takes up CoQ_{10} much more rapidly than **RFA**, and q_e of **GOA** is almost double that of **RFA** (Table 3.1), consistent with the mass gain experiments and lipophilic nature of the pyrolyzed GO.

The pseudo second-order kinetic model is expressed in linearized form as:[118]

$$t/q_t = 1/(k_2 q_e^2) + (1/q_e)t \quad (3.3)$$

where k_2 is the rate constant (mg aerogel/mg CoQ_{10} per min). The plot of t/q_t versus t shows a linear relationship for second order kinetic phenomena. Unlike the pseudo first-order model, it predicts behavior over the whole range of adsorption and does not require q_e to be known for fitting.[119]

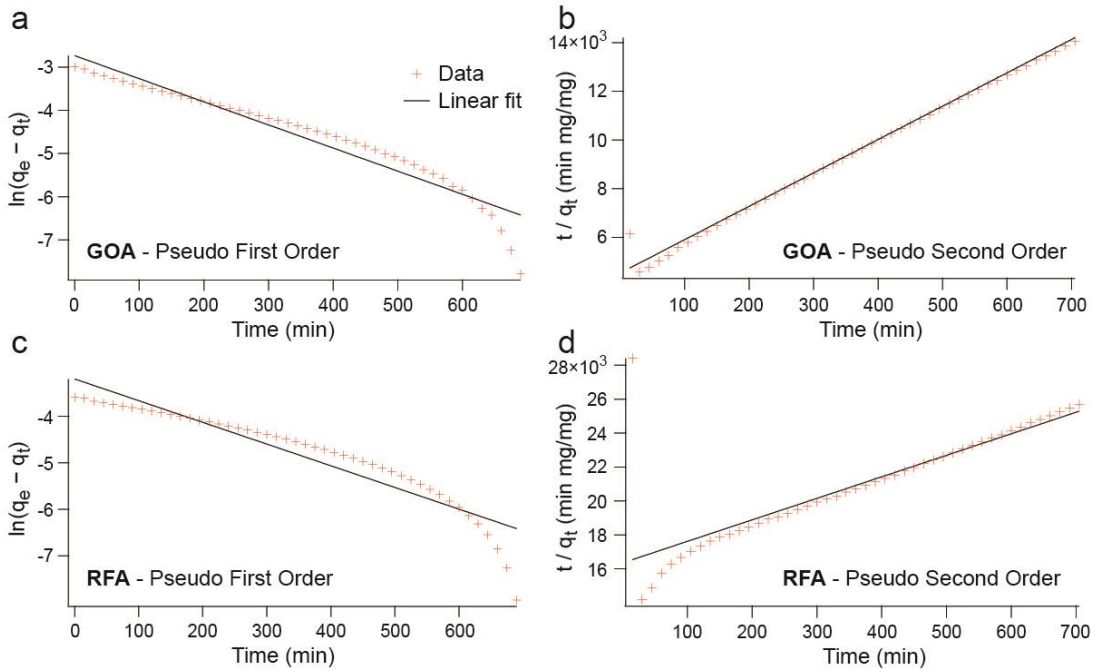

Figure 3.4. Pseudo first-order and pseudo second-order kinetic fits for CoQ_{10} adsorption on **(a, b) GOA** and **(c, d) RFA**.

Table 3.1. Kinetic Parameters for CoQ_{10} Adsorption on Aerogels

Sample	Experimental	Pseudo First Order Model			Pseudo Second Order Model		
	q_e (mg/mg)	k_1 (min^{-1})	$q_{e(calc)}$ (mg/mg)	R^2	k_2 (mg/mg/min)	$q_{e(calc)}$ (mg/mg)	R^2
RFA	0.0274	0.0107	0.0408	0.876	0.0789	0.0790	0.664
GOA	0.0498	0.0123	0.0651	0.921	0.0415	0.0729	0.993

The pseudo first-order and second-order rate constants, along with a "calculated" equilibrium adsorption capacity ($q_{e(calc)}$) for both models were obtained from the coefficients of the linear fits described above. The results with correlation coefficients (R^2) are presented in Table 3.1. For **GOA**, the pseudo second-order model is more appropriate as its corresponding R^2 is over 0.99, compared to 0.921 for the pseudo first-order model. However, neither model is a good fit for the **RFA** dataset as a whole. Rather, it appears that **RFA** follows first-order kinetics at short times (t < 120 min), but second-order kinetics at longer times. The initial first-order kinetics in **RFA** suggest that the rate-limiting step is film diffusion.[120] This is consistent with the smaller average pore size of **RFA**, which would slow penetration of CoQ_{10} into the aerogel matrix relative

to **GOA**. On the other hand, the pseudo second-order behavior in both aerogels at longer times suggests that the rate-limiting step is associated with chemisorption, in which electrons are shared or exchanged between the CoQ_{10} molecules and aerogel.[119] Additionally, the calculated q_e for both models are high compared to experimental q_e values. This is likely due to the slowness of the adsorption process; as seen in Figure 3.3d, the concentration of CoQ_{10} on both aerogels continued to increase even at 12 h.

3.3.3. Crystallinity of the Adsorbed CoQ_{10}

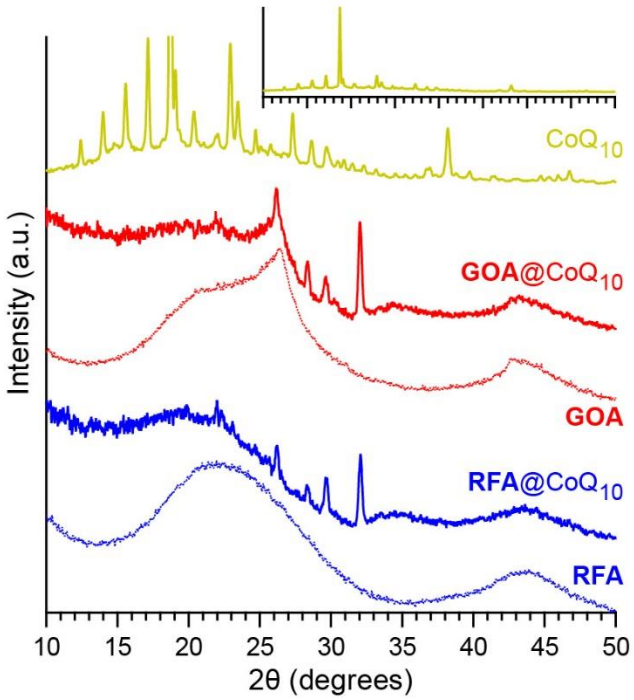

Figure 3.5. XRD patterns of as-received CoQ_{10} powder and carbon aerogels. Inset shows full intensity scale of CoQ_{10} diffraction pattern for same range of 2θ (10–50°). For aerogels, solid lines denote aerogels loaded with CoQ_{10} and dotted lines denote their unloaded counterparts.

XRD was performed on the dried aerogels incubated in 1 mg mL^{-1} CoQ_{10}, as well as the as-received CoQ_{10} powder, to check the crystallinity of the adsorbed CoQ_{10} (Figure 3.5). The as-received CoQ_{10} powder is observed to be highly crystalline and its pattern matches previous reports.[121,122] **GOA** shows a similar XRD pattern to the graphene aerogel from Chapter 2, with two prominent and broad crystalline peaks at 2θ = 26.6° and 44°, corresponding to the (002) and (101) planes of

graphite. Using the Scherrer equation on the graphitic (002) peak, the average thickness of the sheets in **GOA** was estimated to be ~6.5 nm, corresponding to ~20 carbon layers.[74] **RFA** shows no sharp crystalline peaks, only the two broad humps centered at 2θ=23° and 44° that are also visible in **GOA** and are typical of porous amorphous carbons.[123,124] However, the loaded **GOA** and **RFA** show a series of sharp crystalline peaks at similar positions that are not present in the unloaded counterparts and obviously differ from the as-received CoQ_{10}, which has many more peaks. It is worth noting that an earlier XRD study by Katsikas and Quinn,[125] on a sample of CoQ_{10} prepared by slow cooling from its liquid phase, showed only eight reflections from 7.86–2.40 Å (2θ=11.3–37.5°), indicating that CoQ_{10} can adopt simpler crystal structures. In addition, the peaks are slightly more intense for the loaded **GOA** than the loaded **RFA**, consistent with the higher CoQ_{10} mass loading of the former. Although the diffraction patterns of the loaded aerogels do not completely match any previously reported phase of CoQ_{10}, four of the peaks—at 2θ=22.0°, 26.2°, 29.6°, and 32.1°—match reflections observed by Katsikas and Quinn, whereas the three reflections that they observed at lower angles are not visible in the aerogels. We hypothesize that the narrow pores of the aerogel have a confining effect on the CoQ_{10} molecules that prevents them from adopting long-range order when crystallizing, thus explaining the absence of the low-angle (large d-spacing) peaks. This makes sense considering that the longest dimension of the free CoQ_{10} molecule (55.38 Å, obtained from the Spartan'14 molecular modeling software with the CPK space-filling model) is on the same order as the peak pore radii of the aerogels.

3.4. Conclusion

In summary, we have demonstrated the loading of a key lipophilic pharmaceutical, CoQ_{10}, on carbon aerogel hosts using a simple, solution-phase impregnation technique. The carbon aerogels are biocompatible and can be synthesized by a rapid, scalable technique. Mass gain and

spectroscopic studies confirm that graphene oxide, when added to and pyrolyzed with the carbon aerogel precursors, greatly enhances the aerogel's loading capacity and rate of uptake for CoQ_{10}. We attribute this improvement to the highly lipophilic nature of the sp^2-hybridized, π-conjugated graphene surfaces provided by the pyrolyzed GO. Furthermore, the loaded CoQ_{10} forms a unique crystalline phase on both pure amorphous carbon aerogels and aerogels containing pyrolyzed GO, providing a number of potential advantages for drug delivery applications, such as slower, sustained release, as well as the possibility to control the microstructure of CoQ_{10}. More broadly, our platform can be easily tailored to other important pharmaceuticals, simply by incorporating additives into the carbon aerogel during synthesis that can favorably interact with the drug of interest.

Chapter 4. Rapid Sol–Gel Synthesis of Composite TMD–Carbon Aerogels[3]

4.1. Introduction

Transition metal dichalcogenides (TMD's) are crystalline materials whose formula unit consists of a transition metal atom and two chalcogen (Group VI) atoms. Typically they form layered-sheet structures where in each sheet the metal atoms are sandwiched between chalcogen atoms, with weak van der Waals bonding between neighboring sheets, similar to graphite. TMD's have shown promise as supercapacitor active materials due to the range of oxidation states available to transition metals[126–129]. In addition, a recent report demonstrated that the capacitance of MoS_2, perhaps the best-known TMD, significantly improves after conversion from the semiconducting 2H phase to the metallic 1T phase. This is due to enhanced electrical conductivity—the in-plane conductivity of 2H MoS_2 is ~0.2 S cm^{-1} and that of the 1T phase is 10–100 S cm^{-1}—increased ion intercalation mobility, and hydrophilicity of the 1T phase[127,130,131]. Similarly, 2H MoS_2 and WS_2-based supercapacitor performance improved after creation of mesoporous structure with enhanced conductivity[132,133]. However, it is important to note that the most successful 1T devices suffered from a low SSA of 9 m^2 g^{-1}, and required the use of pyrophoric n-butyllithium to exfoliate the material and induce a phase change. Both of these factors mitigate the scalability of its impressive performance, not to mention the dangers of working with pyrophoric chemicals. Furthermore, freestanding TMD films do not exhibit mechanical stability in electrochemical environments, which sets a limit to the maximum size of unsupported films and inhibits high surface area applications[134].

[3] This chapter is based on "Rapid synthesis of transition metal dichalcogenide–carbon aerogel composites for supercapacitor electrodes", published in *Microsystems & Nanoengineering* **3**, 17032 (2017) by Matthew J. Crane, Matthew B. Lim, Xuezhe Zhou, and Peter J. Pauzauskie. I and Matthew Crane were co-first authors and co-wrote the manuscript.

To address the aforementioned limitations, we have encapsulated exfoliated TMD sheets in an RF aerogel matrix via a scalable process similar to that used for the graphene aerogels (Chapter 2). The process employs the ultrasonication of bulk TMD precursors—MoS_2 and WS_2—in acetonitrile to produce 2H MoS_2 and WS_2, respectively, followed by the rapid, acid-catalyzed gelation of RF within 30 minutes at mild temperatures (~40°C). After supercritical drying and pyrolysis, the resulting carbon aerogel provides a high surface area, rigid, and electrically conductive support for the exfoliated TMDs that is well-suited for electrochemical devices. To demonstrate these applications, we perform supercapacitor tests on our TMD-loaded carbon aerogels that yield favorable specific capacitances around 80 F g^{-1}, volumetric capacitances approaching 60 F cm^{-3}, long cycle life, and low operational electrochemical impedance. In addition, RF chemistry and liquid-phase exfoliation offer a benign alternative to the conventional use of pyrophoric chemicals.

4.2. Methods

4.2.1. Aerogel Synthesis

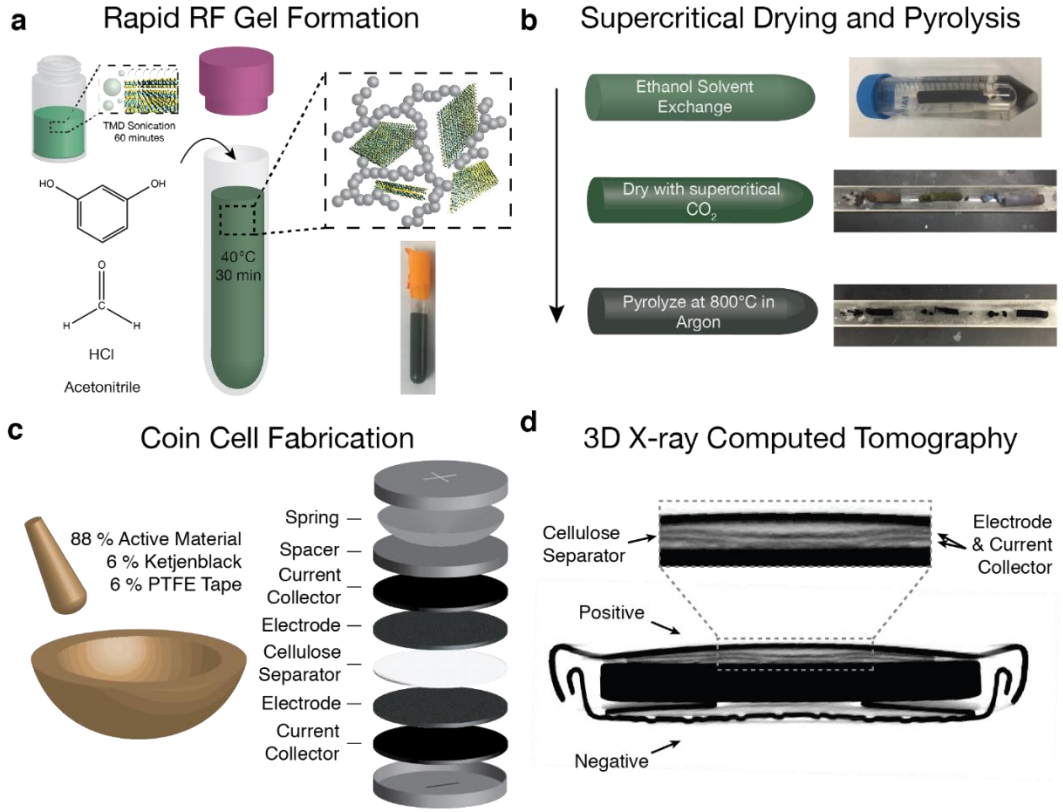

Figure 4.1. Outline of the synthetic process for composite TMD carbon aerogels. **a)** Initially, sonication driven cavitation drives TMD sheets apart and enhances dispersion within acetonitrile. Resorcinol, formaldehyde, and hydrochloric acid are added to this solution, which causes rapid sol-gel formation upon further sonication. **b)** This gel is washed with ethanol, dried with supercritical CO_2, and pyrolyzed in argon. **c)** Finally, the material is processed into a supercapacitor by grinding it with carbon black additive (Ketjenblack) and PTFE tape, rolling and punching it into electrodes that are assembled into a symmetric coin cell with a cellulose separator. **e)** 3D X-ray computed tomography image of a coin cell after 10,000 charge–discharge cycles.

Because exfoliated TMD sheets restack to form low surface area (9 m^2 g^{-1}) films when they dry,[127,135] our synthesis of the TMD-loaded aerogels was designed to avoid allowing the TMD solution to dry before the gelation can trap any exfoliated sheets. Figure 4.1 illustrates our synthetic scheme, which is similar to that of the graphene aerogels (Section 2.2.1). In the first step, a temperature-controlled bath sonicator (~22˚C) exfoliates and disperses bulk TMD sheets in acetonitrile (AN) in a glass vial. Although our study focused on aerogels made from TMD dispersions at concentrations from 8.6 to 34 mg/mL, we were able to synthesize aerogels at TMD

loadings of up to 100 mg/mL in acetonitrile. After sonication for 60 minutes, the dispersion was transferred to a polypropylene tube and added resorcinol (R), formaldehyde (F, 37 wt-% methanol-stabilized aqueous solution), and hydrochloric acid (C, 37 wt-%) to achieve molar ratios of R:F = 1:2, R:C = 8.4:1, and R:AN = 1:76[26,136], which result in R:TMD = 2:1 by weight for a 17.1 mg/mL starting dispersion of TMD. This corresponds to molar ratios for resorcinol to MoS_2 and WS_2 of 2.9:1 and 4.5:1 respectively. For WS_2-loaded gels, we prepared additional samples by the same technique using initial WS_2 dispersions of 8.6 mg/mL and 34 mg/mL, which corresponds respectively to 4:1 and 1:1 weight ratios, or 9.0:1 and 2.25:1 molar ratios, of resorcinol to WS_2. We also prepared a control sample with no TMD. The mixture of reagents was quickly placed in the bath sonicator set to 40˚C for 30 minutes to form the gel. The gel was then removed from the polypropylene tube, washed with ethanol three times over 36 hours to remove the acetonitrile, and dried with supercritical CO_2 in an autoclave. Finally, the resultant aerogel was pyrolyzed under flowing argon gas at 800˚C for 4 hours in a quartz tube furnace. Although the aerogels in the graphene aerogel studies were pyrolyzed at 1000˚C, in this case we found that annealing at that temperature destroyed the TMD's. Henceforth, the pyrolyzed pure RF aerogel will be abbreviated RFA, the pyrolyzed MoS_2-loaded aerogel will be abbreviated MA-17, and the pyrolyzed WS_2-loaded aerogel will be abbreviated WA-8.6, WA-17, or WA-34 according to the concentration of the initial TMD dispersion.

4.2.2. Microstructural and Chemical Characterization

To characterize the aerogels, we employed nitrogen sorption, XRD, Raman spectroscopy, FTIR spectroscopy, and TEM. Nitrogen sorption isotherms were collected using a Quantachrome NOVA 2200e porosimeter, with samples being heated in vacuum at 200°C for at least 12 h prior to analysis to drive off pre-adsorbed species. From the isotherms, surface area and pore size

distributions were obtained with Brunauer-Emmett-Teller (BET) theory and Barrett-Joyner-Halenda (BJH) theory respectively. Specifically, multipoint surface area calculations used data from the relative pressure (P/P_0) range between 0.05 to 0.30, and the pore size distributions used the desorption isotherm. Raman spectra were obtained using a home built setup comprised of a 532 nm (2.33 eV) laser focused with a 50x objective (0.55 NA) and collected on an Acton Research SpectraPro 500i spectrometer fitted with a liquid nitrogen-cooled CCD detector. XRD patterns were collected on a Bruker D8 Discover X-ray diffractometer equipped with General Area Detector Diffraction System (GADDS) and a Cu K_α source at 1.54 Å. FTIR measurements were performed by the KBr pellet method with a Bruker VERTEX 70 spectrometer in transmission mode. Finally, bright-field TEM images with accompanying selected-area electron diffraction (SAED) patterns and energy-dispersive X-ray spectra (EDS) were obtained on an FEI Tecnai G2 F20 with 200 kV accelerating voltage.

4.2.3. Supercapacitor Fabrication and Testing

To fabricate coin cell electrodes, the pyrolyzed TMD-loaded aerogels were ground in a rotary mill and passed through a #140 test sieve (opening size ~106 μm). The milled, sieved product (88 wt%) was ground further with PTFE tape (6 wt%) as a binder, and Ketjenblack carbon black (6 wt%) in a mortar and pestle until the mixture was completely amalgamated. The amalgam was flattened with a glass rolling pin to a ~100 μm thick sheet, from which 0.5" diameter electrodes were punched out. Supercapacitor devices were assembled in a symmetric two-electrode configuration consisting of a sandwich of SUPER-P carbon black @ aluminum foil current collectors, CR2032 coin cell casings and TMD-loaded aerogel electrodes surrounding a cellulose separator, filled with 1 M Na_2SO_4 aqueous electrolyte.

The electrochemical performance of our supercapacitor cells was evaluated using a Bio-Logic VMP3 potentiostat / galvanostat with EC-Lab software. The cells were first conditioned over 5 galvanostatic charge–discharge cycles between 0.1 and 0.9 V, one cycle at 1 mA and four at 10 mA, to ensure complete electrolyte permeation. This was followed by six more galvanostatic cycles between 0.1 and 0.9 V, which were used for capacitance measurements. In these cycles, the cell was charged at 10 mA and discharged at increasing gravimetric current densities of 0.054, 0.28, 0.56, 1.39, 2.78, and 5.53 A g^{-1} for MA-17; and 0.059, 0.30, 0.60, 1.51, 3.02, and 6.03 A g^{-1} for all WS_2 aerogels as well as the RFA (normalized to the mass of active material). For the samples made from 17 mg mL^{-1} TMD dispersions, this corresponds to currents of 1, 5, 10, 25, 50, and 100 mA. Immediately after rate testing, electrochemical impedance spectroscopy (EIS) was conducted at 0.5 V with a 5 mV sinusoidal oscillation between 400 kHz and 10 mHz. Finally, cyclic voltammetry (CV) was performed, sweeping between 0 and 0.9 V at 20 mV s^{-1}. For WA-17, a galvanostatic cycling test was performed following cyclic voltammetry, whereby the cell underwent 2000 continuous charge–discharge cycles between 0.1 and 0.9 V at a fixed current density of 0.25 A g^{-1}.

4.3. Results and Discussion

4.3.1. Microstructural Analysis of Pyrolyzed Aerogels

TEM images of the pyrolyzed aerogels in Figure 4.2 confirmed that the RF matrix, which consisted of nanoscale carbon particles characteristic of a pyrolyzed aerogel, acted as a support for the TMD sheets. Electron diffraction (Figure 4.2a and 4.2c, inset) and EDS of the aerogel composites demonstrate that the sol-gel process does not chemically modify the TMD's. After incorporation, these TMD crystals range in size from 5–60 nm in the (002) stacking plane and up to micron scale in length. While it does not have a high exfoliation efficiency, acetonitrile is effective at preserving

large area sheet sizes by physisorbing to the chalcogenide atoms in TMDs to reduce van der Waals forces before subsequent intercalation[137]. This mild reduction is believed to prevent scissoring of TMDs and lead to large area sheet dispersion (Figure 4.2b, d)[138]. The WS_2 composite exhibited the highest degree of exfoliation from our extensive TEM observations.

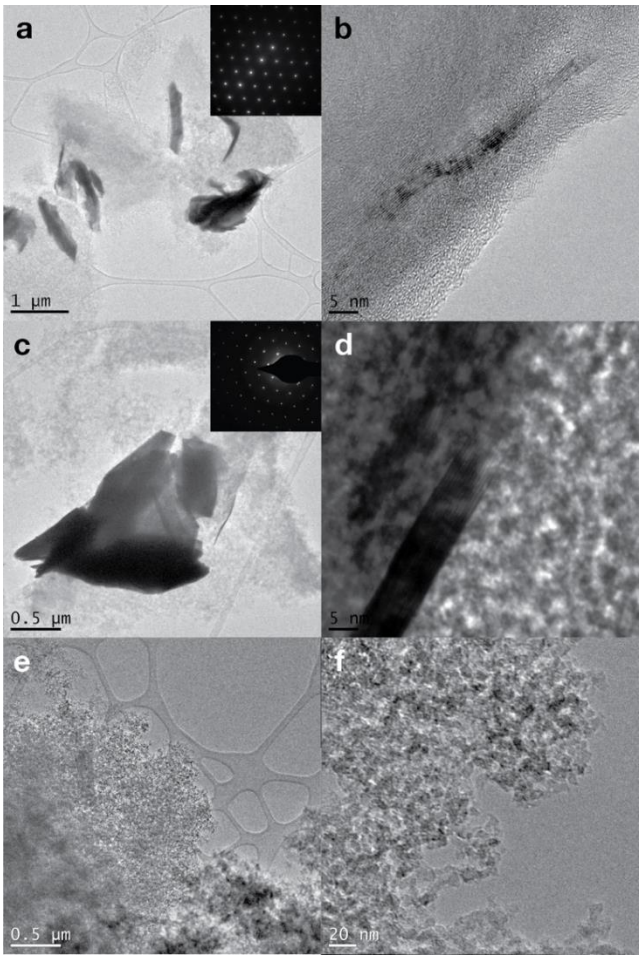

Figure 4.2. TEM images of MA-17 **(a, b)**, WA-17 **(c, d)**, and RFA **(e, f)**. Panels e and f are characteristic of the gels as synthesized, while panels a, b, c, and d demonstrate the presence of exfoliated sheets. Insets in the TEM images (a and c) show electron diffraction of the TMD sheets dispersed in the aerogel**.**

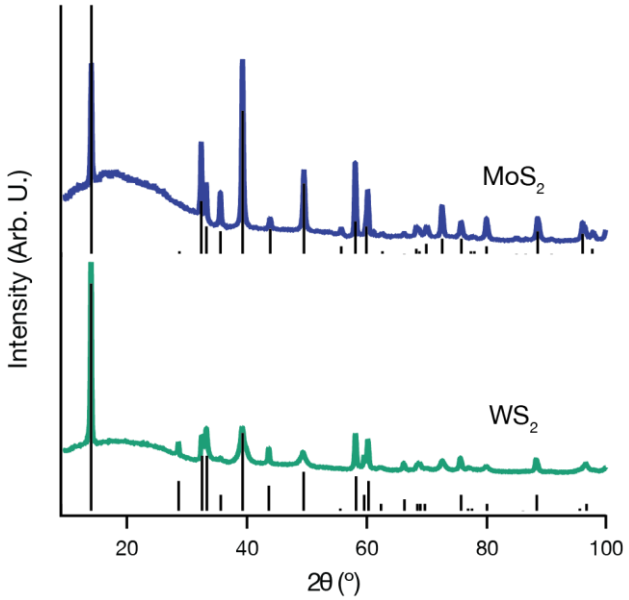

Figure 4.3. XRD patterns of MA-17 and WA-17. Vertical solid lines show the corresponding XRD peaks and relative intensities of 2H-MoS_2 and 2H-WS_2 from the International Centre for Diffraction Data cards.

Electron diffraction from the TEM analysis, along with XRD (Figure 4.3) demonstrated that the TMD's remained crystalline throughout the rapid sol-gel processing and the subsequent high-temperature pyrolysis. Although the 1T phase was not achieved in either TMD-loaded aerogel, the sharp peaks in the XRD patterns are identified as highly crystalline 2H phases of WS_2 and MoS_2. The underlying broad peak centered at $2\theta=17^{\circ}$ originates from amorphous carbon within the aerogel[26]. In a similar fashion to the graphene aerogels, we estimated the thickness of the TMD crystals loaded into the aerogels using the Scherrer equation on the (002) diffraction peak of the TMDs (see Section 2.3.1, Equation 2.1). However, in this case, we used a modified shape factor *k* of 0.76[139] and corrected for instrumental broadening using a peak of a corundum standard (NIST SRM 1976b) that occurs at a nearby Bragg angle to the TMD (002) peak, which occurs at $2\theta=14.2^{\circ}$ for WS_2 and $2\theta=14.4^{\circ}$ for MoS_2. This analysis suggested that on average, the thickness of the WS_2 crystallites in the (002) axis is about the same for all the WS_2-loaded aerogels, around 58 nm or 92 layers; whereas the thickness of the MoS_2 crystallites in the MoS_2-loaded aerogel is

somewhat lower at 37 nm or 60 layers (Table 4.1). This agrees well with the cross-sectional TEM images of the pyrolyzed aerogels.

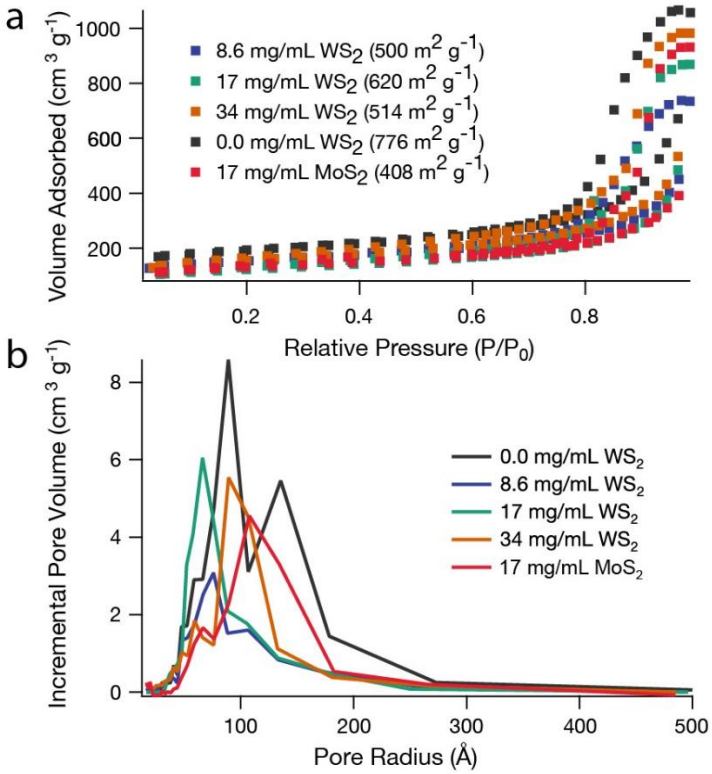

Figure 4.4. a) Nitrogen sorption isotherms with BET surface area and **b)** BJH pore size distribution of pyrolyzed aerogel with different mass loadings of TMD.

BET analysis of the aerogels (Figure 4.4) demonstrated that the neither the addition of TMD sheets in this accelerated synthesis, nor the amount of TMD added significantly impacted the surface area or the morphology of the gel. All the TMD-loaded aerogels maintained high surface areas greater than 400 m^2 g^{-1}, with a maximum for WA-17 at 620 m^2 g^{-1}. Furthermore, processing the aerogels for supercapacitor electrodes did not significantly affect their surface area: WA-17 retained 94% of its original surface area after milling and sieving, and electrode sheets made from combining the same milled and sieved sample with PTFE tape and carbon black retained 99% of the original surface area of the aerogel. These results suggest that the aerogel represents a mechanically stable support throughout processing.

The theoretical maximum surface areas for the TMD's can be calculated by extrapolating from the unit cell and neglecting edge effects, and are 752 and 483 $m^2 g^{-1}$ for MoS_2 and WS_2 respectively. Comparing these values to our control aerogel of pure pyrolyzed RF (776 $m^2 g^{-1}$), it is clear that the carbon aerogel constituted the majority of the surface area[26]. In contrast to the graphene aerogel, the nitrogen sorption isotherms of all the aerogels in this study, including the unloaded control, exhibited type H1 hysteresis[140], which is characteristic of largely uniform diameter spherical particles. This further confirms that the carbonaceous matrix made up most of the surface area in the TMD-loaded samples, and that the addition of TMD's did not significantly affect the character of the matrix. Indeed, the TEM images in Figure 4.2 show that the TMD's incorporated as large sheets of material supported by the homogeneous network of carbonized RF polymer. The BJH pore size distributions of the TMD-loaded aerogels were roughly unimodal and peaked below 100 Å pore radius, revealing their mesoporous nature. In contrast, the RFA featured a bimodal pore distribution with larger pores on average than the other samples, as evidenced by the peaks at 90 and 135 Å, and a tail extending past 250 Å.

4.3.2. Spectroscopic Analysis

In FTIR spectra of MA-17 and WA-17 (Figure 4.5a), the absence of epoxy functional groups at 1220 cm^{-1} and alkoxy groups at 1095 cm^{-1}, which form during polycondensation of resorcinol and formaldehyde, shows that pyrolysis successfully removed these oxygen-containing moieties[141]. The broad band centered at 1510 cm^{-1} along with the weaker band at 1630 cm^{-1} correspond to C=C–C stretching in an aromatic ring and is evidence of carbonized sp^2-bonded structures in the aerogels. The band at 1340 cm^{-1} represents O–H bending in phenol groups, which, as previously noted, have been observed to survive heat treatment even at 1000°C, well above the pyrolysis temperature of 800°C for our aerogels.[142] Notably, both aerogels exhibit a small peak at 680

cm^{-1}, corresponding to a C–S mode, which suggests that the rapid synthesis and subsequent pyrolysis produces chemical bonding between the RF matrix and the TMD sheets.

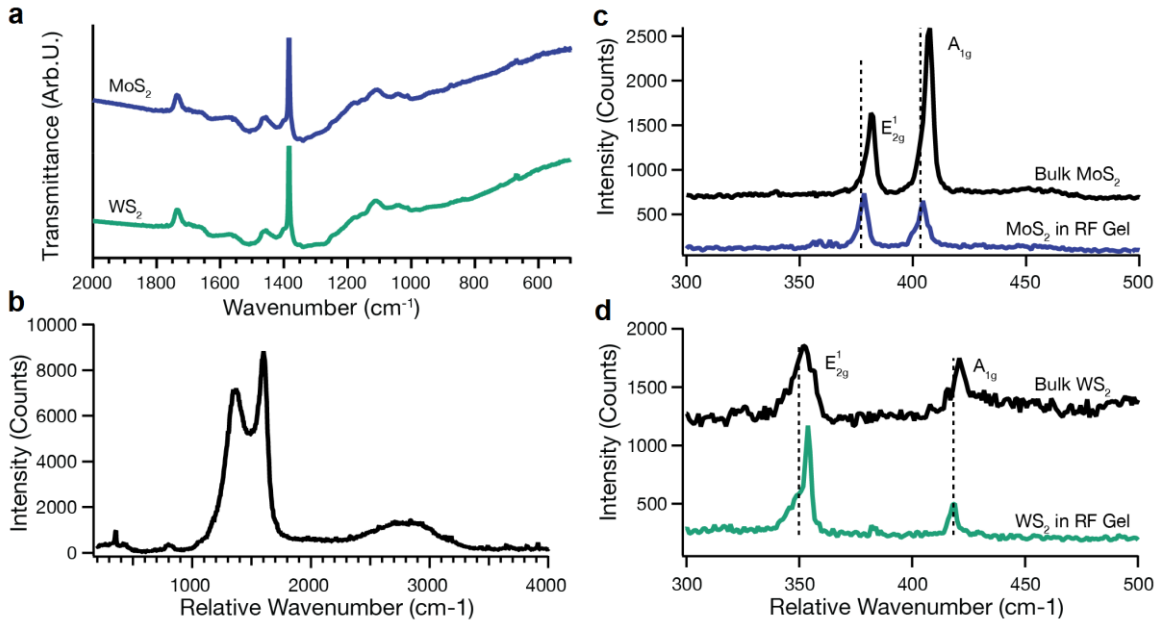

Figure 4.5. a) FTIR transmittance data of MA-17 and WA-17. **b)** Low-resolution Raman spectrum of WA-17. **(c, d)** Higher-resolution Raman spectra showing characteristic bands of MoS_2 (c) and WS_2 (d) dispersed within the carbonized RF matrix of the aerogel for samples synthesized from 17 mg mL^{-1} TMD dispersions. For each RF-supported TMD, the bulk Raman spectra is displayed offset for comparison. Vertical dotted lines represent peak centers of the in plane (E^1_{2g}) and out of plane (A_{1g}) modes of the exfoliated TMD's to emphasize the shift from their bulk counterparts due to exfoliation.

The low-resolution Raman spectrum of WA-17 shows both the D band at 1345 cm^{-1} and the G band at 1603 cm^{-1} (Figure 4.5b). The intensity ratio analysis of these bands (see Section 2.3.2) suggests that these aerogels contain graphitic grain sizes of 11 nm. Looking more closely at the low-wavenumber range, the TMD's—both as bulk powder and encapsulated within the carbon aerogel—exhibit E^1_{2g} and A_{1g} symmetry Raman active modes, which correspond to in-plane and out-of-plane stretching modes, respectively[143]. Similar to carbon, the distance and intensity ratio between these scattering modes gives information about the degree of electrical coupling between layers. The addition of more monolayers tends to increase the energy of the out-of-plane A_{1g} mode. While the TEM data do not suggest high exfoliation of the TMD's in the gels, the shift between peaks implies that there is a decrease in interlayer coupling, which could lead to

increased adsorption or intercalation of ions during supercapacitor operation. For WS_2, the spacing between the E^1_{2g} and A_{1g} peaks decreases from 69 cm^{-1} to 64 cm^{-1} after sonication, which implies that monolayers are electrically coupled to two nearby sheets (Figure 4.5d)[143,144]. This does not necessarily mean that the sheets were highly exfoliated, only that inter-layer coupling in the (001) direction decreased during processing. For MoS_2, there is a less distinct shift, which suggests that the exfoliated material is only slightly shifted from its bulk counterpart (Figure 4.5c). The exfoliated, dispersed E^1_{2g} peak sits at 378 cm^{-1} and the A_{1g} sits at 404 cm^{-1}, compared to 381 cm^{-1} and 407 cm^{-1} for the bulk material, leading to a difference of 26 cm^{-1} in both cases. A comparison to literature for the out-of-plane A_{1g} band shows that each MoS_2 remained coupled to only one other layer. However, the E^1_{2g} and peak spacing suggest the material retained its bulk-like characteristics[143,145].

4.3.3. Electrochemical Testing Results

As with the graphene aerogel, the specific capacitance of the pyrolyzed TMD aerogel supercapacitor electrodes was evaluated from the galvanostatic discharge profiles at each applied current, using the full voltage window of 0.9–0.1 V. However, we chose to characterize the TMD aerogel materials by volumetric capacitance, which can be obtained by multiplying gravimetric capacitance (Eq. 3, p. 26) by the bulk density of the active material. Although gravimetric capacitance is more often used as a figure of merit for supercapacitors, volumetric capacitance normalizes results for significant changes in the density of the active material, as is the case for our aerogels with different TMD concentrations. For example, the densities of RFA, MA-17, and WA-8.6 are 0.33, 0.61, and 0.90 g cm^{-3}. The wide range reflects the significant differences in the TMD densities—7.5 g cm^{-3} for WS_2 and 5.06 g cm^{-3} for MoS_2—as well as their molecular weights. For example, while the WS_2 comprises only 3.3 mol% of WA-17, it represents 41.5 wt%. Thus,

the resulting capacitances represent the interplay between the molar percentage of the TMD and the density, capacitance, surface area, and conductivity of the added TMD, as discussed below.

While TMD-free and TMD-loaded aerogels exhibited similar gravimetric capacitances (87.5 and 84.5 F g^{-1} maxima, respectively), the volumetric capacitance increased significantly upon the addition of TMD's (Figure 4.6d, Table 4.1). The WA-34 exhibited the greatest volumetric capacitance of the samples at 59.8 F cm^{-3} (64.7 F g^{-1}), 127% greater than RFA at 26.3 F cm^{-3} (87.5 F g^{-1}). Similarly, the MA-17 featured a large volumetric capacitance compared to the RFA, at 52.5 F cm^{-3} (84.5 F g^{-1}), as did the other WS_2-loaded aerogels. This marked improvement may be attributed to the reduction of inter-layer coupling in the TMD's accompanying sol–gel processing, as previously shown in Raman analysis. Additionally, the enhanced volumetric capacitance of the TMD-loaded aerogels suggests that they represent promising, scalable materials for high density supercapacitor applications, such as hybrid vehicles or portable electronics where space is constrained[146–149]. It is worth noting that all of our 2H TMD-loaded aerogel devices perform markedly better than devices based on pure, bulk 2H TMD (2–3 F g^{-1} to 40 F g^{-1}) and similarly to devices based on the 1T metallic phase of MoS_2 (~80 F g^{-1}) without pyrophoric materials.[127,150]

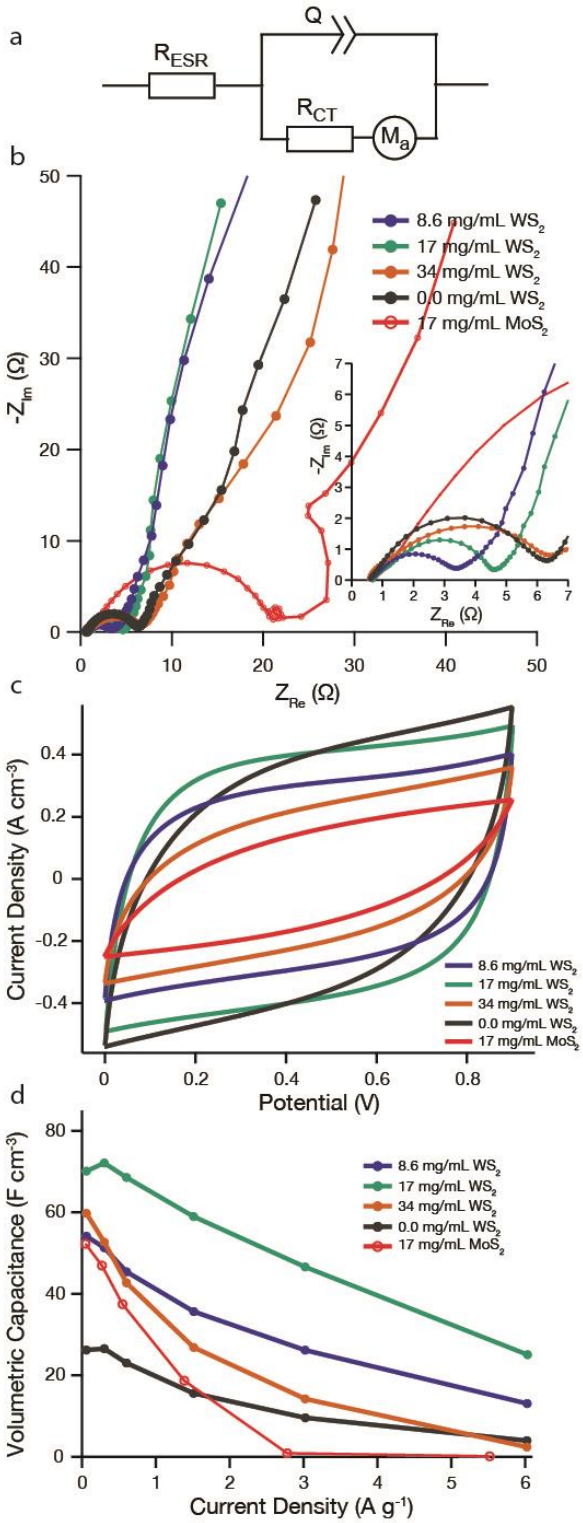

Figure 4.6. Electrochemical characterization of the pyrolyzed aerogels with different TMD mass loadings fabricated into coin cell supercapacitors, including **a)** equivalent circuit diagram, **b)** Nyquist plots from EIS (inset shows more detail of high–mid frequency range), **c)** cyclic voltammograms at sweep rate 20 mV s^{-1}, and **d)** specific volumetric capacitance as a function of applied current density from galvanostatic tests.

The addition of TMD's also improved the rate performance of the aerogels, as seen in Figure 4.6d. At the highest tested current, the specific capacitance of WA-8.6 was 24% of its maximum value, compared to 15% for RFA. However, WA-17, WA-34, and MA-17 exhibited more severe drop-offs than RFA. We hypothesize that the poorer capacitance retention of these samples, as well as RFA, is correlated with their higher charge transfer resistance, a value that is measured from impedance spectroscopy, as discussed below. In addition, WA-17 displayed excellent cycling stability, and actually improved its performance during the 2000 continuous charge–discharge cycles at 0.25 A g^{-1}. The WA-17 specific capacitance more than doubled between cycles 200 and 400, remaining 33% higher than its initial value at the final tested discharge. This enhanced capacitance during cycling may be due to additional exfoliation of the TMD or increased pseudocapacitance during charging and discharging, as observed by Bissett et al. for MoS_2–graphene composite electrodes.[151]

The EIS Nyquist plots (Figure 4.6b) can be modeled with the equivalent circuit in Figure 4.6a to inspect operational resistance as described in Section 2.3.4. This shows that R_{CT} increases with WS_2 loading, and that R_{CT} is much greater for MA-17 than WA-17 (~21 Ω vs. 3.9 Ω), despite the former having larger pore sizes, which would reduce ion transport resistance. We hypothesize that these trends in R_{CT} are related to the formation of Schottky barriers between semiconducting TMD's and metals.[152] Zhang et al. have observed the analogous formation of a Schottky junction at the interface of MoS_2 with sp^2 hybridized carbon in graphite, which they attributed to the existence of metallic edge states in MoS_2 nanosheets.[153] Fermi level pinning may be exacerbated in these devices because the aerogels are not composed of pristine graphite, but carbonized RF polymer, whose highly defective structure hosts many charge trapping sites. Additionally, while WS_2 and MoS_2 have similar bulk contact resistances, the incorporation of WS_2 likely does not

impact the overall charge transfer resistance of the aerogel as severely as MoS_2 due to differences in molar loading (Table 4.1). Alternatively, R_{CT} is associated with ion adsorption within the pores of the active material.[154] On this subject, an EIS study by Bissett et al. on supercapacitors with exfoliated TMD membrane electrodes in aqueous Na_2SO_4 electrolyte, showed that the ion adsorption in MoS_2 occurs on a much slower timescale compared to WS_2.[150] It is worth noting that R_{CT} values comparable to ours have been reported previously for coin cells containing bulk (2H phase) MoS_2 as the active material.[155]

Interestingly, R_{CT} of the RFA control is similar to WA-34 (5.7 Ω). This observation is consistent with previous studies of TMD-carbon composite supercapacitors where the addition of the TMD lowered R_{CT} from that of the plain carbon as well as the bulk TMD.[156,157] Like WA-34 and MA-17, the RFA has larger pores which would lower ionic resistance, but no TMD's to contribute to contact resistance within the electrode. In this case, we hypothesize that the larger R_{CT} is related to the significantly higher specific surface area (776 $m^2 g^{-1}$) and lower bulk density (0.33 g cm^{-3}) of the RFA due to the absence of TMD's, resulting in a more sparse 3D network of active material with poorer electronic conductivity whose effect is great enough to counteract the easier ion movement. In support of this claim, Yang et al. recently conducted a comprehensive study of pyrolyzed RF aerogel supercapacitors where the pore size was tuned by catalyst concentration.[158] They found that charge transfer resistance tended to increase in tandem with pore size and confirmed the high electronic resistance of samples with large pores by four-point probe measurements.

In contrast to R_{CT}, R_{ESR} is similar for all tested aerogels, ranging from 0.56–0.76 Ω. This is not surprising given the identical composition of the pyrolyzed RF matrix and identical construction of the coin cell devices for all samples. The slight increase in R_{ESR} for MA-17

compared to WA-17 reflects the difference in the electrical conductivity of the constituent bulk TMD's—0.9 S cm^{-1} for WS_2 versus 0.2 S cm^{-1} for MoS_2 at 300 K[130,159]. Mechanical integrity may also be responsible for the differences in series resistance, as the MA electrode amalgam had a stronger tendency to crack and flake apart during the flattening process, presumably due to the weak interlayer bonding of the TMD and its higher molar loading compared to WA-17.

Within the WS_2 aerogels, the knee frequency f_k increases with decreasing TMD loading—20, 28, and 54 Hz for WA-34, WA-17, and WA-8.6 respectively—although it drops to 14 Hz for the unloaded RFA. The larger charge transfer resistance of WA-34 and RFA likely accounts for the lower f_k, even though they have larger pores on average compared to the other samples, which would suggest less hindrance to ion diffusion within the electrode.[160] In fact, the very short 45°-sloped Warburg region preceding the steeper part of the line in these samples also suggests lower resistance to ion diffusion in the pores. The much lower f_k of MA-17 (4 Hz) compared to WA-17 is indicative of the former's much higher charge transfer resistance as well.

The wider pore size distribution of WA-34 and RFA also explains why these samples exhibit smaller slopes—corresponding to a lower phase angle—in the low-frequency region. With variation in pore sizes, the AC signal does not penetrate equally at a given frequency, since it is easier for ions to access larger pores than smaller pores, resulting in a shift from the theoretical vertical line of a capacitor. Song et al. developed a model to describe this particular frequency dispersion using a dimensionless frequency-dependent "penetrability" and a pore size distribution function, showing that the slope of the line in the Nyquist plot decreases for pore distributions with greater standard deviation.[161,162]

The Nyquist plot of MA-17 exhibits unusual characteristics at lower frequencies that are difficult to interpret. Between the semicircular R|C region and the steeply sloped constant phase

region, there is a small loop followed by a larger arc that curves back on the real impedance axis, instead of the expected 45° Warburg line. These features indicate low-frequency inductive behavior in the system, which is not typically observed in supercapacitors. We note, however, that these features also appeared for duplicate coin cells made with the same active material. One possible explanation is offered by Bisquert et al., who extensively studied inductive phenomena in the context of a porous, heterogeneous electroactive material composed of two different solids in contact with electrolyte[163]—a good model for our TMD/carbon aerogel composite electrodes. They found that inductive behavior resulted from the coupled dielectric relaxation in the two solid phases, with the relaxation being driven by changes in the electrochemical potential of the phases due to charge transfer between them.

The current–voltage plots from the 20 mV s^{-1} CV sweeps are shown in Figure 4.6c. While an ideal capacitor exhibits a rectangular shape, the voltammograms of the aerogel samples exhibit rounded corners, indicating resistance to ion diffusion that slows the current response. In agreement with EIS, the MA-17 shows the largest ion diffusion resistance, represented by a lens-shaped voltammogram. Similarly, WA-34 and RFA also have significantly distorted CV curves, while WA-8.6 and WA-17 have the most rectangular curves. The more rectangular CV shape of WA-8.6 and WA-17 is also corroborated by their higher knee frequencies compared to the other two samples. Additionally, as in the graphene aerogels, the lack of peaks and troughs in the voltammograms of the TMD-loaded aerogels indicate that no redox reactions occur over the tested voltage range and that the mechanism of capacitance is purely double-layer. While Na^+ ions are known to intercalate between the layers of TMD particles, they are unlikely to do so except at extremely low scan rates.[164,165]

Table 4.1. Summary of pyrolyzed TMD aerogel composite properties.

	Aerogel Sample				
Property	**MoS_2 17 mg/mL**	**WS_2 8.6 mg/mL**	**WS_2 17 mg/mL**	**WS_2 34 mg/mL**	**No loading**
TMD Mole %	6.70%	2.30%	4.40%	8.40%	0.00%
XRD Crystallite Thickness (nm)*	37	57	60	55	-
BET Surface Area (m^2 g^{-1})	408	500	620	514	776
Gravimetric Capacitance (F g^{-1}) †	84.5	60.3	56.2	64.7	87.5
Volumetric Capacitance (F cm^{-3})	52.5	54.2	50.9	59.8	26.3
Equivalent Series Resistance R_{ESR} (Ω)	0.76	0.60	0.68	0.56	0.60
Charge Transfer Resistance R_{CT} (Ω)	21	2.6	3.9	5.7	5.7
Knee Frequency f_k (Hz)	4	54	28	20	14

* in the (002) plane

† Capacitance values from galvanostatic discharge profile at lowest tested current density

4.4. Conclusion

To conclude this chapter, we have demonstrated a rapid, scalable nanomanufacturing process for the production of TMD–carbon aerogel composites. The process is similar to that employed to make graphene aerogels as described in the preceding chapter, relying on polycondensation of resorcinol and formaldehyde catalyzed with hydrochloric acid in acetonitrile, and illustrates the ease of incoporating other functional nanomaterial additives. Compared to typical aerogel processing (24 hours), the reaction presented here occurs in 2% of the time without sacrificing the narrow pore sizes or high surface areas of a standard RF aerogel. This synthesis outlines a general method to support TMD's with high electrical conductivity and porosity which is applicable to other stable TMD's. In addition, any novel advances in TMD synthesis or exfoliation can be directly incorporated via this process. Given the wide potential range of uses of TMD's, including

electrochemical, photovoltaic, and catalytic applications, their efficient synthesis will enable rapid, combinatorial optimization of design parameters to engineer new devices. As a proof of concept, we explored the performance of MoS_2 and WS_2-loaded carbon aerogels as electrodes for supercapacitors. An initial screening of device performances indicates that the addition of TMD's yields electrodes that are cyclically stable and offer volumetric capacitances up to 127% higher than pyrolyzed RF alone. Further, the ability to rapidly process new materials into composites is magnified by the range of applications for high-surface-area, conductive supports, and we believe this scalable manufacturing methodology will find widespread use.

Chapter 5. Patterning of Graphene Oxide with Optoelectronic Tweezers[4]

5.1. Introduction

While the benefits of loading aerogels with low-dimensional, layered nanomaterials such as graphene/GO and TMDs are evident from our supercapacitor studies, they could be made even greater by aligning the nanomaterials in bulk to create a "textured" aerogel. In particular, a textured aerogel would offer much better physical properties compared to an aerogel with randomly oriented sheets, considering that such properties—including electrical conductivity, thermal conductivity, and mechanical strength—are orders of magnitude greater within a layer than perpendicular to it, owing to the weak interlayer bonding. For supercapacitor electrodes, vertically aligning the sheets in the aerogel relative to the current collector would create facile, deeper diffusion pathways for ions in the electrolyte, reducing ohmic losses and increasing rate capability. In principle, such an aerogel could be synthesized by a similar sol–gel approach with RF as described previously, but with simultaneous alignment of the nanomaterial additive. In this chapter, as a first step toward these goals, we demonstrate large-scale alignment along with precise positioning of GO particles in water using a non-contact optical manipulation technique known as optoelectronic tweezers (OET).

Introduced by P-Y Chiou and colleagues in 2005,[166] OET has been used trap and translate such diverse micrometer- to nanometer-scale materials as polystyrene spheres,[166] live cells,[166] silver and silicon nanowires,[167] and both single- and multi-walled carbon nanotubes.[168,169] OET relies on the phenomenon of dielectrophoresis (DEP), in which a non-uniform electric field

[4] This chapter is in preparation and will be published. It is entirely my own work, with valuable advice provided by Xuezhe Zhou, Bennett E. Smith, and Peter J. Pauzauskie.

induces a dipole in a dielectric particle, which then experiences a force proportional to the gradient of the squared electric field. Depending on the properties of the particle, the medium, and the applied field, the DEP force can be either repulsive ("negative DEP") or attractive ("positive DEP") toward the region of highest field gradient; OET takes advantage of the latter to trap and manipulate particles. High-aspect ratio particles like GO exhibit an enhanced DEP force relative to spherical particles, making them particularly suited to OET.[167] In addition, the applied electric field will exert a torque on such particles due to their anisotropic polarizability; GO will rotate to align its basal plane parallel to the field, due to its polarizability being greater in-plane than out-of-plane.[170] This is the means by which large-scale vertical alignment of particles is achieved in tandem with manipulation. Furthermore, unlike conventional DEP manipulation techniques, where fixed, lithographically patterned metallic electrodes are used to trap particles, the DEP force in OET is optically induced, allowing structures of particles to be reconfigured in real time by changing the pattern of light that is projected onto the OET device.

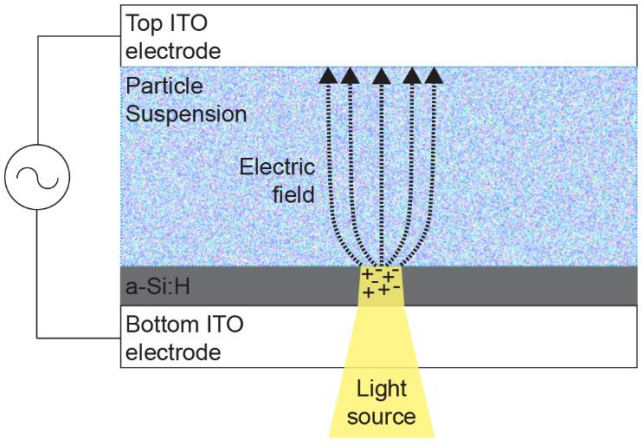

Figure 5.1. Schematic diagram of an optoelectronic tweezers (OET) device.

Figure 5.1 depicts the structure of the OET device used in our investigations. The liquid suspension containing the particles of interest is sandwiched between two parallel transparent electrodes made of indium tin oxide (ITO)-coated glass, across which an AC bias is applied. The

ITO on the lower electrode is further coated with photoconductive hydrogenated amorphous silicon (a-Si:H). Under normal conditions, most of the voltage drops across the a-Si:H layer. However, if focused visible-wavelength light is projected onto the lower electrode, the impedance of the a-Si:H in the illuminated region drops by several orders of magnitude due to the creation of electron–hole pairs. This transfers voltage to the liquid layer and locally bends the electric field lines, producing the DEP force which, if positive, drives nearby suspended particles toward the edge of the illuminated region, where the field gradient is highest. Electric field gradients significant enough for trapping can be produced at optical intensities on the order of 10 W cm^{-2}, mitigating the undesirable photochemical or photothermal heating effects that are commonly encountered with the more established optical manipulation technique of optical tweezers, which uses intensities as high as 10^7 W cm^{-2}.[171,172] The low intensity requirement of OET also makes it possible to trap particles with focused light from commercial digital projectors in addition to laser sources, allowing for easy creation and reconfiguration of trapping patterns with computer presentation software.

Using OET during the synthesis of GO–RF gels, the GO platelets would not only be vertically aligned, but their positioning and density could be manipulated individually or collectively during the initial stages of the gelation process by adjusting both AC-field parameters as well as characteristics of the projected light used to trap the sheets. Specifically, one could organize individual GO sheets into a user-defined configuration using multiple light traps arranged in that pattern, provided that the spacing between the traps is small enough to trap individual GO sheets rather than clusters. The density of the GO configuration could then be tuned by bringing the spots of light either closer together or farther apart, and bulk density variations in the nascent gel could be achieved by selectively adjusting the density of the optical trapping pattern in different

regions. OET would therefore enable the formation of customizable, textured graphene aerogels from initially dilute suspensions of GO. The same patterning approach could be applied to any other nanomaterial capable of being trapped with OET, as a way to make large-scale textured arrays or composites customized to the intended application. Supercapacitor electrodes, in particular, would be well-suited for OET-based nanomanufacturing due to their thin profile (≤ 150 μm).

Herein, we report the vertical alignment, trapping, movement, and patterning of GO in an OET device for the first time, for both single particles and aggregates of particles. Additionally, we outline a simple theoretical model for OET manipulation of a single GO particle, which can be used to select the appropriate applied bias and speed at which to move the optical trap such that the particle aligns with the field and remains confined.

5.2. Theory of OET

To use OET on GO in an informed manner, it is necessary to understand the dielectrophoretic response and hydrodynamics of individual GO particles. Importantly, knowledge of the drag force on a trapped GO particle would enable selection of the appropriate electric field strength and rate at which to translate the trap such that the particle aligns with the field and remains confined. The following three sections present a theoretical model for the alignment, trapping, and translation of a single GO particle in an OET device.

5.2.1. Dielectrophoresis Force

For a generic particle in a nonuniform sinusoidal electric field, the time-averaged DEP force on the particle is:[173]

$$\boldsymbol{F_{DEP}} = \frac{\mathbf{1}}{\mathbf{2}}\mathbf{Re}[\boldsymbol{\alpha}^*]\boldsymbol{\nabla E_{RMS}^2} \quad \textbf{(5.1)}$$

where $\mathrm{Re}[\alpha^*]$ is the real component of the particle's complex effective polarizability and E_{RMS} is the root-mean-square value of the electric field. Since GO has a sheet-like structure with micron-scale in-plane size but nanoscale thickness, it can be approximated as an oblate spheroid with its semi-minor axis a much smaller than its semi-major axis b ($a/b \equiv \gamma \ll 1$). In addition, as previously mentioned, when a voltage is applied across the OET device, a GO particle will rotate to align its basal plane, i.e. its major axis in the oblate spheroid model, parallel to the electric field. For an oblate spheroid oriented as such, the complex polarizability along the major axis is:[174]

$$\boldsymbol{\alpha_b^* = v\varepsilon_m \frac{\varepsilon_p^* - \varepsilon_m^*}{L_b\varepsilon_p^* + (1-L_b)\varepsilon_m^*}} \quad \textbf{(5.2)}$$

where v is the volume of the spheroid ($= (4/3)\pi ab^2$), and ε_p^* and ε_m^* are the complex permittivities of the particle and the medium, respectively. The complex permittivity is equal to $\varepsilon^* = \varepsilon + i(\sigma/\omega)$, where ε, σ, and ω are the real permittivity, electrical conductivity, and frequency of the AC field, respectively. L_b is a shape- and direction-dependent parameter called the depolarization factor. For an oblate spheroid along the major axis this is:

$$\boldsymbol{L_b = -\frac{\gamma^2}{2M} + \frac{\pi\gamma}{4M^{1.5}} - \frac{\gamma}{2M^{1.5}} \arctan\left(\left(\frac{\gamma^2}{M}\right)^{1/2}\right)} \quad \textbf{(5.3)}$$

and $M = 1 - \gamma^2$, where $\gamma \equiv a/b$. Since $\gamma \ll 1$ for GO, $M \approx 1$ and thus L_b reduces to $\pi\gamma/4$. Substituting Equation 5.2 into Equation 5.1 yields the final expression for the DEP force:[175]

$$\boldsymbol{F_{DEP} = \frac{3}{2} v\varepsilon_m \mathrm{Re}\left[\frac{\varepsilon_p^* - \varepsilon_m^*}{C\varepsilon_p^* + D\varepsilon_m^*}\right] \left|\nabla E_{RMS}^2\right| = \frac{3}{2} v\varepsilon_m \mathrm{Re}[f_{CM}^*] \left|\nabla E_{RMS}^2\right|} \quad \textbf{(5.4)}$$

where $C = 3L_b \approx 3\pi\gamma/4$, $D = 3(1 - L_b) \approx 3(1 - \pi\gamma/4)$. The term $f_{CM}^* = \left(\varepsilon_p^* - \varepsilon_m^*\right)/\left(C\varepsilon_p^* + D\varepsilon_m^*\right)$ is the Clausius–Mossotti (CM) factor, whose real part can be used as a relative measure of the strength of the DEP force on a given particle. In addition, the attractive or repulsive nature of the DEP force, in regard to the region of greatest electric field gradient, is determined by whether

$\mathrm{Re}[f_{CM}^*]$ is positive or negative, respectively. For spherical particles, $\mathrm{Re}[f_{CM}^*]$ is fixed between -0.5 and 1,[176] while high-aspect ratio particles such as GO and Pd nanowires, as we will see later on, can have CM factors that are orders of magnitude higher.

To obtain $|\nabla E_{RMS}^2|$, finite element simulations of the electric field produced at a virtual electrode in the OET device were performed with COMSOL Multiphysics, using a 2D axisymmetric model. The results are shown in Figure 5.2a assuming a circular illuminated region 5.8 μm in diameter and power 3.49 μW (measured values from one of our single-particle trapping experiments), 7 V_{pp} and frequency 500 kHz. The effect of the GO particles on the electric field distribution in the fluid was not considered. A Gaussian distribution in the conductivity of the a-Si:H layer was used to approximate the effect of the incident light.

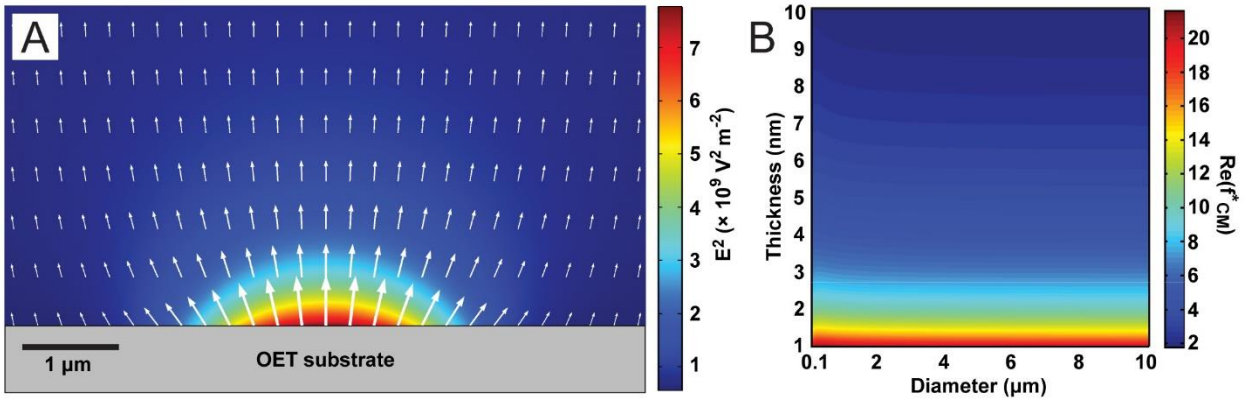

Figure 5.2. a) Simulation of the electric field *E* (arrows) and ∇E^2 (color plot) in the GO suspension near the OET substrate for an applied bias of 7 V_{pp}, 500 kHz and an illuminated region 5.8 μm in diameter. **b)** Calculated values of the real Clausius–Mossotti factor of GO in water at 500 kHz for a range of particle thicknesses and diameters.

5.2.2. Evaluation of Clausius–Mossotti Factor

To calculate the CM factor for a particle of GO, its complex permittivity must be known, which in turn requires its electrical conductivity to be known. However, we cannot simply use the bulk conductivity of GO for this purpose due to the aqueous nature of the system. GO in water will exhibit an additional surface conductivity on top of its bulk conductivity due to the movement of counterions (H_3O^+ or H^+, in this case) in the electric double layer that forms around the particle.

Owing to the insulating nature of bulk GO (whose room-temperature resistivity is greater than 10^{11} Ω cm)[177], this surface conductivity could be significant. O'Konski showed that the effective conductivity of a circular disk with thickness 2*a* and diameter 2*b*, assuming a homogeneous internal electric field, can be expressed as:[178]

$$\boldsymbol{K_{eff,\perp} = K_B + \frac{(a+b)K_S}{ab}} \text{ and } \boldsymbol{K_{eff,||} = K_B + \frac{2\,K_S}{b}} \quad \textbf{(5.5)}$$

where $K_{eff,\perp}$ is the effective conductivity in the in-plane direction, $K_{eff,||}$ is the effective conductivity in the out-of-plane direction, K_B is the bulk conductivity, and K_S is the surface conductance. For the case of GO, where a << b and the bulk conductivity is negligible, the above expressions simplify to:

$$\boldsymbol{K_{eff,\perp} = \frac{K_S}{a}} \text{ and } \boldsymbol{K_{eff,||} = \frac{2\,K_S}{b}} \quad \textbf{(5.6)}$$

Since a << b, $K_{eff,\perp} \gg K_{eff,||}$. Therefore we use $K_{eff,\perp}$ for σ in the calculation of the CM factor.

The surface conductance K_S can be related to the surface charge density σ_S by:

$$\boldsymbol{K_S = \sigma_S \mu_i} \quad \textbf{(5.7)}$$

where μ_i is the mobility of the counterion in the double layer, which we have assumed to be the same as the mobility of H^+ in bulk distilled water ($3.6 \cdot 10^{-7}$ m^2 V^{-1} s^{-1}), although it is usually slightly lower.[170,179] σ_S, in turn, can be calculated from the Grahame equation,

$$\boldsymbol{\sigma_S = \sqrt{8kT\varepsilon_m \rho_\infty}\ \sinh\left(\frac{ze\zeta}{2kT}\right)} \quad \textbf{(5.8)}$$

where ρ_∞ is the concentration of the counterion in bulk solution, *z* is its valency, and ζ is the electrokinetic (zeta) potential. Since the counterion here is H^+, *z* = 1, and ρ_∞ can be easily found by measuring the pH of the GO dispersion. ζ can be measured from light-scattering techniques. The pH of a 0.1 mg mL^{-1} dispersion of GO (a typical concentration used for OET manipulation) was measured to be 5.0, giving $\rho_\infty = [H^+] = 1.0 \cdot 10^{-5}$ M. The zeta potential of the dispersion

was -47.8 mV, an average of three measurements taken with a Malvern Zetasizer Nano ZS. Based on these values and assuming T = 20°C, $\sigma_S = 4.1 \cdot 10^{-4}$ C m^{-2} and $K_S = 1.5 \cdot 10^{-10}$ S.

The other necessary parameters to determine the CM factor were obtained as follows. The electrical conductivity of the 0.1 mg mL^{-1} GO dispersion (σ_m) was measured directly as 16 μS cm^{-1} using a Horiba Twin Cond conductivity meter. The real permittivities of water and GO—80.1 and 4.3 respectively—were taken from the literature.[180,181] Room temperature was assumed for all parameters since the temperature of the GO dispersion does not vary appreciably during OET operation, based on ratiometric thermometry and finite element simulations (Section 5.4.3).

Figure 5.2b shows calculated values of $\mathrm{Re}[f_{CM}^*]$ of GO in water at 500 kHz for typical particle dimensions. The calculations confirm that GO can be trapped with OET, due to the positive sign of $\mathrm{Re}[f_{CM}^*]$, and that GO experiences much stronger DEP forces than a spherical particle of equivalent volume, as $\mathrm{Re}[f_{CM}^*]$ is much greater than 1, particularly for thinner flakes.

5.2.3. Stokes Drag Force

The DEP force on a GO platelet in an OET trap is opposed by hydrodynamic drag, which in this case is completely viscous in nature due to the low Reynolds number (< 10^{-2}). While analytical expressions of the drag force on a particle in an infinite bath are well-established for a variety of geometries, they cannot be used for OET analysis due to the proximity of the trapped particle to the a-Si:H substrate where the electric field gradient is highest. This imposes a boundary condition that increases the drag force relative to an infinite medium.[182]

During the manipulation of colloidal GO sheets with OET, the particle translates edgewise parallel to the substrate, with its basal plane perpendicular to the substrate due to the vertical alignment induced by the applied electric field (~1 kV cm^{-1}). Although we could not find an exact expression in the literature to calculate the translational drag force on a thin spheroid near a wall

that matches this situation, Davis[183] analytically derived an expression for the Stokes drag force on an arbitrarily oriented disk near a plane wall to order D^{-3}, where D is the distance of the disk axis from the wall normalized to the disk radius. This is another suitable approximation for the shape of GO owing to its very small thickness compared to its in-plane dimension. The drag force derived by Davis for the orientation whereby the disk is moving edgewise at constant speed parallel to the wall, with the plane of the disk perpendicular to the wall, is:

$$\boldsymbol{F_D = -16\mu bU\left(\frac{2}{3}\cdot\frac{1}{1-1/(\pi D)} - \frac{1}{18}\cdot\frac{1}{\pi D^3}\right)} \quad \textbf{(5.9)}$$

where μ is the dynamic viscosity of the medium, b is the disk radius, and U is the disk speed. While the actual separation distance of a GO flake from the a-Si:H during OET manipulation is difficult to measure experimentally, using the above $O(D^{-3})$ solution with $D = 1$ yields a theoretical lower bound for the drag force, $F_D \approx -16\mu bU \cdot 0.960$, which is more accurate than the infinite-medium drag force.

At mechanical equilibrium, the drag force on the GO flake will be equal in magnitude to the horizontal (x) component of the DEP force at that location. Although several other forces may act on the trapped particle during OET operation, they are negligible for our experimental parameters (see Section 5.2.4).[184] Since the drag force is proportional to the particle velocity by Equation 5.9 and the DEP force is independent of particle velocity, there will be a limiting velocity above which the drag force will exceed the DEP force and the particle will fall out of the OET trap. Therefore, a theoretical upper bound for the maximum allowable translation speed, at a given applied voltage and frequency, can then be obtained by equating the drag force to the maximum magnitude of the DEP force x-component and solving for U. It is assumed that the disk radius in the drag force expression is equal to the spheroid semi-major axis in the DEP force expression.

$$U_{max} = \frac{\pi a b \varepsilon_m \mathrm{Re}[f_{CM}^*] \left| \left(\nabla E_{RMS}^2\right)_x \right|_{\max}}{8\mu\left(\frac{2}{3}\cdot\frac{1}{1-1/(\pi D)} - \frac{1}{18}\cdot\frac{1}{\pi D^3}\right)} = \frac{\pi a b \varepsilon_m \mathrm{Re}[f_{CM}^*] \left| \left(\nabla E_{RMS}^2\right)_x \right|_{\max}}{8\mu(0.960)} \quad \textbf{(5.10)}$$

5.2.4. Other Negligible Forces

During OET manipulation, several other forces act on the particle of interest in addition to the DEP and drag forces. However, we find these to be negligible for our experiments, as discussed below.

Electrothermal convection arises in tandem with heating in the a-Si:H or liquid layer, which could be Joule heating from the applied voltage, dielectric heating from the alternating nature of the electric field, and/or photothermal heating from the incident light. This creates gradients in the permittivity and electrical conductivity of the liquid that interact with the electric field to produce flow. A related phenomenon is buoyancy-driven flow, which results from density gradients in the liquid due to the temperature gradient. However, as we will prove in Section 5.4.3, temperature gradients in the liquid are negligible for our OET operational parameters, and thus the above two forces can be disregarded.

One force that does not depend on heating is electroosmotic flow, which is a consequence of the electric double layer that forms at the a-Si:H surface when a liquid containing dissolved ions is introduced to the OET chamber. When an AC voltage is applied across the two electrodes of the chamber and the a-Si:H is locally illuminated to produce a tangential electric field component, ions in the diffuse layer will move in response to the field, dragging bulk solution along and creating a flow field. However, for a bias of 20 V_{pp} and optical power density of 250 W cm^{-2} in the trap, electroosmotic effects only become significant below a frequency of ~1 kHz.[184] Given that our experimental optical power density (~13 W cm^{-2}) is much lower and bias frequency (500 kHz) is much higher than these values, we can disregard electroosmotic flow.

Additionally, despite the lack of buoyancy-driven flow in the liquid, the particle itself experiences an upward buoyant force, which is proportional to its size:

$$\boldsymbol{F_B = v(\rho_p - \rho_m)g} \quad \textbf{(5.11)}$$

where v is the volume of the particle, ρ_p and ρ_m are the densities of the particle and medium respectively, and g is the acceleration due to gravity. Nevertheless, if we take a large GO platelet having diameter 16.3 μm and thickness 3 nm (particle 3 in Figure 5.4), and assume the density of GO to be the same as that of graphite (2260 kg m^{-3}), the buoyant force is less than 2 percent of the maximum vertical component of the DEP force, even when the applied bias is only 1 V_{pp}, 500 kHz. Thus, we can treat the buoyant force as negligible as well.

5.3. Experimental Methods

5.3.1. OET Manipulation

To experimentally verify the theoretical framework described in Section 5.2, we determined the maximum achievable speeds for water-dispersed GO particles trapped in a homemade OET device at different applied biases. Our OET device has a 1-μm coating of a-Si:H on the bottom ITO electrode, with two strips of double-sided tape maintaining a ~92 μm separation from the top electrode. This space was filled with a 0.1 mg mL^{-1} dispersion of commercial few-layer GO (CheapTubes) in water, pre-sonicated to break up aggregates. The device was then mounted for sample observation in an optical microscope, equipped with a Princeton ProEM electron-multiplying charge coupled device camera (EMCCD) and a Newport motorized microscope stage with customizable speed. A 633-nm HeNe laser (spot width 5.8 μm, power 3.49 μW), focused with a long working distance 20x objective lens, was used to actuate the a-Si:H layer and trap the particle of interest at an applied voltage of 1–13 V peak-to-peak (V_{pp}) and frequency 500 kHz from

a function generator (Agilent 33220A). The stage holding the OET device was then translated uniaxially at increasing speeds until the particle fell out of the trap.

To calculate the theoretical maximum speeds for our experimentally manipulated particles based on our model, the diameter of the circumscribing circle of each particle was used as the spheroid or disk diameter ($2b$) in the DEP and drag force calculations respectively, and was estimated from optical microscope images of the free particle. Also, since particle thickness, another required parameter, could not be reliably measured in the optical microscope, it was assumed to be 3 nm based on atomic force microscopy measurements of representative particles and information from the GO supplier that the sample was 2–4 layers thick. This yields an effective in-plane conductivity ($K_{eff,\perp}$) of 0.098 S m^{-1} (Equation 5.6).

For multi-particle aggregation and patterning, the same OET setup was used with the same commercial GO sample, except that a more concentrated 0.5 mg mL^{-1} dispersion was used. To observe aggregation, the HeNe laser was focused on the device and held fixed under bias as particles fell into the trap. *In situ* Raman measurements were conducted with the same dispersion, but using a 532 nm single-mode Nd:YAG laser as the excitation source with 0.9 mW power and 60 s exposure time. The laser was focused onto the sample with a long working distance 50x objective lens (Mitutoyo). The scattered light was collected with the same objective and directed into an Acton SpectraPro-500i spectrometer with a 1200 lines/mm grating and liquid nitrogen-cooled CCD detector. For both single and multi-particle experiments, laser power was measured with a ThorLabs hand-held power meter. OET patterning was achieved using a commercially available DLP projector (BenQ) with a digital micromirror device (DMD) instead of a laser as the light source. Trapping patterns were controlled with Microsoft PowerPoint presentation software and focused to microscopic size onto the sample with a convex lens in front of the projector.

5.3.2. In-Situ Thermometry

During OET operation, the temperature of the trapping medium may exceed room temperature due to Joule heating from the applied voltage, dielectric heating from the alternating nature of the electric field, and photothermal heating of the a-Si:H layer from the incident light. The illumination of a-Si:H contributes extra Joule heating as well, due to the photoconductive nature of the material. To check for heating, we performed ratiometric in-situ thermometry experiments with Yb^{3+}/Er^{3+} co-doped $NaYF_4$ nanowires, based on the work of Vetrone et al.[185] Hexagonal β-$NaYF_4$:Yb^{3+},Er^{3+} nanowires were synthesized with dopant concentrations of 10% Yb^{3+} and 1% Er^{3+} via a hydrothermal process adapted from Zheng et al.[186] They were then introduced into a 0.1 mg mL^{-1} GO suspension in water. In such nanocrystals, the intensities of the green fluorescence bands of the Er^{3+} dopant ions follow a Boltzmann distribution, i.e. $\ln(R_1/R_2) \propto 1/T$, where T is the absolute temperature, R_1 is the integrated intensity of the band emanating from the transition $^2H_{11/2} \rightarrow {}^4I_{15/2}$ (centered at 525 nm), and R_2 is the integrated intensity of the band emanating from the transition $^4S_{3/2} \rightarrow {}^4I_{15/2}$ (centered at 545 nm). This means that the temperature of the suspension at different applied voltages can be extracted by correlating $\ln(R_1/R_2)$ in the corresponding photoluminescence spectra to a calibration curve of $\ln(R_1/R_2)$ versus $1/T$ for the same suspension at known temperatures.

For our experiments, spectra of the GO / $NaYF_4$:Yb^{3+},Er^{3+} suspension were measured at applied biases of 0, 1, 2, 3, 5, 7, 10, and 13 V_{pp} and 500 kHz (the same parameters that were used in our single-particle translation experiments) using a focused 975 nm diode laser with power 4.95 mW as the excitation source. The calibration data was obtained with the same excitation source from room temperature to 50°C by placing the sample in a temperature-controlled imaging chamber (Warner Series 30). Photoluminescence was collected with the aforementioned Acton

SpectraPro-500i spectrometer with a 300 lines/mm grating.

5.4. Results and Discussion

5.4.1. Single-Particle Manipulation

Figure 5.3 depicts an example of a single-particle experiment on a GO platelet that is approximately 5.2 μm across at its widest. With only the laser, the platelet remains in Brownian motion. However, when a bias of 5 V_{pp} and 500 kHz is applied simultaneously, the platelet rotates to align its basal plane with the electric field. This causes the particle to appear as a line, since the field is approximately normal to the OET substrate and coverslip through which the observation is conducted. When the laser spot is moved sufficiently close to the particle, it falls into the illuminated area within about 11 seconds, and then follows the light as the beam is moved downward in the viewing area. When the bias is removed, the particle resumes Brownian motion with no preferred orientation and slowly migrates away from the laser spot.

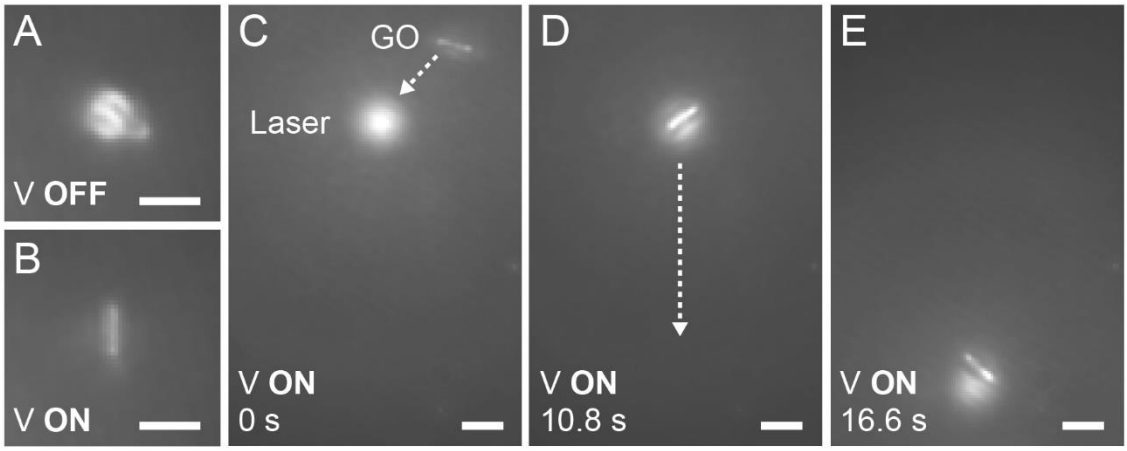

Figure 5.3. Trapping and translation of a single GO particle. The location of the laser spot used as the trap is indicated by the solid circle. **a)** No bias is applied to the OET device and the particle is in Brownian motion. **b)** Voltage (5 V_{pp}, 500 kHz) is turned on and the basal plane aligns with the electric field. **c)** HeNe laser is moved close to particle to induce trapping. **d)** The particle has fallen into the trap, and, **e)** follows the light as it is moved down in the field of view. (scale bar in each panel = 5 μm)

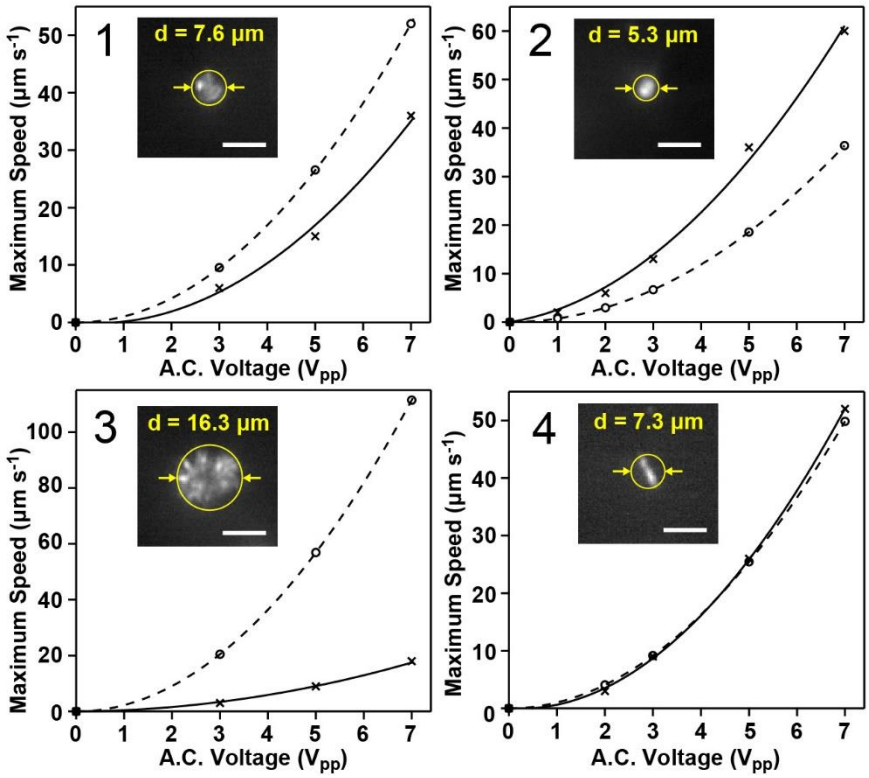

Figure 5.4. Maximum trapping speed of GO particles at different voltages at 500 kHz. Solid lines denote experimentally measured values while dashed lines denote theoretical maximum speeds based on DEP and drag force analysis. Insets show optical microscope images of each particle with circumscribing circle and diameter above (scale bar = 10 µm).

The experimental and theoretical maximum translation speeds for 4 GO platelets from the single-particle OET experiments are shown in Figure 5.4. Above 7 V_{pp}, some GO particles were observed to adhere irreversibly to the a-Si:H surface after being trapped, which is why the presented data is truncated at that voltage. Such immobilization has been previously reported for OET-based manipulation of gold nanoparticles and carbon nanotubes and is due to the combination of DEP force, which is strongest at the OET substrate, and electrophoretic forces from the particle surface charges.[187] Future studies could be directed toward passivating the substrate to make it less favorable for physisorption of GO.

The predicted maximum speeds for each particle are within an order of magnitude of their actual speeds, which is good agreement considering the numerous approximations that were made

for the calculation. It should be re-emphasized that the maximum particle speed was calculated as an upper bound that is less accurate for larger particles than smaller particles, since the error is measured in terms of $1/D$ (the inverse of the particle-wall distance normalized to the particle radius). Consistent with this, the estimate of the maximum speed was the most conservative (~6 times the measured speed) for particle 3, which was the largest of the 4 particles, having a diameter of 16.3 μm. For particle 1, the second-largest, with a diameter of 7.6 μm, the predicted maximum speeds were about 1.5 times higher than the measured values. Interestingly, the predicted speeds for particle 4 almost exactly match the measured values, whereas the predicted speeds for particle 2 are actually lower than the measured values (by a factor of ~0.5), despite the predicted speed being a theoretical upper limit.

One source of this discrepancy is our assumption that the GO particles are spheroids or circular disks for our DEP force and Stokes drag force calculations. AFM and TEM measurements in the literature show that GO possesses a highly irregular geometry, with respect to not only its overall shape but also its surface topography, having numerous steps, creases, and holes.[188,189] Although the effects of such irregularities are difficult to quantify and are beyond the scope of this report, a useful theorem by Hill and Power[190] states that the drag coefficient of an arbitrary particle in Stokes flow is at least that of the inscribing sphere and at most that of the circumscribing sphere. Since the circumscribing circle of the GO particle was used as the surface of the representative disk for our drag calculation, the calculated drag force would be greater than the actual value. If the magnitude of this overestimate is greater in magnitude than the underestimate from the Davis wall correction, then the maximum velocity would be underestimated. On the other hand, the folds, steps, and pores on the GO surface, whose size scale is significantly smaller

compared to the particle as a whole, likely have a negligible effect on the drag force of the particle owing to the fact that Stokes flow is not sensitive to sharp edges.[191]

Another geometric inaccuracy lies in our assumption that all GO particles are 3 nm thick, when a thinner or thicker particle with the same in-plane dimension would have a larger or smaller CM factor respectively and therefore experience a larger or smaller DEP force respectively. The difference is more pronounced going down in thickness, as seen in Figure 5.2b. For example, for particle 4, which had a measured diameter of 7.3 μm, the CM factor assuming a thickness of 3 nm is 6.5, but for a thickness of 1 nm (single layer) it is 20.3, resulting in a calculated maximum speed that is ~4% higher due to the greater DEP force.

Finally, the discrepancy in maximum speed for our particles could stem from non-geometric factors, such as the presence of ions other than H^+ in the GO dispersion, which were not considered. If there were residual metal, chloride, and sulfate ions from the Hummers method[192] that was used to synthesize the GO, they would cause the Debye screening length in the dispersion to be larger than predicted, thereby increasing the surface conductance of GO, the real CM factor, and the maximum speed.

5.4.2. Multi-Particle Manipulation

In addition to single-particle manipulation, we demonstrate the trapping of multiple GO particles simultaneously in a virtual electrode, which is necessary to realize large-scale patterns and local density gradients with OET. In a 0.5 mg mL^{-1} GO suspension, a single static optical trap formed by the 633-nm HeNe laser, with intensity similar to that from our single-particle experiments, can collect all the nearby GO platelets within 32 seconds when a bias of 20 V_{pp}, 500 kHz is applied (Figure 5.5a, b). To demonstrate this aggregation capability non-visually, Figure 5.5c shows the superimposed Raman spectra of a 0.5 mg mL^{-1} GO suspension in an OET device with and without

an applied bias of 20 V_{pp}, 500 kHz. The 532-nm Nd:YAG laser used as the Raman excitation source (power 0.9 mW) also actuates the a-Si:H, creating an optical trap when the bias is applied. The resulting aggregate of GO is dense enough after one minute to produce noticeable D and G bands in the Raman signal, at ~1350 and 1600 cm^{-1} respectively, that are characteristic of graphitic materials.

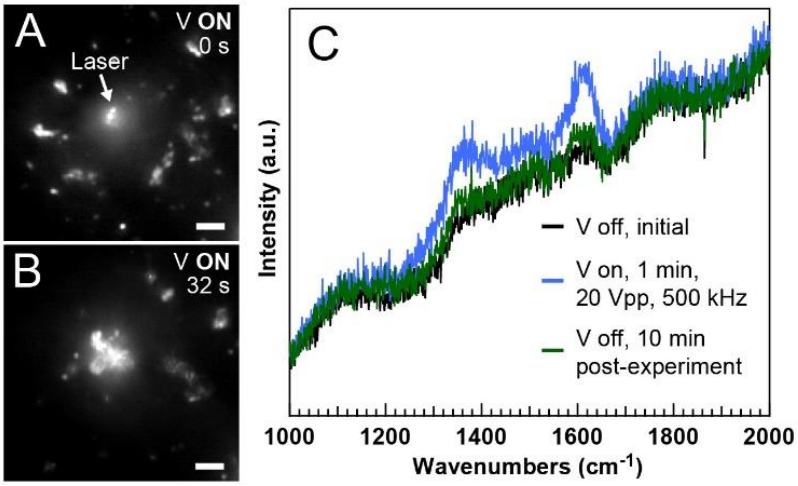

Figure 5.5. Multi-particle aggregation. **(a)** A bias (20 V_{pp}, 500 kHz) is applied to the OET device and a focused laser beam creates a trap. **(b)** In less than one minute, all the nearby GO particles are trapped in the spot (scale bar = 10 μm). **(c)** Raman spectrum of GO suspension in OET device with (blue) and without (black, green) bias of 20 V_{pp}, 500 kHz.

Finally, we show that GO can be manipulated in our OET device not only with a laser but also with a commercial DLP projector, which offers tremendous advantages as an actuator over lasers due to its lower cost, availability, and ease of use. Furthermore, using a projector allows for massively parallel and dynamic processing of particles since it can create many virtual electrodes simultaneously and move them around in a predefined manner, controlled by simple presentation software. Figure 5.6 shows a series of still images from the trapping and aggregation of GO particles in a 0.5 mg mL^{-1} aqueous dispersion using a dynamic array of dots from a digital projector. Given that the light from the projector is less intense than the laser, higher voltages must be used to induce trapping. Nevertheless, a bias of 20 V_{pp} and 100 kHz results in sufficient

DEP force to collect nearby GO particles to each of the four projected dots of light. As the dots are moved closer together and eventually merge into a single illuminated area over the course of 1 minute, the trapped particles move in tandem with each dot until they are all clustered in the middle. This experiment vividly illustrates how GO can be formed into arbitrary patterns and locally enriched with OET, as opposed to simply being moved around.

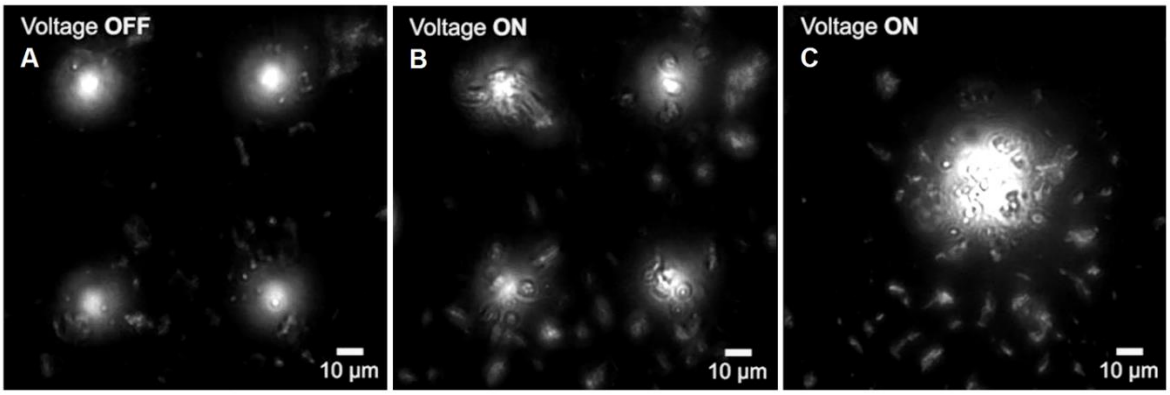

Figure 5.6. Large-scale patterning of GO with a digital projector. **a)** An array of four illuminated dots in projected onto the suspension. **b)** Bias of 20 V_{pp}, 100 kHz is applied, GO aligns with the electric field, and each dot traps nearby particles, which follow the dots as they are slowly moved closer together. **c)** The dots have converged and the particles are now locally aggregated.

5.4.3. In-Situ Thermometry

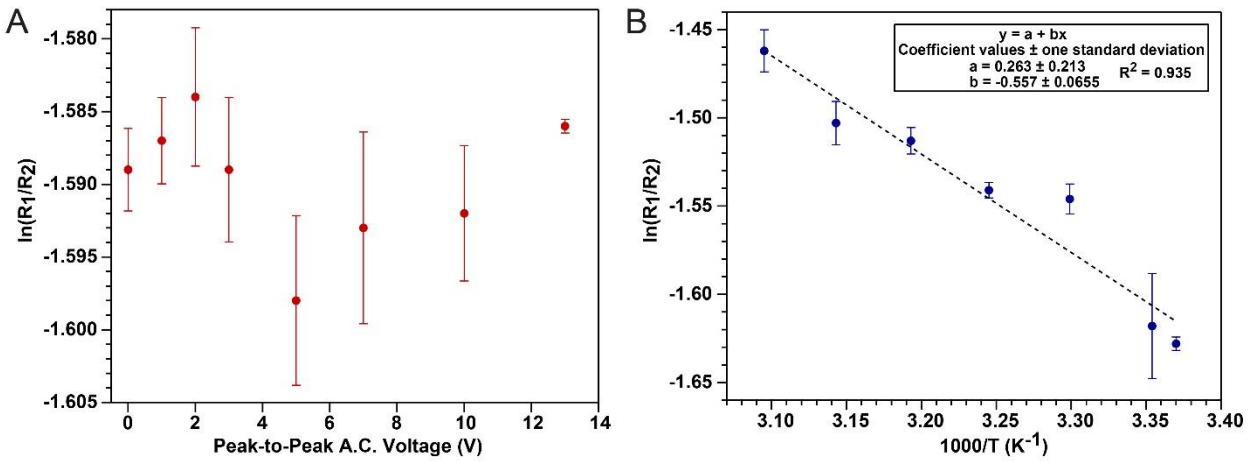

Figure 5.7. Thermometry of GO suspension in OET device with $NaYF_4$:Yb^{3+},Er^{3+} nanocrystals. **a)** Plot of $\boldsymbol{\ln(R_1/R_2)}$ as a function of applied voltage (frequency = 500 kHz). **b)** Calibration data collected with temperature-controlled sample chamber from room temperature (23.6°C)–50°C.

Figure 5.7a shows the plots of $\ln(R_1/R_2)$ from our *in-situ* ratiometric thermometry experiments in the OET device. Unfortunately, the calibration data (Figure 5.7b) was not particularly linear

(R^2 of best-fit line = 0.935), and the ambient temperature as measured with the thermocouple within the chamber (23.6°C) was slightly higher than the air temperature measured with a standalone thermocouple (21.7°C). These factors precluded the extraction of absolute temperatures within a few degrees' accuracy. In addition, the power of the excitation laser was more than a thousand times greater than the laser used for OET manipulation, which could cause significant photothermal heating and explain why the zero-voltage point corresponds to a temperature of ~28°C. Nevertheless, the variations in $\ln(R_1/R_2)$ for the GO/$NaYF_4$:Yb^{3+},Er^{3+} nanowire suspension at different applied voltages are small compared to the variations between successive calibration points. In fact, using the best-fit line for the calibration data, the difference between the maximum and minimum of $\ln(R_1/R_2)$ (-1.594 and -1.581 respectively) over the tested voltages corresponds to a variation in temperature of less than 2.2°C, confirming expectations of negligible Joule heating. It is also worth noting that $\ln(R_1/R_2)$ did not follow a clear trend as voltage was increased, suggesting that the variations may simply stem from measurement uncertainty rather than the applied field. The negligible temperature change not only allows room-temperature values to be used for theoretical force calculations, but also rules out electrothermal convection and buoyancy-driven flow as forces to be considered for the trapped particles, since these originate from temperature gradients in the liquid.

We correlated these experimental results with a finite-element simulation in COMSOL Multiphysics. Based on measurements of the OET device used in our experiments, the trapping medium was modeled as a cylinder 8 mm in diameter and 92 μm thick sandwiched between two 20 × 30 × 0.7 mm rectangular plate electrodes. The conductivity of the medium was set at our measured room-temperature value of 16 μS cm^{-1} for a GO dispersion of 0.1 mg mL^{-1}. To approximate the effect of illumination, the conductivity of the a-Si:H was modeled as a 2D

Gaussian distribution at the center of the liquid region. The maximum conductivity was taken as 0.003 S m^{-1} based on an experimental fit to power densities performed by Valley et al.,[184] with the edge of the illuminated region corresponding to 3 standard deviations from the maximum. The dark conductivity, corresponding to the baseline of the Gaussian, is $2.45 \cdot 10^{-5}$ S m^{-1}.[193] The heat flux due to the incident light at the a-Si:H/liquid boundary was modeled using a 2D Gaussian distribution of the measured laser power (3.49 μW), multiplied by the room-temperature emissivity of a-Si:H (0.8, taking it to be the same as the emissivity of crystalline silicon).[194] A heat transfer coefficient of 10 W m^{-2} K^{-1} and emissivity of 0.9 was assumed for the glass surfaces in contact with air.

The results of the simulation are shown in Figure 5.8 for our maximum experimental bias of 13 V_{pp} at 500 kHz. Even at this bias, the maximum predicted temperature increase of the liquid is only 2.2 K, consistent with the ratiometric measurements.

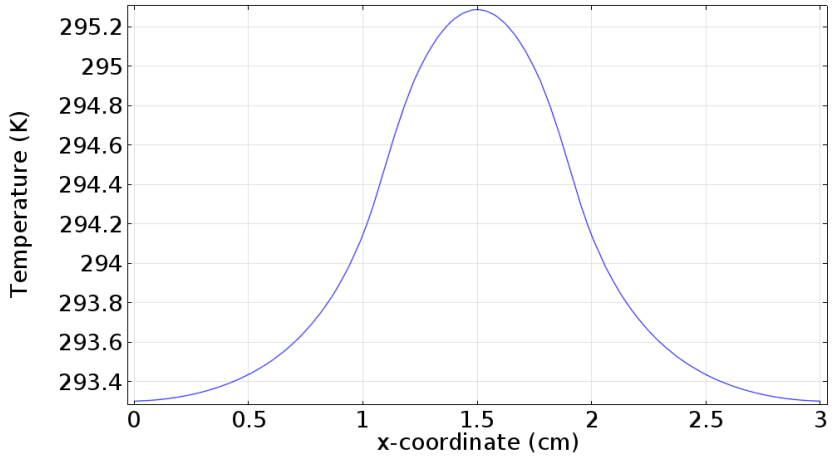

Figure 5.8. Steady-state temperature plot of OET device obtained from finite-element simulations, at level of a-Si:H surface, illuminated with HeNe laser (power 3.49 μW, spot diameter 5.8 μm) at bias of 13 V_{pp}, 500 kHz.

5.5. Conclusion

In conclusion, we have demonstrated that both single and multiple platelets of GO can be trapped, translated, and positioned in suspension using OET. The trapping can be actuated by a low-power helium–neon laser or even a digital projector, the latter allowing for parallel trapping of particles

into complex and dynamic user-defined configurations. In addition, *in situ* thermometry with rare earth-doped fluoride nanoparticles shows that heating is minimal during OET operation. With reasonable approximations, both the DEP force and the hydrodynamic drag force on an arbitrary particle of GO can be calculated from its dimensions and the properties of the OET device and trapping medium. Knowing these forces makes it possible to determine the particle's maximum achievable speed in an OET trap and thereby quantitatively gauge the capabilities of OET for GO. Combined with suitable immobilization and reduction techniques, OET can be a simple, low-cost means to tune the electrical, thermal, optical, and mass transport properties of graphene-based materials derived from GO.

Chapter 6. Copper- and Chloride-Mediated Synthesis and OET Trapping of Palladium Nanowires[5]

6.1. Introduction

Palladium nanocrystals are highly useful for industrial and small-scale research processes alike. Examples include hydrogen sensing and storage based on hydriding phase transformations[195–197]; heterogeneous catalysis for hydrogenation, cross-coupling reactions, electro-oxidation of organic compounds[198–201], and singlet-oxygen generation[202]. Because the performance of Pd in such applications is highly dependent on its size, shape, and exposed facets, much research has been devoted to controlling the geometry of Pd nanocrystals during their synthesis. Additionally, considering palladium's catalytic importance, the ability to manipulate and spatially pattern Pd nanocrystals via OET would be highly valuable, enabling one to tailor the mass transport of reactive species and the distribution of reaction products. While OET has proven useful in the past for patterning and separation of metallic silver nanowires[167], it generally requires nanostructures with high aspect ratios (L/d>100) to generate an appreciable trapping force at reasonable voltages, as we previously saw that the high aspect ratio of GO particles enhanced the Clausius–Mossotti factor (Section 5.2.2). Conventional spherical Pd nanoparticles can be difficult to manipulate with OET because thermal fluctuations typically overcome the DEP force, which scales with the cube of the particle radius.[167] Hence, there is a special interest in producing Pd nanocrystals with elongated morphology. Beyond easier OET manipulation, for hydrogen sensing and storage, Pd nanowires would have the benefit of shorter diffusion lengths for hydrogen due to their short radial dimension, allowing for shorter response times.

[5] This chapter is based on "Copper- and chloride-mediated synthesis and optoelectronic trapping of ultra-high aspect ratio palladium nanowires", published in *Journal of Materials Chemistry A* **6**, 5644-5651 (2018) by Matthew B. Lim, Jennifer L. Hanson, Leron Vandsburger, Paden B. Roder, Xuezhe Zhou, Bennett E. Smith, Fumio S. Ohuchi, and Peter J. Pauzauskie.

To date, several methods have been reported for the preparation of one-dimensional Pd nano-rods and wires, such as chemical vapor transport[203], electrodeposition[204,205], electron beam lithography[206], and solution-phase reduction of palladium-containing salts[207–209]. While solution-based processes offer the most promise for large-scale production, it is challenging to preferentially obtain 1D nanostructures in this manner because of palladium's face-centered cubic (FCC) structure, which provides no driving force for anisotropic growth. Polyols such as ethylene glycol are commonly used as solvents for solution-phase preparation of noble metal nanocrystals with well-defined morphologies, due to their ability to dissolve the precursor metal salts and temperature-dependent reducing power. However, product geometries are typically restricted to cuboctahedra or truncated cubes because of the rapid reduction and growth rates in polyols.[210]

In 2009, Huang and Zheng reported a simple hydrothermal synthesis of large yields of high aspect ratio palladium nanowires (PdNWs) using $PdCl_2$ as the metal precursor and polyvinylpyrrolidone (PVP) as both the palladium reductant and nanowire surface stabilizer[208]. They also noted the importance of NaI in promoting nanowire growth, which has since been attributed to the role of iodide as a selective capping agent for the lateral {100} facets of nanowires.[211,212] By carefully tuning the reaction time and reagent concentrations, particles with lengths up to 3 μm and diameter around 9 nm were produced. Structurally, the nanowires have a cross-section consisting of five {111} twin planes radiating from the central <110> axis and are bounded by {100} surfaces on the sides (Figure 6.2h). Unfortunately, this method as-written has not been reproducible in the present authors' hands, resulting mainly in low-aspect ratio palladium nanoparticles.

Trace impurities are known to significantly affect the solution-phase growth of metallic nanocrystals. Parts per million-level chloride impurities in the polyol synthesis of silver

nanocrystals were found to inhibit the growth of irregular, twinned nanoparticles in favor of single-crystal cubes and tetrahedra.[213] Also, iodide impurities in cetyltrimethylammonium bromide (CTAB) surfactants have been shown to prevent the surfactant mediated synthesis of gold nanowires.[214] On the other hand, more recently, Tang et al. noted that the addition of trace Ag(I) or Cu(II) enhanced the yield of pentagonally twinned Pd nanorods grown in water at atmospheric pressure from $PdCl_2$, using CTAB and iodide as capping agents and ascorbic acid as the reductant.[209] While these nanorods were inferior in aspect ratio to those produced hydrothermally by Huang and Zheng, being only 100–500 nm long by 20 nm wide, the results suggest that the presence of other transition metal ions is key to producing 1D Pd nanostructures in large quantities, an idea that had not been introduced previously.

In this chapter, we demonstrate a reproducible, high-yield route to palladium nanorods and nanowires based on the aforementioned hydrothermal method, and their utility for OET patterning. Furthermore, we show that the high yield of these 1D nanostructures is mediated by the introduction of trace Cu(II)—via soluble copper(II) acetate or copper(II) sulfate—and/or sodium chloride to the precursor solution. Nanowires produced by this approach feature a greater length and aspect ratio (up to 7 μm and 350 respectively) than any previously reported Pd nanocrystals produced by solution-phase, non-templated methods.

6.2. Materials and Methods

6.2.1. Synthesis

Palladium(II) chloride (99.999%), sodium iodide (≥99%), polyvinylpyrrolidone (PVP, MW=29000 or 55000), copper(II) acetate monohydrate ($Cu(OAc)_2*H_2O$, ≥98%), and sodium chloride (≥98%) were purchased from Sigma-Aldrich Corporation, USA. Copper(II) sulfate pentahydrate (≥98%) was purchased from Avantor Performance Materials, USA. Nanopure

deionized water (18.2 MΩ·cm, ThermoScientific Barnstead filtration system) was used in all experiments. All reagents were used as received without additional purification.

In a typical synthesis with the Cu(II) additive alone, 17.7 mg of $PdCl_2$, 300 mg of NaI, and 800 mg of PVP (MW 29000) were added to an Erlenmeyer flask with 11 mL of nanopure water. For control experiments without Cu, 12 mL of water was used. The mixture of reagents was sonicated until the NaI and PVP dissolved completely. Due to the poor solubility of $PdCl_2$ in water, the mixture was then stirred at 50°C for 10 h, and cooled back to room temperature.

For syntheses involving NaCl, 46.8 mg of NaCl was added alongside $PdCl_2$, NaI, PVP, and water in the same amounts as above, giving a NaCl:$PdCl_2$ molar ratio of 8:1. Additionally, MW 55000 PVP was substituted for MW 29000 PVP. In this case, the reagents were only stirred for 3 h at room temperature following sonication, owing to the enhanced solubility of $PdCl_2$ imparted by NaCl.

To introduce Cu(II), 1 mL of 8 μM aqueous solution prepared from $Cu(OAc)_2 \cdot H_2O$ or $CuSO_4 \cdot 5H_2O$ powder was then added dropwise to the mixture under stirring, giving 0.67 μM Cu(II) overall, or a Cu:Pd molar ratio of ~1:12500. The final precursor solution was then sealed within a 23-mL Teflon-lined steel autoclave (Parr, model #4749). To guard against contamination from other trace metals and organics, the Teflon liner was treated for 24 hours beforehand with aqua regia, prepared from a 1:3 (mol/mol) mixture of concentrated nitric and hydrochloric acids; after this time, the acid was neutralized with sodium bicarbonate and the liner was rinsed repeatedly with water. The sealed autoclave was placed in a preheated oven at 200°C for 6 h (for syntheses with Cu(II) alone) or 2 h (for syntheses with Cu(II)+NaCl or NaCl alone), after which it was removed and cooled to room temperature in ambient air. The recovered solution was diluted with isopropyl alcohol, and then repeatedly rinsed and centrifuged at 5000 rpm to precipitate the

Pd particles. Samples were finally rinsed and suspended in ethanol or water before subsequent characterization. High-aspect-ratio nanowire suspensions were observed to have a dynamic opalescent texture when inverted.

6.2.2. Characterization

SEM images were obtained on a FEI Sirion XL30 with 10 kV accelerating voltage. TEM images with accompanying SAED and EDS were obtained on a FEI Tecnai G2 F20 with 200 kV accelerating voltage.

XRD was performed on a Bruker D8 Discover with General Area Detector Diffraction System (GADDS) with a Cu K_α radiation source at 1.54 Å and 2θ step size 0.05°. The sample consisted of a (111) silicon wafer onto which an aqueous PdNW suspension was evaporated, and was aligned in the system using the laser guidance system provided in the instrument.

XPS was conducted using a PHI 5000 VersaProbe setup with Al K_α radiation. Samples were deposited on a Si wafer, treated with oxygen plasma prior to analysis to etch away the existing PVP surface coating, and aligned in the system using the laser guidance system provided in the instrument. Acquired spectra were deconvoluted and analyzed with PHI MultiPak software (Physical Electronics, Inc.). The energy calibrations were made against the C1s peak (284.8 eV) of adventitious carbon as a reference. For core-level analysis of Pd, an asymmetric peak shape (Doniach-Sunjic) was used for each of the Pd subpeaks, while the oxide subpeaks were fitted with a Gaussian lineshape. FWHM values were limited to 1–1.5 eV for all peaks excepting the $Pd3p_{3/2}$, which is given a broader FWHM, as shown by Gabasch et al.[215]

Zeta potentials of the Pd particles were obtained on a Malvern Instruments Zetasizer Nano ZS. The particles were dispersed dilutely in nanopure water and the zeta potential was taken as the average of 5 measurements.

6.2.3. OET Manipulation

For OET studies of our hydrothermal PdNWs, the samples made with NaCl alone were used because they contained the highest-aspect-ratio particles, which would experience the largest trapping forces. The OET setup was identical to that used for single-particle GO manipulation (Section 5.3.1).

6.3. Calculation of the Clausius–Mossotti Factor for a Pd Nanowire

To confirm the trappability of our PdNWs in OET from a theoretical perspective, we employ a method similar to GO to determine the CM factor, taking surface charge effects into account (see Section 5.2), but modeling the nanowire as a long cylinder or highly prolate spheroid. As with GO, the PdNW will align its long axis parallel to the electric field during OET operation, due to the polarizability along the long axis being much greater than along its short axis.[216] The expression for the CM factor is identical to the oblate spheroid case, i.e. $f_{CM}^{*} = \left(\varepsilon_p^{*} - \varepsilon_m^{*}\right)/\left(C\varepsilon_p^{*} + D\varepsilon_m^{*}\right)$ with $C = 3L_a$ and $D = 3(1 - L_a)$, but the depolarization factor L_a is different. For a prolate spheroid with semi-major axis *a* and semi-minor axis *b*, the depolarization factor along the major axis is:[217]

$$\boldsymbol{L_a = \frac{b^2}{2a^2e^3}\left[\ln\left(\frac{1+e}{1-e}\right) - 2e\right]} \qquad \textbf{(6.1)}$$

where the eccentricity $e = \sqrt{1 - b^2/a^2}$.

O'Konski showed that the effective conductivity of a cylinder with half-length *a* and radius *b*, assuming a homogeneous internal electric field, can be expressed along the two directions as:[178]

$$\boldsymbol{K_{eff,a} = K_B + \frac{2K_S}{b}} \text{ and } \boldsymbol{K_{eff,b} = K_B + \frac{K_S}{b}} \qquad \textbf{(6.2)}$$

where K_B is the bulk conductivity of the particle and K_S is the surface conductance. In our case, it is misleading to use the conductivity of bulk Pd (~$9.1 \cdot 10^6$ S m^{-1}) for K_B, as the conductivity of

nanowires can be significantly lower due to grain boundary reflections and surface scattering of charge carriers.[218,219] Instead, we use the results of Bhuvana and Kulkarni,[220] who measured a resistivity of 0.300 μΩ m (conductivity = $3.33 \cdot 10^6$ S m^{-1}) for PdNWs with a 30 x 60 nm cross-section and μm-scale length, similar to our PdNWs. This value is still high enough, given the metallic nature of Pd, that we would expect the surface conductivity of a PdNW in deionized water to be negligible in comparison. However, to verify this claim, as with GO, we can assume that the counterion is H^+ and calculate the surface conductivity using the Grahame equation (Equation 5.8) with the measured pH and zeta potential of a PdNW dispersion. For a dilute aqueous dispersion of the highest aspect ratio nanowires (made with NaCl and MW 55000 PVP), at a similar concentration to that used for OET manipulations, the measured pH was 6.33 and the zeta potential was -31.2 mV (Table 6.1). The pH gives a bulk H^+ concentration of $4.68 \cdot 10^{-7}$ M, or $2.82 \cdot 10^{20}$ m^{-3}. Solving the Grahame equation at T = 20°C gives surface charge density $\sigma_S = 5.29 \cdot 10^{-5}$ C m^{-2}, which in turn gives surface conductance $K_S = 1.91 \cdot 10^{-11}$ S. Thus, for typical PdNW radii in the tens of nanometers, the surface charge contribution to the effective conductivity is on the order of 10^{-3} S m^{-1}, which is indeed far lower than the bulk conductivity of the nanowire.

Besides the conductivity, the relative permittivity of a PdNW must also be known to determine its CM factor. This can be calculated from the Drude model of metallic conduction, which is based on the classical kinetic theory of gases and treats the system as a sea of non-interacting electrons constantly bouncing off of heavier, immobile positive ions. According to this model, the real part of the dielectric function, ε_1, for a given angular frequency ω is:[221]

$$\boldsymbol{\varepsilon_1 = \varepsilon_c - \frac{\omega_p^2}{\omega^2 + 1/\tau^2}} \qquad \textbf{(6.3)}$$

where ε_c is the limiting high-frequency value of the dielectric function, ω_p is the plasma frequency, and τ is the relaxation time. For practical purposes, ε_c can be taken as 1, given that at the high-

frequency limit, no mechanical system can react quickly enough to the electric field. ω_p represents a plasma oscillation resonance and is the frequency at which $\varepsilon_1 = 0$, and below which ε_1 is negative; in other words, an incident field with frequency below ε_1 cannot penetrate the sample and will be totally reflected. For Pd, $\hbar\omega_p$ has previously been reported as 9.72 eV, corresponding to $\omega_p = 1.48 \cdot 10^{16}$ s^{-1}.[222] τ represents the time required to relax the velocity of an electron in the material to 1/*e* of its initial value and can be found from the following relation:[221]

$$\boldsymbol{\tau = 4\pi\, \sigma_{dc}/\omega_p^2} \qquad \textbf{(6.4)}$$

where σ_{dc} is the DC conductivity of the material (i.e., at $\omega = 0$), for which we can use the aforementioned PdNW conductivity of $3.33 \cdot 10^6$ S m^{-1}, giving $\tau = 1.72 \cdot 10^{-15}$ s. Finally, substituting τ along with the plasma frequency into Equation 6.3, and letting ω be the OET bias frequency of 500 kHz ($3.14 \cdot 10^6$ s^{-1} in angular form), we get $\boldsymbol{\varepsilon_1 \approx -647}$.

The other necessary parameters to determine the CM factor were obtained in the same way as with GO. The electrical conductivity of the PdNW dispersion (σ_m) was measured directly as 14 μS cm^{-1}. The real permittivity of water (80.1) was taken from the literature.[180] Room temperature was assumed for all parameters.

As shown in Figure 6.1, for typical dimensions of our highly elongated PdNWs, $Re[f^*_{CM}]$ is 10^3–10^4. In contrast, nanorods with diameter 20 nm and length 500 nm, similar to those reported by Tang et al.,[209] $Re[f^*_{CM}]$ is less than 100, using the same prolate spheroid model described above. This illustrates the dramatic impact of aspect ratio on OET trapping.

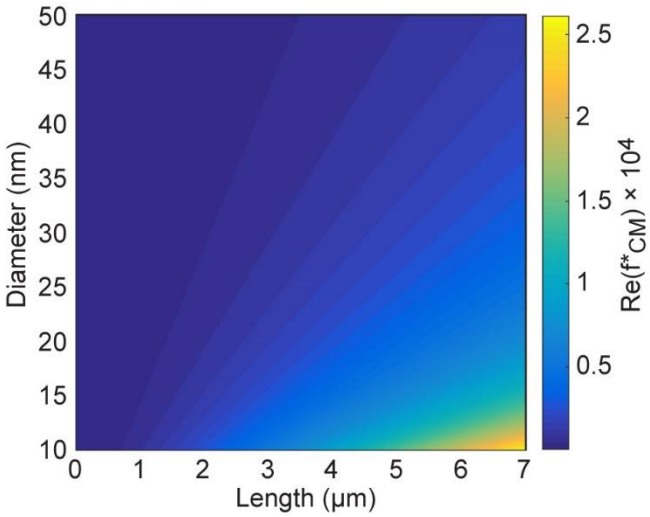

Figure 6.1. Calculated values of the real Clausius–Mossotti factor ($Re(f^*_{CM})$) of a Pd nanowire in water at 500 kHz for a range of particle lengths and diameters.

6.4. Results and Discussion

6.4.1. Synthetic Studies

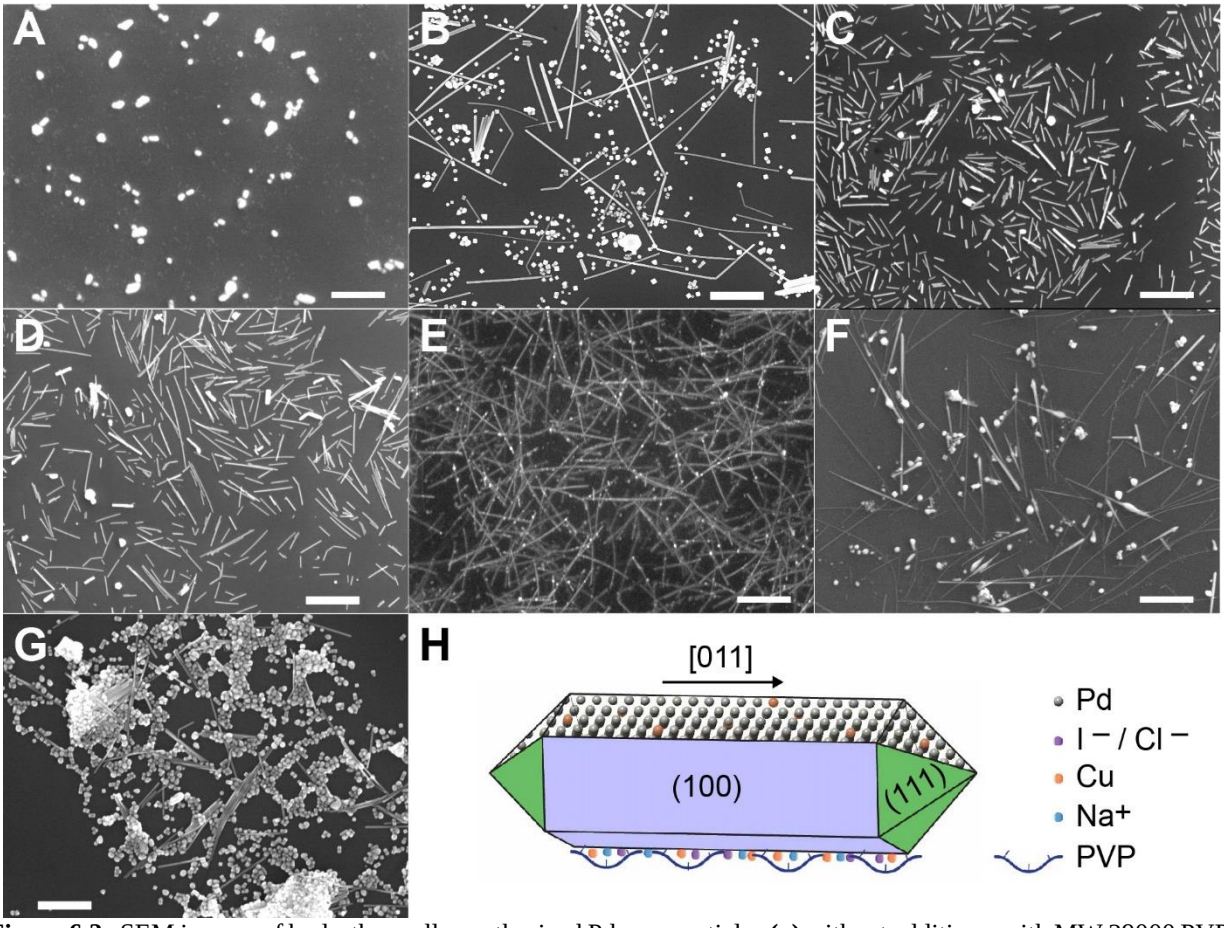

Figure 6.2. SEM images of hydrothermally synthesized Pd nanoparticles **(a)** without additives, with MW 29000 PVP, for 2 h; **(b)** without additives, with MW 29000 PVP, for 6 h; **(c)** with $Cu(OAc)_2$ and MW 29000 PVP for 6 h; **(d)** with CuSO4 and MW 29000 PVP for 6 h; **(e)** with NaCl, $Cu(OAc)_2$, and MW 55000 PVP for 2 h; **(f)** with only NaCl and MW 55000 PVP for 2 h; **(g)** with Cu(OAc)2, NaCl, and MW 29000 PVP for 2 h. Scale bar = 1 μm (a–f); 500 nm (g). **(h)** Schematic of ideal PdNW with penta-twinned cross-section, <011> growth direction, and surface coating.

Table 6.1. Summary of hydrothermally synthesized 1D Pd nanostructures. Particle dimensions were measured from SEM images with sample size = 50 particles.

Additive	MW of PVP	Dwell Time @ 200°C	Average Length of 1D Structures ± SD [μm]	Yield of 1D Structures	Zeta Potential (mV)
None	29000	2 h	N/A	N/A	–40.5
None	29000	6 h	1.24 ± 0.919	~10%	–18.7
$Cu(OAc)_2$	29000	6 h	0.390 ± 0.233	~90%	–21.1
$CuSO_4$	29000	6 h	0.491 ± 0.325	~90%	–14.9
NaCl + $Cu(OAc)_2$	55000	2 h	0.935 ± 0.412	~75%	–35.3
NaCl	55000	2 h	1.83 ± 1.45	~50%	–31.2

As illustrated in Figure 6.2a, an exact reproduction of Huang and Zheng's synthesis,[208] with $PdCl_2$, NaI, and MW 29000 PVP in water, no prolonged incubation prior to hydrothermal treatment, and a 2 h dwell time at 200°C, only produced round blob-like particles 50–300 nm in diameter. It is worth noting that because $PdCl_2$ is poorly soluble in water, we had to add an overnight heated stirring step to dissolve it appreciably; even then, it did not always dissolve completely. Additionally, we had to increase the hydrothermal dwell time to 6 h to obtain an appreciable amount of 1D particles in the product (Figure 6.2b), but their yield was only ~10%.

In contrast, adding 0.67 μM $Cu(OAc)_2$ or $CuSO_4$ to the precursor solution while maintaining the dwell time at 6 h dramatically increased the yield of 1D particles to ~90% (Figure 6.2c, d). However, they are much shorter than those made without additives (Table 6.1). Both of these observations are consistent with the aforementioned report of Tang et al.,[209] who used a similarly small concentration of Cu(II) (19 μM) via $CuSO_4$. They hypothesized that Cu(II) was reduced to Cu nanoparticles, which tend to form twinned structures and could therefore serve as a template for twinned Pd nanorods. While this is a plausible explanation for their system, given the ability of ascorbic acid to reduce Cu(II) in addition to Pd(II) at elevated temperature, it is unlikely for our system due to the weaker reducing power of PVP. In fact, Gasparotto et al. found that PVP adsorbed on crystalline Pt electrodes does not begin to be oxidized until ~0.4 V vs. RHE, which is higher than the standard reduction potential of Cu (+0.34 V, $Cu^{2+} + 2e^- = Cu$), implying that PVP cannot spontaneously reduce Cu(II) ions.[223]

Rather, we believe that Cu protects twinned Pd nuclei by acting as a sacrificial target for oxidation by O_2 (from ambient air) dissolved within the precursor solution. Left unchecked, the dissolved O_2 works in tandem with halide ions, particularly Cl^-, to re-oxidize the nascent metallic

Pd crystals back to soluble metal–halide complexes. Since high-energy crystal facets and defect zones are especially susceptible to this oxidative etching, the formation and growth of pentagonally twinned Pd seeds into nanowires will be greatly suppressed, as has been experimentally verified for polyol synthesis of Pd nanostructures from Na_2PdCl_4.[224] Although our introduction of $Cu(OAc)_2$ may seem counterintuitive as +2 is generally the highest oxidation state of Cu, and PVP is unlikely to reduce Cu(II) as previously stated, we speculate instead that the excess iodide in the system reduces Cu^{2+} to CuI, which can then be oxidized back to CuO by the dissolved oxygen.[225] Incidentally, for the synthesis of Ag nanowires in ethylene glycol, which also reduces Cu *in situ*, it has been shown that Cu(I) and Cu(II) salts have near-identical effectiveness in scavenging oxygen and promoting nanowire growth.[226] While Huang and Zheng's report on hydrothermal PdNW synthesis[208] does not mention the addition of Cu species, it is possible that the deionized water used by the authors contained trace Cu from the corrosion of copper pipes, thereby promoting the growth of nanowires.

Our nuclei protection hypothesis is not only corroborated by the higher yield of 1D Pd nanostructures with Cu(II), but also by their shorter average length compared to those obtained without additives. The Cu(II) species enable a higher concentration of Pd nuclei to form, particularly the penta-twinned seeds for rods and wires, which in turn restricts the extent of diffusional growth.

We also sought to address the problem of inconsistent and incomplete dissolution of $PdCl_2$ in the precursor mixture. This would have an unpredictable effect on reagent ratios, particularly the ratio of PVP to Pd precursor, which is known to heavily affect the product morphology.[208,227] We therefore introduced NaCl, which enables formation of the complex $PdCl_4^{2-}$ anion that lowers the energy of interaction with water molecules so more palladium can be solvated.[228] Indeed,

when NaCl was added in an 8:1 molar ratio relative to $PdCl_2$, no residual solid was observed in the precursor mixture following sonication and 3 h of room-temperature stirring. This eliminated the need for prolonged, heated mixing prior to hydrothermal treatment. Another advantage of NaCl is that $PdCl_4^{2-}$ has a lower redox potential than Pd^{2+} alone (+0.59 V versus +0.95 V), offering a slower reduction pathway that would limit the number of nuclei and favor diffusional growth. Again in line with expectations, NaCl gave high yields of PdNWs, significantly longer than those obtained with Cu(II) alone, with only 2 h of heating at 200°C rather than 6 h (Figure 6.2e, Table 6.1). The time savings and high aspect ratio of the PdNWs from this processes hold great promise for large-scale manufacture and OET applications.

Two surprising observations were noted with the NaCl-mediated approach, which we believe are related. The first is that we had to use larger PVP (MW 55000) to attain a high yield of nanowires; using MW 29000 PVP gave a mixture of nanowires and nanoparticles in similar proportions to the sample made without any additives (Figure 6.2g). Second, even when Cu(II) species were omitted altogether, good yields of long nanowires were obtained (Figure 6.2f, Table 6.1), considerably better than the yield from the 6 h syntheses with no additives. This is surprising considering the excess of Cl^- in the system with NaCl, which would conceivably exacerbate oxidative etching of twinned seeds in the absence of any scavenger. A similar phenomenon has been reported for the aqueous, ascorbic acid-mediated synthesis of Pd nanoparticles with a large excess of Cl^-, where increasing the Cl^- concentration increased the size and fraction of pentagonal nanorods in the product.[229] The proposed explanation is that the extra Cl^- lowers the reduction rate by hindering contact between the Pd precursor and reducing agent, and also lowers the etch rate by obstructing O_2 from the Pd seeds. Going back to the first observation, it has also been shown that in the reduction of Na_2PdCl_4 by PVP, the conversion percentage to Pd decreases with

increasing molecular weight of PVP.[227] Thus, we believe that the slower reduction in this system has a stronger effect on the product than oxidative etching. Nevertheless, it is worth noting that the nanowire yield is even better with the co-addition of $Cu(OAc)_2$ (75% vs. 50%), suggesting that oxidative etching still plays a minor role. Also, the nanowires produced with the co-addition of $Cu(OAc)_2$ are shorter on average than those produced with NaCl alone, again consistent with our hypothesis that Cu protects twinned seeds.

Subsequent characterizations of our PdNWs in this report focus on the samples synthesized with $Cu(OAc)_2$ alone.

6.4.2. Characterization of Cu-Mediated PdNWs

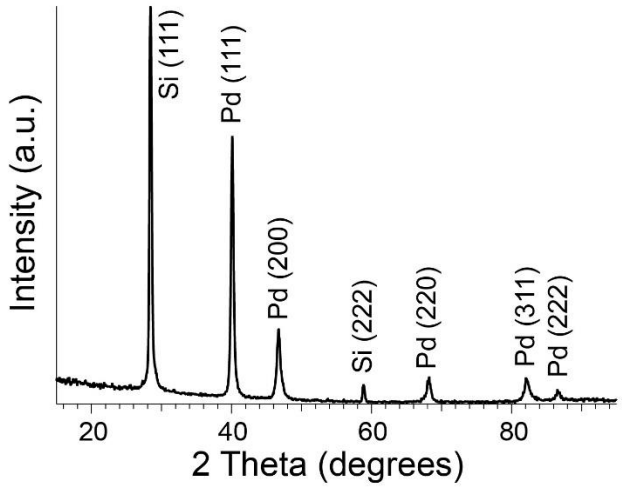

Figure 6.3. Cu Kα XRD pattern of PdNWs synthesized with $Cu(OAc)_2$ and MW 29000 PVP for 6 h. Si (111) peak is from the silicon wafer on which the nanowires were deposited.

XRD confirmed the crystallinity of the PdNWs (Figure 6.3), with the diffraction peaks at 2θ = 40.1°, 46.7°, 68.1°, 82.1°, and 86.6° originating from the (111), (200), (220), (113), and (222) planes of FCC Pd respectively (JCPDS card #05-0681). According to the JCPDS card, the respective intensity values of these peaks, normalized to that of the (111) peak, are 1:0.42:0.25:0.24:0.08, while our experimental intensities follow the ratio 1:0.23:0.076:0.078:0.045 which is consistent with the nanowires' high aspect ratio. In particular, the intensity ratio between

the (111) and (200) peaks is 83% higher, and the intensity ratio between the (200) and (220) peaks is 80% higher, compared to the JCPDS card. This indicates that the PdNWs are mainly bounded by {111} and {100} facets, as expected from the pentagonal wire geometry (Figure 6.2h). In addition to the Pd diffraction peaks, the sharp peaks at $2\theta = 28.4°$ and 58.9° come from the (111) and (222) planes, respectively, of the (111)-oriented silicon wafer on which the PdNWs were deposited. (Although (222) is theoretically a basis-forbidden reflection for Si, it has been observed experimentally due to the phenomenon of multiple diffraction which can make a forbidden reflection visible depending on the sample's in-plane orientation.[230])

Bright-field TEM provided evidence of the pentagonally twinned nature of the PdNWs (Figure 6.4). At high magnification of a single nanowire, lattice fringes are visible with a distinctive Moiré pattern and FFT in one particular area (Figure 6.4b–d), which can be interpreted in the context of a chain-like structure of five twinned tetrahedral crystals bound by {111} facets and arranged about the <011> axis. Specifically, these features arise from the overlapping of the [100] and [112] zone axes when the electron beam is oriented perpendicular to one of the <011> lateral edges and its opposing {100} face. In support of this claim, a well-defined dark line appears along the middle of nanowire in Figure 6.4b, corresponding to the aforementioned lateral edge. Additionally, the strong and complex contrasts observed on individual nanowires at both high and low magnification suggest numerous internal strains and defects, which are expected due to the intrinsic 7.4° angular gap of a theoretical structure of five twinned {111} tetrahedra in the FCC system. Similar FFT and contrast features have been reported for pentagonally twinned nanowires and nanorods of silver, another FCC metal.[231–233]

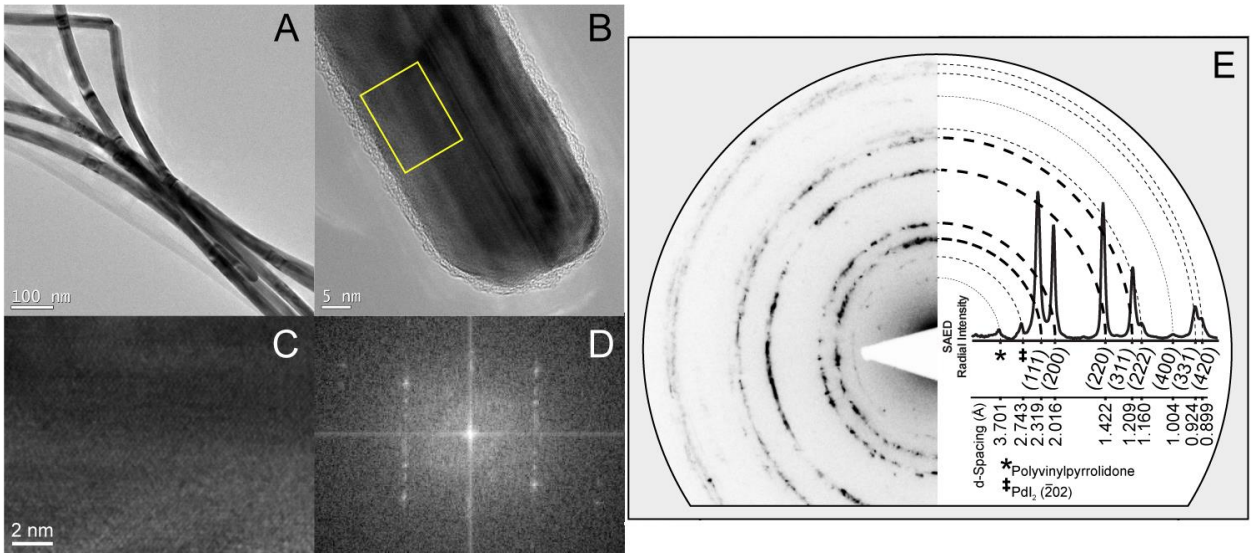

Figure 6.4. Bright field TEM images of **(a)** an aggregate of PdNWs; **(b)** a single PdNW. **(c)** Enlarged and rotated image of area outlined in (b), showing lattice fringes and moiré pattern. **(d)** FFT of (c). **(e)** Background-subtracted SAED pattern (left) with integrated intensities (right) of a cluster of PdNWs.

SAED of a cluster of nanowires agreed with XRD and bright-field TEM on the FCC nature of the nanowires, but showed additional peaks at 2.72 and 3.67 Å d-spacing (Figure 6.4e). The first of these peaks matches the d-spacing of the $(\bar{2}02)$ planes of PdI_2, a phase that could form from surface iodide remnants.[234] The peak at 3.67 Å likely originates from the PVP polymer surface coating owing to its broad shape, the sharply increasing background signal (subtracted out in Figure 6.4e) for d-spacings > 2.5 Å ($2\theta < 36°$), and the presence of a peak around a similar d-spacing in previous XRD studies of PVP.[235–237] Consistent with this hypothesis, a thin (~1 nm) amorphous layer is observed to surround the nanowire in Figure 6.4b. Given that both PVP and PdI_2 would only be present at the nanowire surfaces, they would not appear in the XRD pattern due to the μm-scale penetration depth of X-rays versus the nm-scale penetration depth of electrons. Furthermore, the presence of iodide on the surface is consistent with the negative zeta potential measurements on all of our samples (Table 6.1), considering that PVP is a neutral polymer.[238]

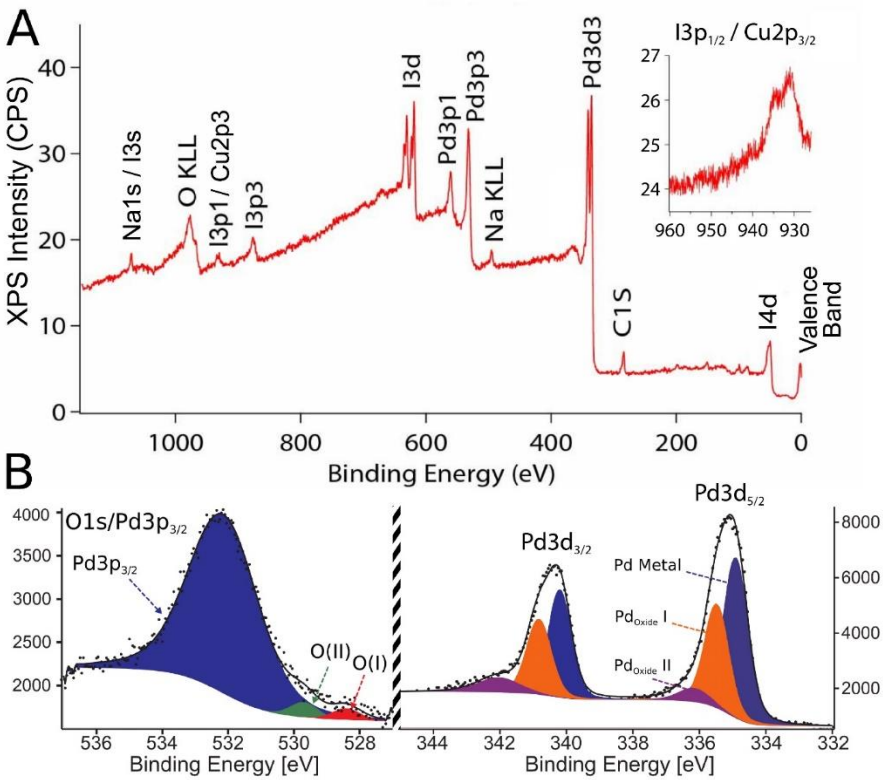

Figure 6.5. (a) XPS survey spectrum of oxygen plasma-treated PdNW dispersion on Si substrate. $I3p_{1/2}$ binding energy at 932 eV overlaps with potential $Cu2p_{3/2}$ peak (inset). **(b)** High-resolution XPS spectrum of Pd3p (left) and Pd3d (right) regions with deconvoluted peaks.

XPS was performed to provide chemical information for the nanowires' surface composition (Figure 6.5). PdNW samples were treated with oxygen plasma to expose the metallic surface, removing the PVP polymer coating. Carbon (C1s 284 eV), sodium (Na1s 1070.5 eV), iodine ($I3p_{3/2}$ 876 eV), and palladium ($Pd3d_{5/2}$ 335, $Pd3d_{3/2}$ 340, $Pd3p_{3/2}$ 532.5, $Pd3p_{1/2}$ 561 eV) peaks are present in the spectra. Partial oxidation of the iodine can be seen through double peaks for $I3d_{5/2}$ (619, 623 eV) and $I3d_{3/2}$ (630.5, 635 eV).

The presence of metallic Cu is difficult to ascertain from XPS, as the potential $Cu2p_{3/2}$ peak (expected 932 eV)[239] overlaps directly with the iodine $I3p_{1/2}$ line (Figure 6.5a, inset). The shoulder at 935 eV and tail toward higher binding energy does suggest the presence of CuO, though it cannot be determined whether it was part of the nanowire as-formed, or simply developed upon exposure to air. Complementary neutron activation analysis (NAA) data confirms the presence of

Cu in the nanowires at a concentration of ~62 ppm. Additionally, energy-dispersive X-ray spectroscopy (EDS) mapping of a PdNW in the TEM showed Cu throughout the wire with potential enrichment along its edge, whereas no Cu was detected in a background EDS spectrum of the bare SiO_2 support film of the TEM grid.

High resolution analysis of the Pd3d and Pd3p peaks (Figure 6.5b) suggests that the Pd present in the XPS-analyzed wires is metallic with a Pd_5O_4 monolayer film. The deconvoluted spectrum for $Pd3p_{3/2}$ was fitted to have one metal and two oxidized peak contributions, arising from the overlap of the Pd and O1s peaks. The Pd^0 peak is the largest component of the XPS signal at this energy, indicating a thin oxide film. In addition, the area ratio of the O(I) and O(II) component peaks is approximately unity (1.1–1.3). This is in line with the Pd_5O_4 surface 2D oxide phase, which has been previously reported for annealing of Pd (111) at intermediate temperatures (< 800 K).[215,240,241] The Pd3d signal is also consistent with the presence of Pd_5O_4, as the $3d_{5/2}$ and $3d_{3/2}$ peaks, offset by approximately 5.5–6 eV, can each be deconvoluted into a metal and two oxide subpeaks, following the reasoning that the Pd has two oxidation states in the film. The subpeak positions for the $3d_{5/2}$ level in particular agree with the analysis of Lundgren et al. for Pd_5O_4, the metallic Pd^0 peak being at 334.9 eV, and subsequent oxide peaks placed at 335.5 eV, and 336.2 eV.[241] For $Pd3d_{3/2}$, the Pd^0 peak is at 340.2 eV, with oxide peaks at 340.8 eV and 342.0 eV. As a side note, the energies of the fitted metallic peaks in our Pd3d spectra match those of pure bulk Pd, ruling out the presence of bimetallic PdCu species, which exhibit a slightly higher Pd3d binding energy than pure Pd due to the transfer of valence electrons from Pd to Cu.[242]

We emphasize that the presence of the palladium oxide is attributed to the oxygen plasma treatment prior to XPS, rather than to oxidation during synthesis, considering that Pd films do not oxidize spontaneously in ambient conditions.[243,244] Additionally, while to our knowledge no

studies have been performed on the oxidation of polycrystalline Pd in oxygen plasma, Pd (100) surfaces have been shown to oxidize gradually to bulk PdO under oxygen plasma treatment, with accompanying broadening of the $Pd3p_{3/2}$ and $Pd3d_{5/2}$ peaks similar to our samples.[245] Furthermore, the necessity for an oxygen scavenger to grow nanowires, as demonstrated by our studies with Cu(II), speaks against the presence of a native oxide layer prior to plasma treatment.

6.4.3. OET Manipulation of Pd Nanowires

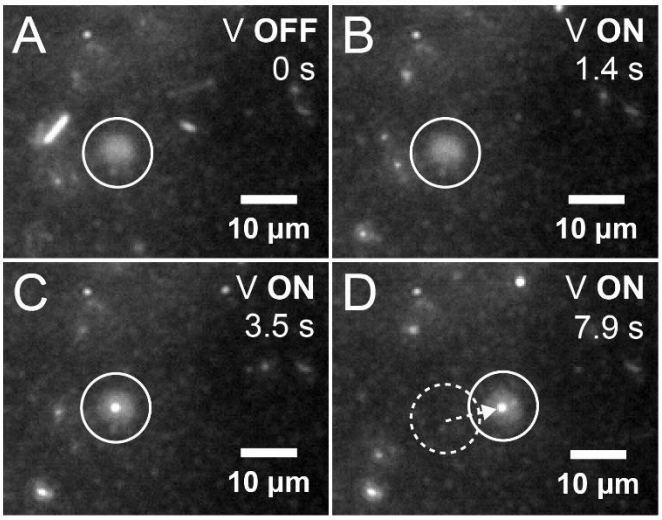

Figure 6.6. Trapping and translation of a single PdNW in water with OET. Arrows indicate the location of the nanowire, and the circular outline indicates the location of the laser spot used as the trap. **a)** No applied bias, nanowire is in Brownian motion. **b)** Voltage (5 V_{pp}, 500 kHz) is turned on, axis of the nanowire aligns with the electric field, and it moves toward the trap. **c)** The nanowire has fallen into the trap. **d)** The nanowire follows the position of the trap as the trap is moved right.

As visual evidence that our PdNWs can be easily trapped, Figure 6.6 depicts an OET experiment with a single PdNW in water, where the a-Si:H was actuated by a helium–neon laser with wavelength 633 nm and a low optical power density of ~13 W cm^{-2}. The nanowire, approximately 6 µm long, is initially in Brownian motion. Upon applying an AC bias of 5 V peak-to-peak (V_{pp}) and 500 kHz, the nanowire experiences a torque that aligns its long axis parallel to the electric field (i.e., vertically within the device), causing it to appear as a dot in the microscope

image. Within ~2 s, the nanowire falls into the nearby illuminated spot, and follows the light as it is moved.

Considering that only low-intensity light (~10 W cm^{-2}) is needed to generate significant electric field gradients, we also demonstrate that our suspended PdNWs can be trapped in bulk with an image emitted from an inexpensive digital projector (Figure 6.7). This offers tremendous advantages over traditional dielectrophoretic nanowire patterning with fixed lithographically defined electrodes,[246] making it possible to form user-defined, dynamically reconfigurable arrays of nanowires using simple presentation software. Such capabilities would be particularly important for Pd considering its widespread use as a catalyst. Conceivably, reaction rates and selectivity could be optimized by controlling the arrangement of catalyst particles. Additionally, the bulk vertical alignment of PdNWs achieved with OET would create facile diffusion pathways for reagent and product species. Finally, the large-scale, solution-phase approach of OET lends itself nicely for creating Pd–carbon nanocomposites via *in situ* gelation of RF. This would allow the patterning and texturing of the PdNWs to be preserved for ex-situ uses, and provide them with a robust, conductive support.

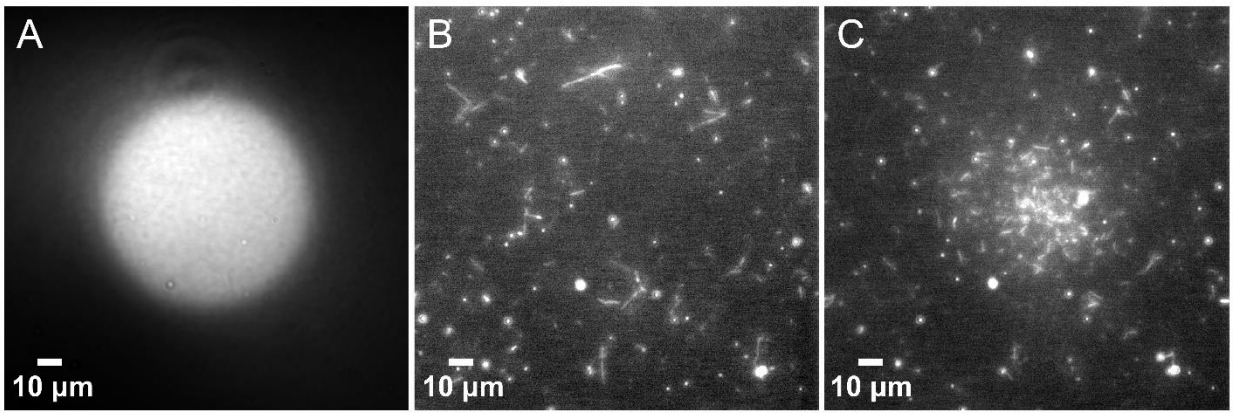

Figure 6.7. Aggregation of PdNWs in water with OET. **(a)** An illuminated circle ~86 µm in diameter is projected onto the OET device using an ordinary digital projector. **(b)** PdNW suspension before illumination and application of bias. **(c)** PdNW suspension after illumination and application of 20 V_{pp}, 500 kHz bias for 5 min (bias off and projected image removed).

6.5. Conclusion

In conclusion, palladium nanorods and nanowires have been synthesized hydrothermally by reduction of $PdCl_2$ with PVP in the presence of iodide and controlled amounts of Cu(II) salts and/or NaCl. Our analyses show that these nanostructures have the same pentagonally twinned structure as previously reported one-dimensional palladium nanocrystals, with a thin PVP/iodide surface layer. The Cu(II) ions, when present in sufficient quantities, are hypothesized to scavenge oxygen in solution that would otherwise etch the twinned Pd seeds from which nanowires grow. Furthermore, using larger molecular weight PVP, NaCl promotes growth of nanowires that are even longer than those made with the addition of Cu alone, with nanowire yield remaining high even in the absence of Cu species. This result is attributed to the slower reduction kinetics imparted by $PdCl_4^{2-}$, excess Cl^-, and larger PVP. Knowledge of these critical roles, which have not been elucidated previously, will facilitate large-scale, shape-controlled production of palladium nanocrystals, which is significant given their myriad applications. As one use case, we show that the high aspect ratio of our palladium nanowires makes them uniquely suited to solution-phase manipulation via optoelectronic tweezers, offering a simple means to create customizable arrays of nanowires for potential applications in heterogeneous catalysis.

Chapter 7. Rapid, Solvent-Free Approach to Porous Carbons and their Nanocomposites with Silicon for Electrochemical Energy Storage

7.1. Introduction[6]

Although the processing methodology for carbon aerogel composites outlined in the previous chapters offers rapidity and facile incorporation of additives during synthesis of the polymeric gel precursor, it still has certain drawbacks. First, the necessary solvent exchange and supercritical drying following gelation add several days or more to the process, depending on the size of the gel. In addition, supercritical drying requires high-pressure autoclaves, making it difficult to scale up production to industrial levels. To address these issues, this chapter describes a unique, solvent-free approach to porous carbons and their composites, which allows for rapid, scalable processing from initial reagents to final carbon. This alternative approach is based on the solid-state polymerization of bisphenol A (BPA) with hexamethylenetetramine (HMT), two inexpensive and abundant raw materials, that, when ground together and heated at mild temperatures overnight, below the melting point of both BPA and HMT, cross-link into a resin that can be immediately pyrolyzed in CO_2 to form the porous carbon, requiring less than a day in total. Not only is this significantly faster than RF aerogel formation or traditional wet chemistry approaches to resins that require drying, it is also more environmentally friendly, as the use of organic solvents is completely avoided.

Chemically, our dry BPA-HMT approach is related to RF in that both BPA and resorcinol are phenolic compounds. The use of HMT as a crosslinking agent for phenolic compounds is well-

[6] This work was conducted as an industry collaboration with Group14 Technologies, Inc. using some instrumentation and facilities shared with EnerG2, Inc. All of the experimental methods and analysis herein were conducted by myself, with valuable input and assistance from Group14 colleagues Henry R. "Rick" Costantino, Abirami Dhanabalan, Aaron M. Feaver, Avery J. Sakshaug, and Christopher D. Timmons.

established, being reported as early as 1914.[247] Interestingly, this was the first work to report on the reaction of HMT with anhydrous phenol under mild heating (>60°C), which was observed to evolve ammonia as the only byproduct. However, this cannot strictly be called a dry process as phenol is in a liquid state at 60°C, and presumably acting as a solvent for the HMT. More recently, Sojka, Wolfe, and Guenther[248] probed the mechanism of this cross-linking in water using NMR and FTIR, showing an initial rapid reaction of HMT with phenol to form hydroxybenzylamine intermediates, which can then react with free phenol molecules to form methylene bridges. HMT is also known to decompose to ammonia and formaldehyde in water, particularly under acidic conditions or heating, making it useful as a secondary crosslinker for conventional phenol–formaldehyde resins.[249,250]

A few studies have been published on the application of HMT to porous carbons, though only in catalytic amounts. Wu et al. used HMT as a basic catalyst and secondary crosslinking agent for resorcinol–furaldehyde aerogels in isopropanol, and showed that the mesopore volume of the aerogels following carbonization varied with the ratio of resorcinol to HMT.[251] Similarly, García et al. used HMT as an additive for resorcinol–furaldehyde gels in tert-butyl alcohol/water mixtures, and elucidated its role in determining porosity and pore size.[252] A recent patent application filed by Costantino and colleagues at EnerG2 touches on BPA and HMT as one means for solvent-free processing of porous carbons.[253] However, to the best of our knowledge, there are no reports from other sources on the use of HMT to develop carbon materials in a solvent-free preparation, nor on its use as the primary crosslinker, nor on the use of BPA as the phenolic component. This chapter provides further insight on the dry BPA-HMT process to produce micro-/mesoporous carbons—featuring surface areas more than double those of our RF-based carbon

aerogels—and demonstrates the incorporation of graphite and ammonium dihydrogen phosphate (ADP) additives to tune their pore size and electrochemical properties.

Beyond examining their obvious promising application for supercapacitor electrodes, we also study our BPA-HMT carbons as scaffolds for silicon–carbon (Si–C) nanocomposites for lithium-ion battery anodes. As mentioned in the introduction, silicon offers a very high lithium capacity but its performance is hampered by the large accompanying volume changes, whose detrimental effects can be lessened by reducing the size of the silicon to the nanoscale. The approach we pursue is to deposit amorphous silicon within the nanoscale pores of our BPA-HMT carbon, which can accommodate the lithiation-induced expansion while providing good electrical conductivity, mechanical and chemical stability. We show that Si–C composites made this way offer the high capacity imparted by silicon, while having excellent cycling stability and rate capability.

7.2. Materials and Methods

7.2.1. Synthesis of Carbons and Composites

In a typical resin synthesis, 6 g BPA and 2.47 g HMT were ground together thoroughly in a mortar and pestle (molar ratio of BPA to HMT = 3:2). For samples made with graphite and ADP, 0.1 g and 8.47 g respectively were ground together with the BPA and HMT. The graphite additive was a synthetic ultrafine graphite powder supplied by Asbury Graphite Mills, grade 4124, with mean particle size < 3.0 μm and resistivity 0.29 Ω/cm. The powder mixture was then placed in an aluminum weigh pan, covered loosely with aluminum foil, and cured in an oven at 130°C for at least 16 h. Upon curing, the samples formed hard resins with a fishy odor. Additive-free resins were bright yellow, and resins loaded with graphite and ADP were dark gray to black. The resins

were removed from the pans and crushed in a plastic bag with a hammer until the largest pieces were no more than 5 mm across.

The crushed resin was spread out in an alumina boat and heated in an alumina tube furnace, under flowing CO_2 (0.55 L/min) with a 1 h ramp to the desired temperature and dwell time, ranging from 800–1000°C for 1–3 h. This treatment simultaneously pyrolyzes and activates the sample to enhance its porosity and surface area, due to the reverse Boudouard reaction ($C + CO_2 = 2CO$).[254] The pyrolysis temperature and time were varied to achieve a final carbon surface area of 1600–1900 m^2/g and pore volume of 0.7–1.0 cm^3/g, as these properties were found to be optimal to achieve the target silicon weight loading in the composites while minimizing residual surface area. At the end of the dwell period, the flow gas was switched to N_2 and the furnace cooled naturally. The resulting black carbon (denoted BHC for the sample made without additives and BHAGC for the sample made with ADP and graphite) was crushed again in a mortar and pestle (as pyrolysis tended to make the material cake together), ground further in a Fritsch Pulverisette rotary mill, and passed through a sieve (opening size ~25 μm) to obtain a fine powder.

For silicon incorporation, the sieved carbon was spread out in an alumina boat and subjected to a silane decomposition process in a furnace at 400–600°C for several hours. The time was varied to achieve a target silicon weight loading of 40–50 wt% and surface area < 20 m^2/g. The resulting slate-gray Si–C composite powder was passed again through the 25 μm sieve; it was denoted BHC-S or BHAGC-S according to the carbon that was used as the scaffold.

7.2.2. Characterization

Nitrogen porosimetry and accompanying analysis was performed identically to the graphene aerogels (see Section 2.2.2). Particle size measurements were obtained using a laser diffraction-

based instrument (Malvern MasterSizer 3000). The powders were stirred and sonicated in water at a dilute concentration in the automated dispersion unit (Hydro MV) attached to the instrument.

Scanning electron microscopy (SEM) with accompanying energy-dispersive X-ray spectroscopy (EDS) was performed on a FEI Sirion field-emission SEM with 10 kV accelerating voltage and an attached Oxford X-Max silicon drift detector. Transmission electron microscopy (TEM) was performed on a FEI Tecnai G2 F20 with 200 kV accelerating voltage. X-ray diffraction was obtained on a Bruker D8 Discover X-ray diffractometer equipped with a two-dimensional area detector and a Cu K_α source at 1.54 Å.

Raman spectra were obtained on a Renishaw inVia Raman microscope with 514 nm laser excitation, operated at a low power to avoid photothermal heating effects. FTIR spectra were obtained on a ThermoScientific Nicolet iS10 instrument using the attenuated total reflectance (ATR) technique with a diamond ATR crystal. Spectra of the carbon scaffolds and composites exhibited an upward-sloping baseline toward lower wavenumber, characteristic of carbon-rich samples due to light scattering.[255] A multi-point baseline correction was applied to these scaffolds to better resolve the absorption peaks.

Thermogravimetric analysis (TGA) of the BPA-HMT resin was performed with a TA Instruments Discovery SDT 650. The crushed sample was loaded in a 90 μL alumina crucible and heated under flowing CO_2 (80 mL/min) to 950°C at 15.8°C/min, corresponding to a 1 h ramp.

7.2.3. Lithium-Ion and Supercapacitor Electrode Fabrication and Testing

To process the composites into electrodes for Li-ion testing, the sieved powder was combined with 5% w/w sodium carboxymethylcellulose (Na-CMC) solution in water and SUPER C45 carbon black such that the weight ratio of composite:Na-CMC:SUPER C45 was 60:20:20. This

corresponds to a total solid to solvent weight ratio of 1:3.8. The components were homogenized in a Thinky planetary mixer, and the slurry was blade-coated onto etched copper foil (foil thickness ~ 17 μm) at room temperature. The coated foil was dried in an oven at 60–80°C and calendered so that the final thickness of the coating was uniform and around 30 μm. 0.5 inch diameter circular electrodes were punched out from the sheet, dried in a vacuum oven at 120°C for 1.5 h, and transferred to an argon-filled glovebox. In the glovebox, Li-ion half-cells were assembled within CR2032 coin cell casings, with lithium foil as the counter-electrode, trilayer polypropylene/polyethylene/ polypropylene separator (Celgard 2325), and 1 M $LiPF_6$ in ethylene carbonate/diethyl carbonate (EC:DEC, 2:1 w/w) + 10% fluoroethylene carbonate (FEC) as the electrolyte.

The cells were subjected to galvanostatic charge–discharge tests in the range of 0.005–0.8 V vs. Li^+/Li using a BioLogic VMP3 multi-channel testing system. The cells were kept in an environmental chamber (TestEquity TEC1) at 25.0°C for the entire duration of testing. The cells were first held at OCV for 6 h to ensure complete permeation of the electrolyte. They were then subjected to 5 cycles at 120 mA/g (normalized to the mass of Si–C composite in the electrode), 25 cycles at 240 mA/g, and finally 20 cycles at 600 mA/g. These currents correspond to C-rates of C/10, C/5, and C/2 respectively based on a nominal capacity of 1200 mAh/g. At the end of each charge (lithiation) half-cycle, the potential was held at 0.005 V until the current dropped to 60, 60, and 300 mA/g respectively for the 120, 240, and 600 mA/g test regimes. To determine electrode expansion, following the 50 galvanostatic cycles, the cells were charged back to 0.005 V at 240 mA/g and held at that voltage until the current dropped to 60 mA/g. The cell was then disassembled and the thickness of the fully lithiated anode was measured with a micrometer immediately to minimize air oxidation.

As with the current densities, all reported specific capacities are normalized to the mass of Si–C composite in the electrode. Although carbon blacks such as SUPER C45 exhibit reversible lithium capacity in half-cell systems similar to ours, it is only on the order of 100 mAh/g in the current density range used in our tests.[256] The contribution of the carbon black thus comes out to less than 3% of the overall reversible capacity of the electrodes observed at 240 mA/g.

For supercapacitor evaluation, the additive-free BPA-HMT carbons were processed into coin cell electrodes and tested similarly to our previously discussed carbon aerogels. Briefly, a mixture of 92.2 wt% milled/sieved carbon, 4.9 wt% carbon black (Ketjenblack, AkzoNobel), and 2.9 wt% Teflon tape was ground in a mortar and pestle until it became a homogeneous amalgam, which was then flattened to a thickness of ~50 μm. 5/8 inch diameter electrodes were punched out from this sheet, dried in vacuum at 120°C for 1.5 h, and transferred to an argon-filled glovebox, where they were assembled into CR2325 coin cells. A symmetric two-electrode configuration was employed, with a cellulose separator (NKK TF4035), carbon black (Timcal SUPER-P) @ aluminum foil current collectors, and 1 M tetraethylammonium tetrafluoroborate (TEABF4) in acetonitrile as the electrolyte. Supercapacitor testing and capacitance evaluation were identical to the graphene aerogels (see Section 2.2.4).

7.3. Results and Discussion

7.3.1. Pore Structure

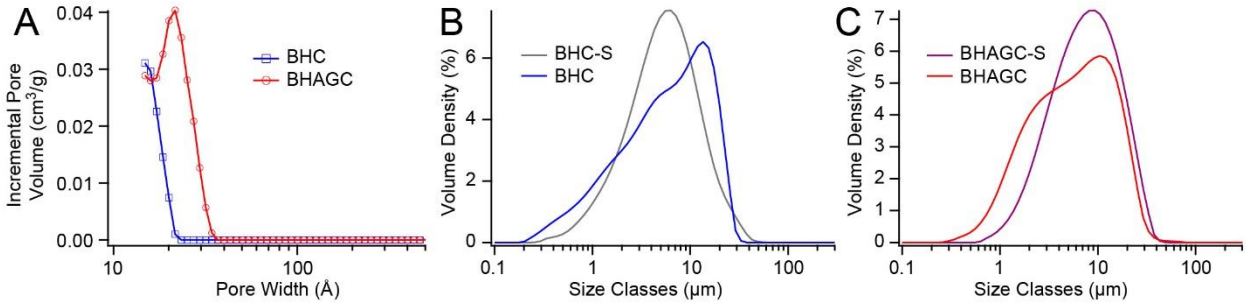

Figure 7.1. (a) Pore size distributions for the carbon scaffolds from nitrogen sorption. Particle size distributions for **(b)** BHC and BHC-S and **(c)** BHAGC and BHAGC-S, obtained from laser scattering measurements.

Table 7.1. Specific surface area and pore volume of carbons and Si–C composites.

	BHC	**BHC-S**	**BHAGC**	**BHAGC-S**
Surface Area (m^2/g)	1647	19	1641	1.9
Pore Volume (cm^3/g)	0.684	0.0083	0.754	0.0028

Nitrogen sorption was performed on the ground carbons and sieved Si–C composites to obtain their surface area and pore characteristics. Both carbons had surface areas exceeding 1600 m^2/g—more than twice that of our RF-based carbon aerogels—as well as pore volumes over 0.6 cm^3/g, attesting to their highly porous nature. Interestingly, both carbons had well-defined pore sizes, with almost all pores less than 50 Å wide (Figure 7.1a). Furthermore, BHC was almost entirely microporous (pore diameter < 20 Å), whereas BHAGC featured somewhat larger pores that extended into the mesopore range (diameter = 20–50 Å).

Nitrogen sorption was also performed after silicon deposition to verify that the process effectively infiltrated the carbon scaffolds. A large reduction in specific surface area and pore volume is desired to minimize irreversible side reactions and accompanying capacity fade. This turned out to be the case, as the surface area and pore volume of both samples became almost negligible upon silicon incorporation (Table 7.1). Furthermore, particle size measurements show that silicon incorporation did not appreciably change particle size relative to the bare carbon

scaffold (Figure 7.2b, c), suggesting that the silicon mainly filled the pores of the scaffold, as opposed to capping pores or bridging particles. This result is also desirable as it minimizes the size of the silicon, ensures electrically conductive pathways and accommodation of the volume changes during lithium insertion and extraction.

It is hypothesized that the larger average pore size of the ADP-loaded carbons is attributed to the decomposition products of ADP during pyrolysis. ADP melts at 190°C with subsequent decomposition to orthophosphoric acid (H_3PO_4) and ammonia at 210°C; this is followed by transformations to pyrophosphoric acid ($H_4P_2O_7$), and then metaphosphoric acid (HPO_3), both steps accompanied by loss of water.[257] This process would open up voids in the resin previously occupied by the ADP crystals. Furthermore, phosphoric acid is a well-known chemical activating agent to prepare activated carbons from cellulosic precursors, and it has been proposed that at 400–700°C, phosphoric acid species can further dehydrate to form P_4O_{10}, which can react with the carbon to generate new pores along with CO_2.[258,259] This would also explain the observation that the ADP-loaded samples required less pyrolysis time to achieve a comparable surface area and pore volume to the additive-free samples.

7.3.2. Compositional Analysis

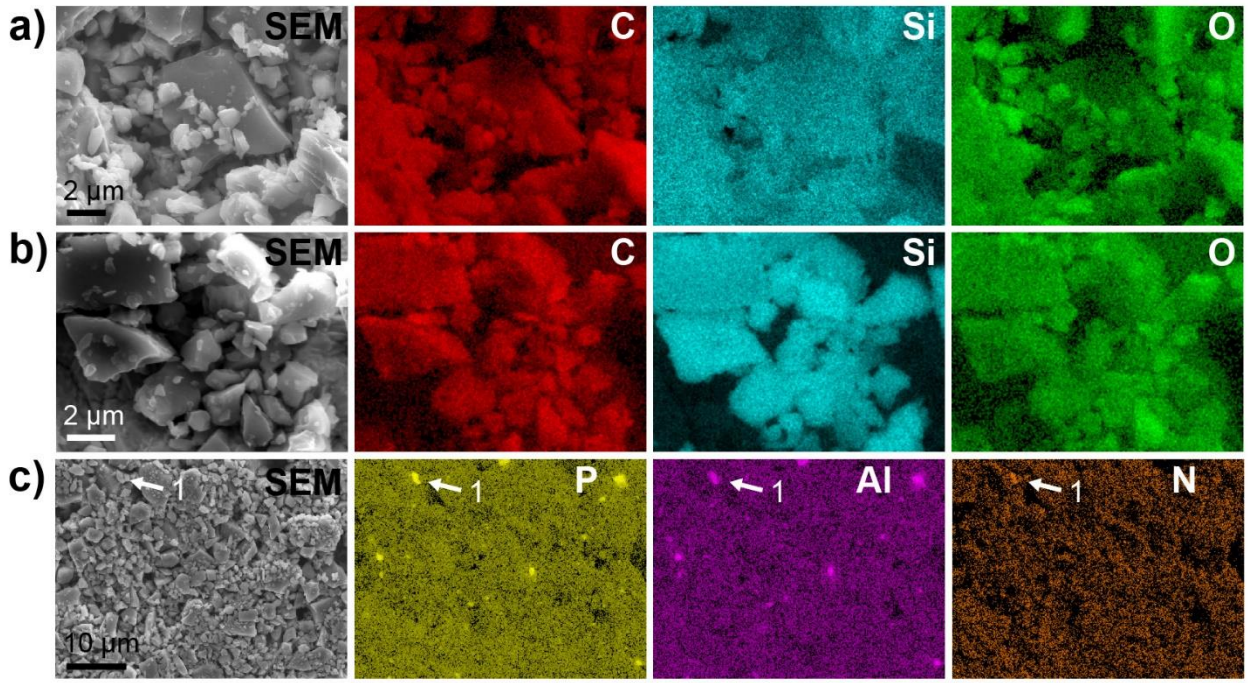

Figure 7.2. SEM-EDS characterization of carbons and composites. SEM image with corresponding elemental maps of C, Si, and O for **(a)** BHC-S, **(b)** BHAGC-S. **(c)** Lower-magnification SEM image with elemental maps of P, Al, and N for BHAGC-S. Arrow labeled '1' denotes a region of concentrated P, Al, and N that is quantified in Table 7.2.

Table 7.2. Elemental quantifications from EDS of carbons and composites.

	Quantity (wt%)				
Element	**BHC**	**BHC-S**	**BHAGC**	**BHAGC-S**	**BHAGC-S, Particle 1**
C	95.14 ± 0.27	43.62 ± 0.27	84.26 ± 0.16	33.54 ± 0.29	26.92 ± 0.27
O	4.86 ± 0.14	11.10 ± 0.14	10.61 ± 0.14	18.93 ± 0.17	30.26 ± 0.21
Si	—	45.28 ± 0.23	—	45.23 ± 0.23	21.27 ± 0.15
P	—	—	4.95 ± 0.07	2.13 ± 0.07	14.20 ± 0.13
Al	—	—	0.18 ± 0.03	0.18 ± 0.04	2.62 ± 0.05
N	—	—	—	—	4.73 ± 0.26

SEM-EDS mapping of the Si–C composites indicates a uniform coating of silicon (Figure 7.2a, b). Quantification of the accompanying spectra (Table 7.2) gives similar silicon concentrations of 45.2 wt% for BHAGC-S and 45.3 wt% for BHC-S. These values are not far off from weight gain measurements of the samples following silicon incorporation, which give 39.5 wt% Si for BHAGC-S and 44.5 wt% Si for BHC-S, assuming all of the deposited material is silicon. However, EDS shows that this is not true; the deposited material contains a non-negligible amount

of oxygen as well, as the measured oxygen content in both composites (18.9 wt% for BHAGC-S and 11.1 wt% for BHC-S) is significantly higher than in the scaffolds alone. This, in turn, implies that EDS slightly overestimates the proportion of deposited material in the composites, which makes sense given that EDS is a surface technique with limited depth resolution of 1–2 μm.

EDS mapping shows that oxygen, as with silicon, is uniformly distributed over the particles of the composites, consistent with surface oxidation (SiO_x). Such oxidation is inevitable considering the prolonged exposure of the composites to air following silicon deposition, as they were being processed into electrodes. This is not necessarily undesirable from the standpoint of electrochemical performance. Although oxidation of silicon is known to lower the first-cycle Coulombic efficiency and increase electronic resistance, SiO_x also serves as a passivating layer to restrict expansion of the underlying silicon and stabilize the solid–electrolyte interphase (SEI), improving rate capability.[260]

Besides silicon and oxygen, EDS shows residual phosphorus in the carbons and composites produced with ADP. BHAGC had a small phosphorus content of 4.95 wt%, which was reduced to 2.13 wt% in BHAGC-S due the added mass from silicon loading, whereas no phosphorus was detected in BHC or BHC-S. Lower-magnification EDS maps of BHAGC and BHAGC-S show that the phosphorus is uniformly distributed on most particles, but a few particles had significantly higher phosphorus concentration than the bulk, with one such particle, labeled '1' in Figure 7.2c, containing 14.2 wt% phosphorus (Table 7.2). Aluminum and oxygen were also enriched in these regions, suggesting that they are aluminophosphate inclusions that were formed from etching of the alumina boat by the phosphoric acid decomposition products of ADP during pyrolysis. In support of this hypothesis as opposed to simple contamination from the boat, no aluminum was detected in BHC or BHC-S.

In addition, nitrogen could not be reliably detected by EDS in the bulk of either composite or carbon scaffold, although the previous patent literature has demonstrated that carbons produced from additive-free BPA-HMT resins by a similar process to the one described herein contain 1–4% nitrogen from CHN combustion analysis.[253] This apparent lack of nitrogen from EDS may be due to its already low concentration in the sample, combined with the low characteristic X-ray energy of nitrogen ($N_{K\alpha 1}$ = 0.392 keV), which could cause the generated X-rays to be reabsorbed by the sample before reaching the detector. However, EDS did detect appreciable quantities of nitrogen in some regions of BHAGC and BHAGC-S, as with particle 1 in Figure 7.2c. This extra nitrogen likely comes from non-volatile decomposition products of ADP or by-products of its reaction with alumina, rather than from HMT, given the coincidence of this N-rich area with the P, Al, and O-rich area, and the fact that no nitrogen was detected in any scans of BHC or BHC-S. Obviously, the inhomogeneity of these elements and the introduction of aluminum as an impurity are undesirable from a materials development perspective, and could be avoided in future experiments by using a boat made out of graphite or other thermally stable, acid-resistant material.

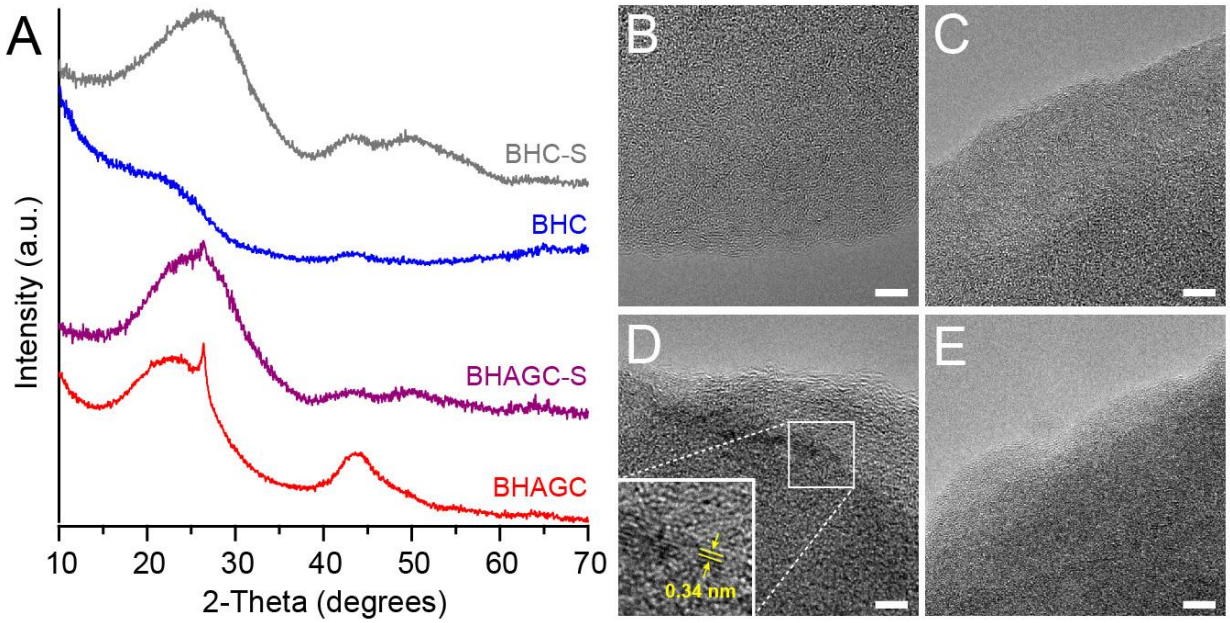

Figure 7.3. **(a)** XRD patterns of carbons and composites. Bright-field TEM images of **(b)** BHC, **(c)** BHC-S, **(d)** BHAGC with inset showing embedded graphite with interlayer spacing of 0.34 nm, **(e)** BHAGC-S. Scale bar = 5 nm.

XRD patterns of the composites prove that both the carbon scaffolds and the deposited silicon are amorphous. The only sharp peak, characteristic of a crystalline material, is in BHAGC-S and BHAGC at 2θ = 26.4°, and originates from the (002) basal planes of the graphite additive (Figure 7.3a). The lack of other crystalline peaks also proves that the ADP completely decomposed and that the phosphorus did not incorporate into the carbon or silicon as a separate crystalline phase. The other features in the XRD patterns are broad humps typical of amorphous materials. In the composites, the humps centered at 2θ = 23° and 43.5° come from the carbon scaffolds, whereas the broadening of the first hump toward higher 2θ, along with the weaker hump at 2θ = 50°, are from amorphous silicon (a-Si), matching earlier studies of a-Si thin films.[261] These results are corroborated by high-resolution TEM images, which show no long-range atomic ordering (Figure 7.3b–d), except for BHAGC, where layered graphitic structures are clearly visible embedded in the amorphous carbon bulk. These structures are not visible in BHAGC-S, presumably obscured by the silicon coating.

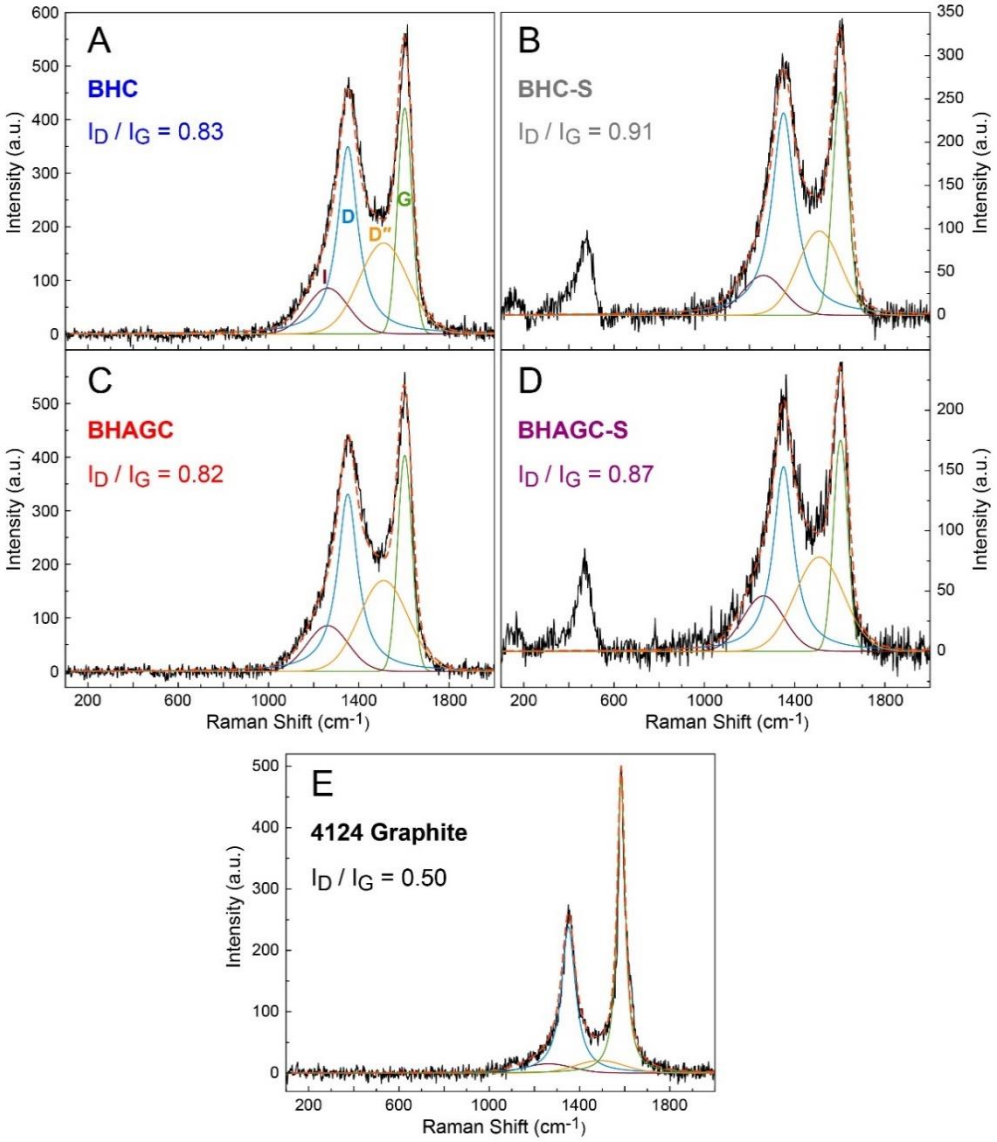

Figure 7.4. Raman spectra of carbons, composites, and 4124 graphite additive with deconvoluted carbon regions showing I, D, D″, and G bands.

Raman spectra of the composites also confirm the amorphicity of the silicon, with broad peaks centered at ~150 and ~480 cm^{-1} originating from the transverse acoustic (TA) and transverse optical (TO) phonons of a-Si, rather than a sharp peak at ~520 cm^{-1} characteristic of crystalline Si (T2g mode, Figure 7.4).[262,263] It is difficult to verify Si-O or Si-P bonding, as the Raman spectrum of SiO_x is similar to that of a-Si, and the Si-P stretching region (400–500 cm^{-1}) overlaps with the broad a-Si band.[264,265] However, on other accounts there is no evidence that the Si coating is chemically bonded to the carbon scaffold, as there are no peaks between 500 and 1000 cm^{-1}, where

Raman-active vibrational modes for Si-C and Si-N occur.[266–268] For the ADP-loaded samples, P-C bonds are also ruled out, as their associated stretching modes are in the 650–770 cm^{-1} range.[269] It is therefore likely that the phosphorus has incorporated into the carbon via P-O-C bonds, which is supported by FTIR analysis, as discussed below. In addition, P-O-C species are known to be more thermally stable, surviving temperatures as high as 1000°C, compared to P-C or P-N species which start to decompose around 800°C.[270]

As with the RF-based carbon aerogels, the peak intensity ratio of the D band to the G band (I_D/I_G) is a rough measure of disorder in the carbon, and can be determined by deconvolution into the D, G, D″, and I bands. The D band was fitted to a Lorentzian function, and the I and D″ bands were fitted to Gaussian functions as previously described, but in this case the G band was fitted to a Gaussian function, for all samples except for the 4124 graphite, where a Lorentzian function was used similar to the aerogels. As shown by Ferrari and Robertson, the D and G bands of amorphous carbons can show features of either Gaussian or Lorentzian curves depending on their microstructure, and there is no *a priori* reason to choose one function over the other for fitting.[271]

Both composites and their scaffolds had the same D and G peak positions at 1351 and 1603 cm^{-1} respectively, as well as similar I_D/I_G ratios in the 0.8–0.9 range, suggesting that the additives and silicon incorporation did not significantly alter the structure of the carbon matrix. However, the I_D/I_G ratios for the composites are slightly higher than their corresponding scaffolds, indicating additional disordering or defect formation in the scaffold during silicon deposition that may be attributed to the prolonged high-temperature condition of the process. As expected, the pure 4124 graphite powder had a considerably lower I_D/I_G (0.50) than the BPA-HMT carbons. The narrower D and G bands, the down-shift of the G peak position to 1584 cm^{-1} (closer to that of bulk graphite), and the markedly less intense I band also attest to its predominantly sp^2 nature.[272] Presumably,

the closer resemblance of the spectrum of BHAGC to BHC, despite the presence of 4124 graphite in the former, is due to the relatively low loading of graphite. Based on the combined yield of BHAGC from cure and pyrolysis, and assuming that all the graphite is preserved during those processes, the final carbon contains only ~10 wt% graphite.

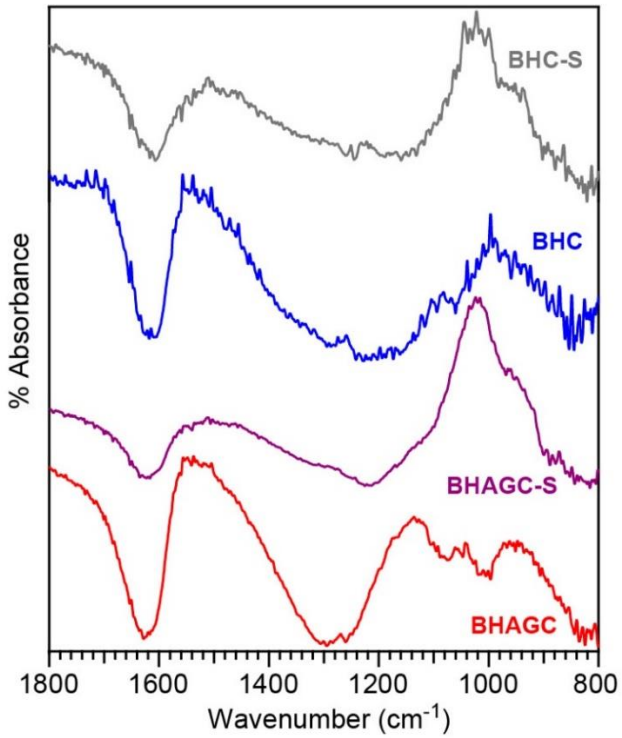

Figure 7.5. Baseline-corrected FTIR absorbance spectra of carbons and composites.

Molecular bonding in the carbon scaffolds and Si–C composites was also studied by FTIR (Figure 7.5). Interestingly, all the scaffolds show a broad band peaking at 1500–1550 cm^{-1}, which has been ascribed to NH deformation in amides, or the large dynamic charge of delocalized π bonding in carbon networks with high sp^2 content.[75,273] The latter would explain the higher intensity of this peak for BHAGC, which contained the graphite additive. Furthermore, BHAGC scaffold exhibits a broad envelope containing three peaks at 1140, 1050, and 970 cm^{-1}, not seen in BHC. The first of these peaks corresponds to C-C-N bending, P=O, or P–aromatic ring stretching, whereas the other two peaks correspond to P-O stretching.[75] BHC instead shows a single broad

peak at 1000 cm^{-1}, corresponding to an aromatic ring breathing mode; it is expected that this would be present in BHAGC as well, but may be convoluted with the aforementioned three-peaked structure.

Like the scaffolds, the spectra of the Si–C composites also feature the broad band at 1550 cm^{-1}, albeit less intense due to the silicon coating on the carbon network. The lower-wavenumber features, however, are replaced by a single prominent peak at 1025 cm^{-1}, which is characteristic of amorphous SiO_x and originates from Si-O-Si antisymmetric stretching.[274] As in Raman, there is no evidence for Si-C bonding, whose vibrations have been reported to appear at 1400 cm^{-1}, 860 cm^{-1}, or 780 cm^{-1}.[275–277]

7.3.3. Chemistry of Resin Curing and Pyrolysis

Additional FTIR studies were performed to examine the chemistry of resin curing and pyrolysis. In the first experiment, a 3:2 BPA-HMT mixture was cured at 130°C for 16 h, and the spectrum of the cured resin was compared to the precursor powder mixture (Figure 7.6b, bottom two plots). The spectrum of the cured resin was in fact similar to the pre-cured mixture, also showing the major peaks attributable to pure BPA and HMT, which suggests the presence of unreacted BPA and HMT in the resin. However, there are several key differences. First, the C-H out-of-plane (oop) bands in the 850–750 cm^{-1} range shift to slightly higher wavenumber upon curing, indicating increased substitution of the aromatic rings. This in turn indicates that cross-linking has occurred, and makes sense in light of previous NMR studies of the reaction mechanism between phenol and HMT showing that methylene bridges form between aromatic rings, similar to other phenolic resins.[248] In addition, the lower intensity of the peak at 1445 cm^{-1} (relative to the rest of the spectrum) and the loss of the broad hump centered at 3300 cm^{-1} in the cured sample, representing in-plane OH bending and O-H stretching respectively, suggest the partial loss of OH groups that

could stem from the formation of methylene ether bridges between the aromatic rings. Finally, the C–N vibration band of raw HMT, at ~1000 cm^{-1}, is split into a doublet in the cured resin. This splitting is consistent with the study of Pshenitsyna and Kotrelev on the reaction mechanism between phenol and HMT, and is hypothesized to arise from hydrogen bonding of the nitrogen atoms on HMT to hydroxyl groups on BPA.[278]

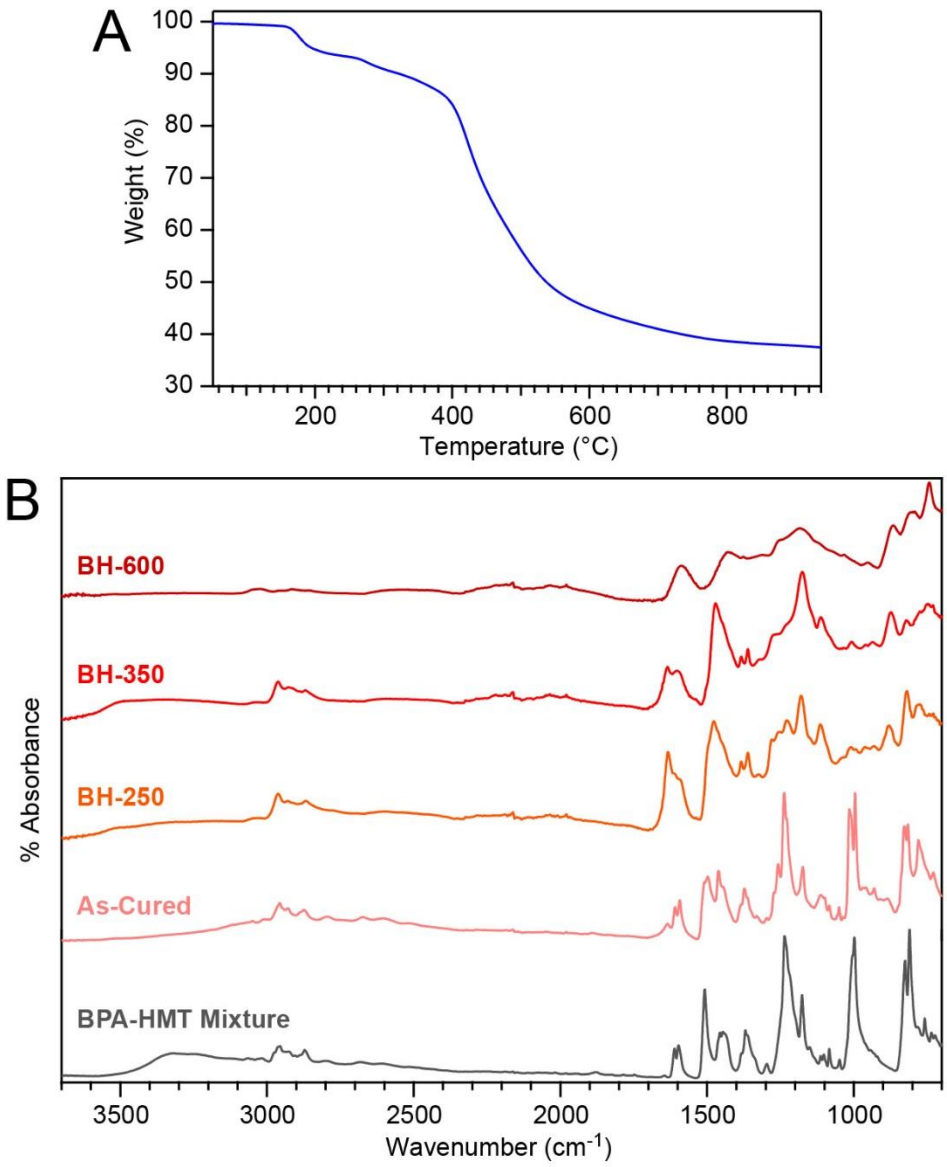

Figure 7.6. **(a)** TGA weight loss curve of a BPA-HMT resin (3:2 molar ratio) from heating to 950°C at 15.8°C/min under CO_2. **(b)** FTIR spectra of 3:2 BPA-HMT mixture prior to curing, after curing, and after heating the cured resin to 250°C, 350°C, and 600°C at the same ramp rate under CO_2.

TGA study of a 3:2 BPA-HMT resin under CO_2 showed three distinct weight loss regions at 150–240°C, 250–310°C, and 370–600°C (Figure 7.6a). To study the chemistry behind each of these weight losses, resin samples that were initially oven-cured at 130°C for at least 16 h were aliquoted, heated in the TGA under CO_2 at 15.8°C/min to 250°C, 350°C, or 600°C, then cooled rapidly by flowing air over the furnace and analyzed with FTIR. The heat-treated resins were called BH-250, BH-350, and BH-600 respectively, and their spectra are presented in Figure 7.6b (top three plots).

For BH-250, most of the peaks from pure BPA or HMT that were present in the initial cured resin are gone, indicating that they have been consumed or volatilized. In particular, the C-N stretching peaks at ~1000 cm^{-1} and 1240 cm^{-1}—among the most prominent peaks in the as-cured resin—as well as the peak at 2875 cm^{-1} representing stretching modes of CH_3 attached to N, have almost vanished in BH-250, suggesting the relatively early loss of nitrogen during pyrolysis. The spectrum of BH-350 looks similar to BH-250, except for the diminished C-H oop peak at 820 cm^{-1} and the diminished C=O stretching peak at 1635 cm^{-1}, indicating additional loss of oxygen. For BH-600, much of the peak structure is lost. The aforementioned C-N and C=O bands completely disappear, as does the C-O or C-O-C stretching band at ~1115 cm^{-1}, but the aromatic ring stretch at 1590 cm^{-1}, C-O stretch at 1180 cm^{-1} and C-H oop modes at low wavenumbers persist. The presence of residual oxygen is consistent with our EDS analysis and makes sense as phenol groups, in particular, have been shown to survive temperatures as high as 1000°C.[66] Additionally, it is worth noting that, as in the cured resin versus uncured mixture, the oop peaks keep shifting to higher wavenumbers from BH-250 to BH-350 to BH-600, suggesting that cross-linking continues over the whole heating regime.

7.3.4. Lithium-Ion Anode Characterization

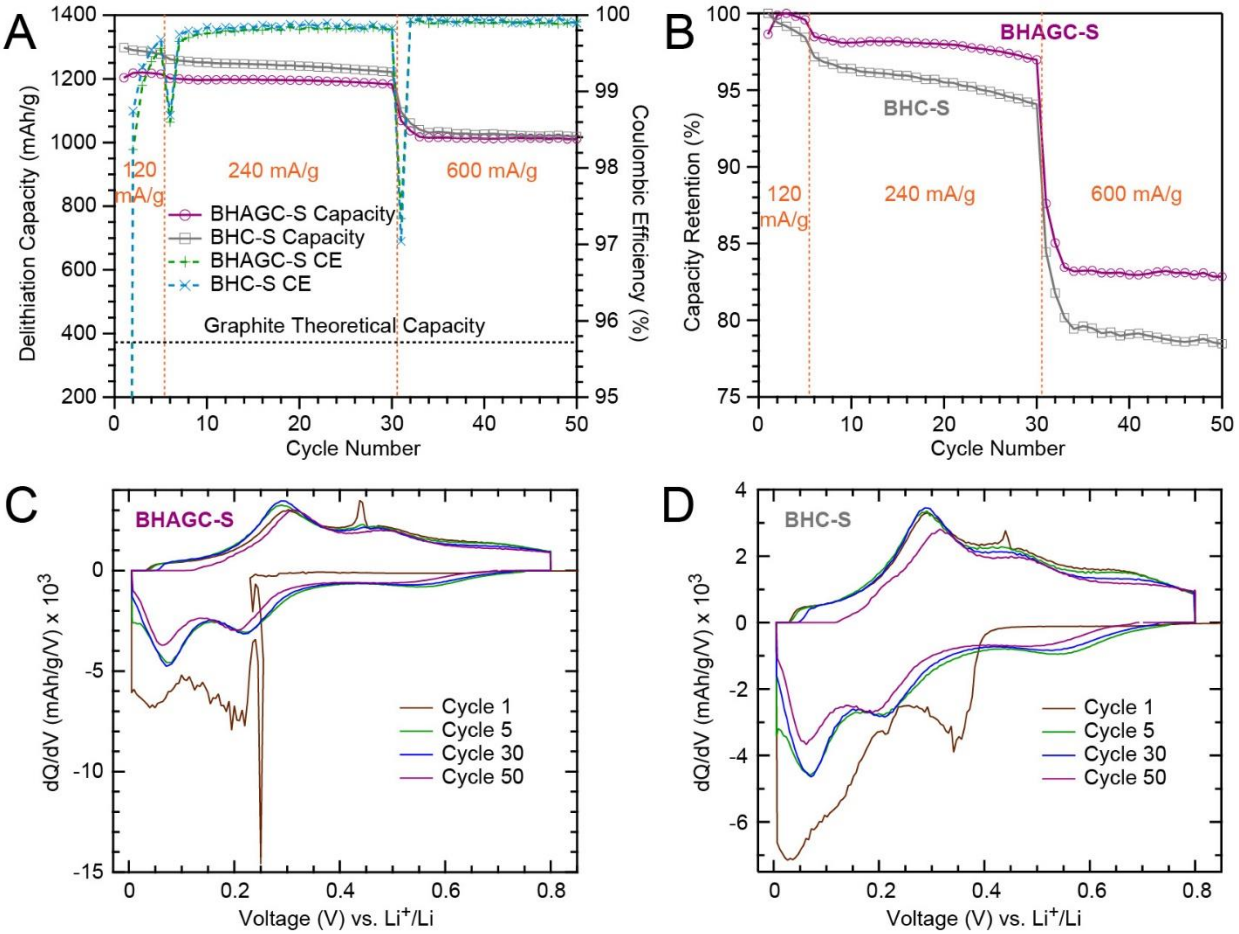

Figure 7.7. Lithium-ion half-cell performance of composites. **(a)** Reversible delithiation capacity (solid lines) and Coulombic efficiency (dashed lines) versus cycle plot. **(b)** Capacity retention versus cycle plot. Differential capacity plots at selected cycles for **(c)** BHAGC-S and **(d)** BHC-S.

Figure 7.7 presents the gravimetric capacities of the composites attained in each extraction (delithiation) half-cycle, along with capacity retention (extraction capacity normalized to the maximum extraction capacity achieved during the test) and Coulombic efficiencies (CE). Both composites exhibit capacities near 1200 mAh/g when cycled at 240 mA/g, more than 3 times the theoretical capacity of graphite, along with excellent stability. Capacity loss is minimal at 240 mA/g, with BHAGC-S and BHC-S maintaining 97% and 94% of their maximum capacities respectively at the end of that regime. Even following the 20 cycles at the fastest current of 600 mA/g, capacity retention is 83% for BHAGC-S and 78% for BHC-S. This represents a major

improvement over bulk micron-thick films of a-Si, where delamination causes the capacity retention to drop precipitously to less than 40% after just 20 cycles at C/10 in a similar half-cell system to ours.[279] Furthermore, the composites feature excellent reversibility in each cycle. BHAGC-S has an average CE of 99.80% for the 240 mA/g cycles, and 99.90% for the 600 mA/g cycles (excluding the first cycles at those rates). For BHC-S, those figures are 99.84% and 99.93% respectively.

Comparing the two composites to one another, while both of them performed impressively relative to bulk silicon and graphite, BHAGC-S shows markedly better rate capability and overall capacity retention than BHC-S. We hypothesize that this improvement comes from the higher electrical conductivity imparted by graphite and phosphorus to the carbon network. Graphite offers delocalized π-electrons whereas phosphorus can act as an n-type dopant in either the amorphous carbon or graphite to further increase the charge carrier density.[280] In addition, phosphorus-doped soft carbons made from impregnation with phosphoric acid, which is one of the thermal decomposition products of ADP, have previously been shown to enhance rate capability over undoped counterparts.[281] Furthermore, the ADP and graphite additives mitigate electrode expansion from lithiation and repeated cycling, as the BHAGC-S electrode exhibited only a 75% increase in thickness, compared to 103% for BHC-S. This illustrates the better containment of silicon particle expansion offered by the larger pores of BHAGC.

Figures 7.7c and 7.7d shows the differential capacity plots of the two electrodes for selected cycles. In the first cycle, several features should be noted that explain the low first-cycle Coulombic efficiencies of both samples (67.3% for BHAGC-S and 72.7% for BHC-S). During initial lithiation of BHAGC-S, a sharp peak appears at 0.25 V that is not observed in subsequent cycles. This may be attributed to nucleation processes during initial lithiation of a-Si,[282] or to an

irreversible reaction between lithium and SiO_x to form the silicate phase, Li_4SiO_4.[274] On the other hand, BHC-S shows a broad irreversible peak centered at 0.36 V during initial lithiation. Incidentally, this may also correspond to Li_4SiO_4, as its formation potential has been shown to vary with the oxygen content of the SiO_x.[283] The formation of other lithium silicates, such as Li_2SiO_3 or $Li_6Si_2O_7$, is also possible.[284] In the first delithiation for both samples, a prominent peak appears at ~0.45 V, corresponding to formation of metastable $Li_{15}Si_4$.[282,285] In subsequent cycles, this peak is reduced to a small blip for BHAGC-S, and completely disappears for BHC-S. Although normally $Li_{15}Si_4$ continues to form with repeated cycling, FEC-containing electrolytes, as used in our cells, form a more compact SEI layer that promotes parasitic reactions with the alkyl carbonates in the solvent that consume $Li_{15}Si_4$. This results in marginal capacity loss but better cyclic stability.[286]

Other reversible peaks characteristic of a-Si appear in the first delithiation and subsequent cycles, at ~0.2 and ~0.07 V during lithiation, and at ~0.29 and ~0.48 V during delithiation.[282,283] The two lithiation peaks of a-Si also appear in the first cycle, but are shifted to a slightly lower potential. This has been shown in various earlier reports and suggests that the chemical processes during the initial lithiation of a-Si differ from subsequent cycles, a hypothesis that has been verified by *in situ* TEM experiments.[34,287] The shift has also been explained in the context of the larger compressive stresses associated with lithiating pristine Si.[282]

As seen in the differential capacity curve for the 50^{th} cycle, when the applied current is increased to 600 mA/g, the peaks shift slightly to lower potentials during lithiation and higher potentials during delithiation. In this case, the shift occurs because of increased polarization of the cell at higher currents.[288] The increased polarization also causes the electrode to reach its

cutoff potential before all its available capacity can be utilized, leading to the drop in specific capacity that is concurrently observed.

7.3.5. Supercapacitor Characterization

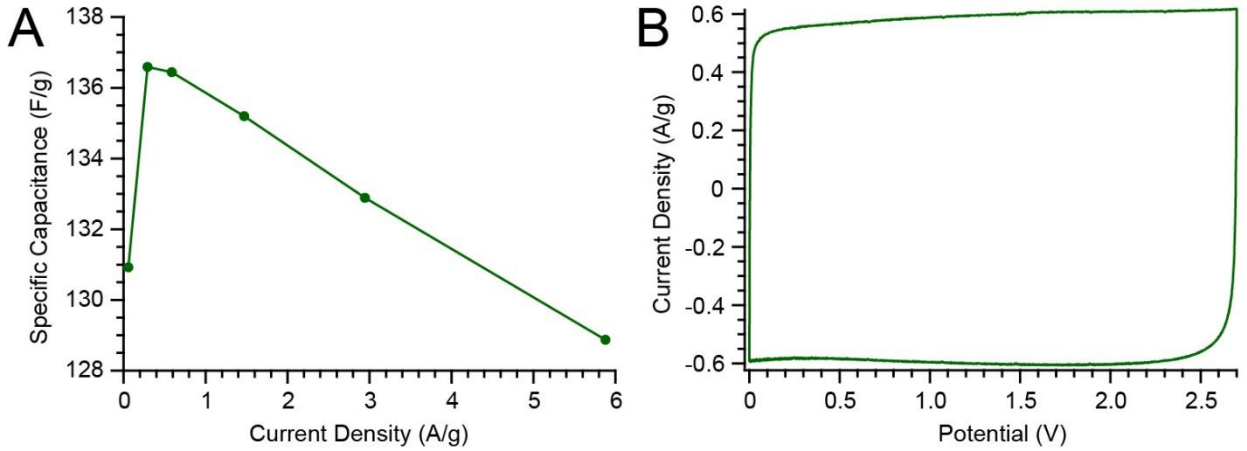

Figure 7.8. Supercapacitor performance of BHC. **(a)** Gravimetric capacitance as a function of applied current density from galvanostatic tests. **(b)** Cyclic voltammogram at sweep rate 20 mV/s.

As proof of concept, we also processed the bare BHC into supercapacitor electrodes, assembled them into coin cells, and tested their performance similarly to our graphene and pure RF carbon aerogels (Section 2.2.4). Figure 7.8a shows the specific capacitance as a function of applied current density, as calculated from galvanostatic discharge profiles and normalized to the total mass of active material in both electrodes. In line with expectations, the sample has a high gravimetric capacitance, peaking at 136.5 F/g—more than twice the maximum capacitance achieved by either the graphene or plain RF carbon aerogels. More importantly, BHC exhibits impressive rate capability compared to the aerogels, with only a slight drop in capacitance to 129 F/g at the highest tested current of 5.9 A/g. The CV curve at 20 mV/s is nearly rectangular (Figure 7.8b), attesting to the near-ideal double-layer capacitive behavior and rapid current response upon voltage reversal.

7.4. Conclusion

In conclusion, we have introduced a solvent-free approach to synthesizing porous carbons based on the solid-state polymerization of BPA and HMT at mild temperatures overnight, followed by simultaneous pyrolysis and activation in CO_2. Because this method eliminates the need for drying, the precursors can be converted to the porous carbon in less than 24 hours total, and large batches can be processed at a time, offering great promise for scalable, high-throughput manufacture. We demonstrate that such carbons are well-suited to supercapacitor applications, but, more importantly, that they can be infiltrated with silicon to form a nanocomposite that features high specific capacity, stability, and rate capability as an anode for lithium-ion batteries. In addition, we show that the microstructural, chemical, and electrochemical properties of these porous carbons and composites can be modified with graphite and phosphate additives to the precursor mixture. Most notably, carbons with these additives exhibit faster activation rate, larger pore sizes, and residual phosphorus content, with the composites featuring even better rate capability than the additive-free composites.

Chapter 8. Conclusions

This thesis can be summarized in the context of processing improvements for porous carbon nanocomposites, with an eye toward scalable production and the ability to texture and pattern the nanomaterials within the composites. In Chapters 2 and 4, I presented the ultrafast synthesis of graphene– and TMD–carbon aerogel composites respectively based on the polymerization of resorcinol and formaldehyde in the presence of solution-exfoliated graphene oxide (GO) and TMD. This distinctive approach uses HCl as the catalyst and acetonitrile as the solvent to reduce the gelation time from many hours or even several days (via the traditional base-catalyzed route) to just 1–2 hours at near-ambient temperatures, making it easier to produce large quantities of these materials within reasonable time. Additionally, for the TMD–carbon aerogel composites, this process offers a safer alternative to the use of pyrophoric chemicals typically used to exfoliate TMDs. Furthermore, both of these aerogel composites outperformed plain RF carbon aerogels as supercapacitor electrodes, illustrating the favorable impact of the additives. Chapter 3 demonstrated the versatility of the graphene aerogels beyond supercapacitor applications by evaluating them as a drug loading host for CoQ_{10}, which preferentially adsorbed on the graphene aerogels due to the π-conjugated structure imparted by graphene.

To address texturing and patterning, Chapter 5 introduced optoelectronic tweezers (OET) and demonstrated its utility in aligning GO particles in bulk, as well as trapping and moving them into arbitrary patterns in water. These manipulations were backed up by a theoretical model of the dielectrophoretic force and drag force on a trapped GO particle to calculate its maximum achievable speed. To dig deeper into another important nanomaterial that can be patterned with OET and investigate a way to control particle shape, which greatly affects the dielectrophoretic force on which OET is based, Chapter 6 presented a simple hydrothermal method to synthesize

large yields of palladium nanowires (PdNWs), mediated by introduction of trace Cu(II) and/or sodium chloride to the precursor solution. These nanowires were observed to have tremendous lengths and aspect ratios, enabling them to be aligned, manipulated, and patterned with ease in OET.

Finally, in Chapter 7, I investigated a different approach to accelerating the synthesis of porous carbons and their nanocomposites, using a solvent-free preparation of the polymer precursor, based on bisphenol A (BPA) and hexamethylenetetramine (HMT). Although this system requires overnight cure at temperatures over 100°C, in contrast to the acid-catalyzed gelation of RF, the need for solvent exchange and supercritical drying is eliminated, saving several days' time, along with the costs associated with supercritical drying. I show that carbons produced by this technique feature even higher surface area and better supercapacitor performance than the RF-based carbon aerogels, and that they can be combined with silicon to form composite anodes for lithium-ion batteries with high capacity and rate capability, which can be further enhanced through incorporation of graphite and phosphate additives.

References

[1] S. Sircar, T. C. Golden, M. B. Rao, *Carbon* **1996**, *34*, 1.
[2] R. L. Culp, G. L. Culp, *Advanced Wastewater Treatment*, Van Nostrand Reinhold, **1971**.
[3] S. Porada, L. Borchardt, M. Oschatz, M. Bryjak, J. S. Atchison, K. J. Keesman, S. Kaskel, P. M. Biesheuvel, V. Presser, *Energy Environ. Sci.* **2013**, *6*, 3700.
[4] Y. Yang, K. Chiang, N. Burke, *Catal. Today* **2011**, *178*, 197.
[5] M. Sevilla, R. Mokaya, *Energy Environ. Sci.* **2014**, *7*, 1250.
[6] S. Kapri, S. Maiti, S. Bhattacharyya, *Carbon* **2016**, *100*, 223.
[7] S. J. Allen, L. Whitten, G. Mckay, *Dev. Chem. Eng. Miner. Process.* **1998**, *6*, 231.
[8] H. Tamon, H. Ishizaka, M. Mikami, M. Okazaki, *Carbon* **1997**, *35*, 791.
[9] S. A. Al-Muhtaseb, J. A. Ritter, *Adv. Mater.* **2003**, *15*, 101.
[10] A. M. ElKhatat, S. A. Al-Muhtaseb, *Adv. Mater.* **2011**, *23*, 2887.
[11] J. Feng, J. Feng, C. Zhang, *J. Porous Mater.* **2012**, *19*, 551.
[12] R. W. Pekala, *J. Mater. Sci.* **1989**, *24*, 3221.
[13] M. A. Aegerter, N. Leventis, M. M. Koebel, *Aerogels Handbook*, Springer Science & Business Media, **2011**.
[14] C. Lin, J. A. Ritter, *Carbon* **1997**, *35*, 1271.
[15] K. Zhang, B. T. Ang, L. L. Zhang, X. S. Zhao, J. Wu, *J. Mater. Chem.* **2011**, *21*, 2663.
[16] M. A. Worsley, T. Y. Olson, J. R. I. Lee, T. M. Willey, M. H. Nielsen, S. K. Roberts, P. J. Pauzauskie, J. Biener, J. H. Satcher, T. F. Baumann, *J. Phys. Chem. Lett.* **2011**, *2*, 921.
[17] S. Mulik, C. Sotiriou-Leventis, N. Leventis, *Chem. Mater.* **2007**, *19*, 6138.
[18] J. Bird, *Electrical Circuit Theory and Technology*, Routledge, **2014**.
[19] H. D. Abruna, Y. Kiya, J. C. Henderson, *Phys. Today* **2008**, *61*, 43.
[20] J. R. Miller, P. Simon, *Science* **2008**, *321*, 651.
[21] J. Li, X. Wang, Y. Wang, Q. Huang, C. Dai, S. Gamboa, P. J. Sebastian, *J. Non-Cryst. Solids* **2008**, *354*, 19.
[22] U. Fischer, R. Saliger, V. Bock, R. Petricevic, J. Fricke, *J. Porous Mater.* **1997**, *4*, 281.
[23] R. Saliger, U. Fischer, C. Herta, J. Fricke, *J. Non-Cryst. Solids* **1998**, *225*, 81.
[24] S. J. Kim, S. W. Hwang, S. H. Hyun, *J. Mater. Sci.* **2005**, *40*, 725.
[25] Y. J. Lee, G.-P. Kim, Y. Bang, J. Yi, J. G. Seo, I. K. Song, *Mater. Res. Bull.* **2014**, *50*, 240.
[26] M. B. Lim, M. Hu, S. Manandhar, A. Sakshaug, A. Strong, L. Riley, P. J. Pauzauskie, *Carbon* **2015**, *95*, 616.
[27] M. Ciszewski, E. Szatkowska, A. Koszorek, M. Majka, *J. Mater. Sci. Mater. Electron.* **2017**, *28*, 4897.
[28] Y.-H. Lin, T.-Y. Wei, H.-C. Chien, S.-Y. Lu, *Adv. Energy Mater.* **2011**, *1*, 901.
[29] J. Li, X. Wang, Q. Huang, C. Dai, S. Gamboa, P. J. Sebastian, *J. Appl. Electrochem.* **2007**, *37*, 1129.
[30] D. Bélanger, T. Brousse, J. W. Long, *Interface* **2008**, *17*, 49.
[31] W. Dmowski, T. Egami, K. E. Swider-Lyons, C. T. Love, D. R. Rolison, *J. Phys. Chem. B* **2002**, *106*, 12677.
[32] M. T. McDowell, S. W. Lee, W. D. Nix, Y. Cui, *Adv. Mater.* **2013**, *25*, 4966.
[33] X. H. Liu, L. Zhong, S. Huang, S. X. Mao, T. Zhu, J. Y. Huang, *ACS Nano* **2012**, *6*, 1522.

[34] M. T. McDowell, S. W. Lee, J. T. Harris, B. A. Korgel, C. Wang, W. D. Nix, Y. Cui, *Nano Lett.* **2013**, *13*, 758.
[35] Y. Xu, Y. Zhu, C. Wang, *J. Mater. Chem. A* **2014**, *2*, 9751.
[36] M.-S. Wang, Y. Song, W.-L. Song, L.-Z. Fan, *ChemElectroChem* **2014**, *1*, 2124.
[37] Z. Wang, F. Li, N. S. Ergang, A. Stein, *Carbon* **2008**, *46*, 1702.
[38] R.-P. Ren, W. Li, Y.-K. Lv, *J. Colloid Interface Sci.* **2017**, *500*, 63.
[39] J. Li, J. Li, H. Meng, S. Xie, B. Zhang, L. Li, H. Ma, J. Zhang, M. Yu, *J. Mater. Chem. A* **2014**, *2*, 2934.
[40] I. Andjelkovic, D. N. H. Tran, S. Kabiri, S. Azari, M. Markovic, D. Losic, *ACS Appl. Mater. Interfaces* **2015**, *7*, 9758.
[41] D. N. H. Tran, S. Kabiri, L. Wang, D. Losic, *J. Mater. Chem. A* **2015**, *3*, 6844.
[42] A. Abdelwahab, J. Castelo-Quibén, M. Pérez-Cadenas, A. Elmouwahidi, F. J. Maldonado-Hódar, F. Carrasco-Marín, A. F. Pérez-Cadenas, *Catalysts* **2017**, *7*, 25.
[43] M. Sánchez-Polo, J. Rivera-Utrilla, J. Méndez-Díaz, J. López-Peñalver, *Ind. Eng. Chem. Res.* **2008**, *47*, 6001.
[44] O. Czakkel, E. Geissler, I. M. Szilágyi, K. László, *Nanomater. Environ.* **2013**, *1*, 23.
[45] A. A. Balandin, S. Ghosh, W. Bao, I. Calizo, D. Teweldebrhan, F. Miao, C. N. Lau, *Nano Lett.* **2008**, *8*, 902.
[46] S. Ghosh, I. Calizo, D. Teweldebrhan, E. P. Pokatilov, D. L. Nika, A. A. Balandin, W. Bao, F. Miao, C. N. Lau, *Appl. Phys. Lett.* **2008**, *92*, 151911.
[47] X. Li, G. Zhang, X. Bai, X. Sun, X. Wang, E. Wang, H. Dai, *Nat. Nanotechnol.* **2008**, *3*, 538.
[48] M. F. El-Kady, V. Strong, S. Dubin, R. B. Kaner, *Science* **2012**, *335*, 1326.
[49] E. H. Hwang, S. Adam, S. Das Sarma, *Phys. Rev. Lett.* **2007**, *98*, 186806.
[50] S. V. Morozov, K. S. Novoselov, M. I. Katsnelson, F. Schedin, D. C. Elias, J. A. Jaszczak, A. K. Geim, *Phys. Rev. Lett.* **2008**, *100*, 16602.
[51] B. Kuchta, L. Firlej, A. Mohammadhosseini, P. Boulet, M. Beckner, J. Romanos, P. Pfeifer, *J. Am. Chem. Soc.* **2012**, *134*, 15130.
[52] G.-H. Lee, R. C. Cooper, S. J. An, S. Lee, A. van der Zande, N. Petrone, A. G. Hammerberg, C. Lee, B. Crawford, W. Oliver, J. W. Kysar, J. Hone, *Science* **2013**, *340*, 1073.
[53] J. Wang, M. Ellsworth, *ECS Trans.* **2009**, *19*, 241.
[54] F. Liu, T. S. Seo, *Adv. Funct. Mater.* **2010**, *20*, 1930.
[55] Y. Xu, K. Sheng, C. Li, G. Shi, *ACS Nano* **2010**, *4*, 4324.
[56] Z. Chen, W. Ren, L. Gao, B. Liu, S. Pei, H.-M. Cheng, *Nat. Mater.* **2011**, *10*, 424.
[57] H. Li, L. Liu, F. Yang, *J. Mater. Chem. A* **2013**, *1*, 3446.
[58] M. A. Worsley, P. J. Pauzauskie, T. Y. Olson, J. Biener, J. H. Satcher, T. F. Baumann, *J. Am. Chem. Soc.* **2010**, *132*, 14067.
[59] Y. Zhu, H. Hu, W. Li, X. Zhang, *Carbon* **2007**, *45*, 160.
[60] J. Li, X. Wang, Q. Huang, S. Gamboa, P. J. Sebastian, *J. Power Sources* **2006**, *158*, 784.
[61] W. Zhang, Z.-H. Huang, C. Zhou, G. Cao, F. Kang, Y. Yang, *J. Mater. Chem.* **2012**, *22*, 7158.
[62] Z.-S. Wu, S. Yang, Y. Sun, K. Parvez, X. Feng, K. Müllen, *J. Am. Chem. Soc.* **2012**, *134*, 9082.
[63] W.-Y. Cheng, C.-C. Wang, S.-Y. Lu, *Carbon* **2013**, *54*, 291.
[64] S. Guo, S. Dong, *Chem. Soc. Rev.* **2011**, *40*, 2644.

[65] S. Park, J. An, I. Jung, R. D. Piner, S. J. An, X. Li, A. Velamakanni, R. S. Ruoff, *Nano Lett.* **2009**, *9*, 1593.
[66] A. Ganguly, S. Sharma, P. Papakonstantinou, J. Hamilton, *J. Phys. Chem. C* **2011**, *115*, 17009.
[67] B. L. Coyle, M. Rolandi, F. Baneyx, *Langmuir* **2013**, *29*, 4839.
[68] K. Guo, H. Song, X. Chen, X. Du, L. Zhong, *Phys. Chem. Chem. Phys.* **2014**, *16*, 11603.
[69] K. K. Aligizaki, *Pore Structure of Cement-Based Materials: Testing, Interpretation and Requirements*, CRC Press, **2005**.
[70] X. Zhao, Y. Li, J. Wang, Z. Ouyang, J. Li, G. Wei, Z. Su, *ACS Appl. Mater. Interfaces* **2014**, *6*, 4254.
[71] J. Li, T. Shirai, M. Fuji, *Adv. Powder Technol.* **2013**, *24*, 838.
[72] F. K. van Dijen, R. Metselaar, *J. Eur. Ceram. Soc.* **1991**, *7*, 177.
[73] S. Hashimoto, S. Ohashi, K. Hirao, Y. Zhou, H. Hyuga, S. Honda, Y. Iwamoto, *J. Ceram. Soc. Jpn.* **2011**, *119*, 740.
[74] M. S. Seehra, A. S. Pavlovic, *Carbon* **1993**, *31*, 557.
[75] J. B. Lambert, H. F. Shurvell, R. G. Cooks, *Introduction to Organic Spectroscopy*, Macmillan, New York, **1987**.
[76] D. W. Boukhvalov, M. I. Katsnelson, *J. Am. Chem. Soc.* **2008**, *130*, 10697.
[77] T. Szabó, O. Berkesi, P. Forgó, K. Josepovits, Y. Sanakis, D. Petridis, I. Dékány, *Chem. Mater.* **2006**, *18*, 2740.
[78] I. Poljansek, M. Krajnc, *Acta Chim. Slov.* **2005**, *52*, 238.
[79] B. H. Stuart, *Infrared Spectroscopy: Fundamentals and Applications*, Wiley, Chichester, West Sussex, England ; Hoboken, NJ, **2004**.
[80] L. M. Malard, M. A. Pimenta, G. Dresselhaus, M. S. Dresselhaus, *Phys. Rep.* **2009**, *473*, 51.
[81] K. Sasaki, Y. Tokura, T. Sogawa, *Crystals* **2013**, *3*, 120.
[82] F. Tuinstra, J. L. Koenig, *J. Chem. Phys.* **1970**, *53*, 1126.
[83] A. C. Ferrari, *Solid State Commun.* **2007**, *143*, 47.
[84] L. G. Cançado, K. Takai, T. Enoki, M. Endo, Y. A. Kim, H. Mizusaki, A. Jorio, L. N. Coelho, R. Magalhães-Paniago, M. A. Pimenta, *Appl. Phys. Lett.* **2006**, *88*, 163106.
[85] A. Sadezky, H. Muckenhuber, H. Grothe, R. Niessner, U. Pöschl, *Carbon* **2005**, *43*, 1731.
[86] J.-M. Vallerot, X. Bourrat, A. Mouchon, G. Chollon, *Carbon* **2006**, *44*, 1833.
[87] J. Kuhn, R. Brandt, H. Mehling, R. Petričević, J. Fricke, *J. Non-Cryst. Solids* **1998**, *225*, 58.
[88] A. S. Milev, N. H. Tran, G. S. K. Kannangara, M. A. Wilson, *Phys. Chem. Chem. Phys.* **2010**, *12*, 6685.
[89] F.-Y. Yuan, H.-B. Zhang, X. Li, H.-L. Ma, X.-Z. Li, Z.-Z. Yu, *Carbon* **2014**, *68*, 653.
[90] S. Roldán, D. Barreda, M. Granda, R. Menéndez, R. Santamaría, C. Blanco, *Phys Chem Chem Phys* **2015**, *17*, 1084.
[91] A. Balakrishnan, K. R. V. Subramanian, *Nanostructured Ceramic Oxides for Supercapacitor Applications*, CRC Press, Boca Raton, **2014**.
[92] J. Bisquert, *Phys. Chem. Chem. Phys.* **2000**, *2*, 4185.
[93] M. D. Stoller, S. Park, Y. Zhu, J. An, R. S. Ruoff, *Nano Lett.* **2008**, *8*, 3498.
[94] C. Du, N. Pan, *Nanotechnology* **2006**, *17*, 5314.
[95] K. Xu, R. Zou, W. Li, Q. Liu, T. Wang, J. Yang, Z. Chen, J. Hu, *New J. Chem.* **2013**, *37*, 4031.

[96] M. D. Stoller, R. S. Ruoff, *Energy Environ. Sci.* **2010**, *3*, 1294.
[97] M. M. Shaijumon, F. S. Ou, L. Ci, P. M. Ajayan, *Chem. Commun.* **2008**, 2373.
[98] H. Valo, S. Arola, P. Laaksonen, M. Torkkeli, L. Peltonen, M. B. Linder, R. Serimaa, S. Kuga, J. Hirvonen, T. Laaksonen, *Eur. J. Pharm. Sci.* **2013**, *50*, 69.
[99] B. S. K. Gorle, I. Smirnova, M. Dragan, S. Dragan, W. Arlt, *J. Supercrit. Fluids* **2008**, *44*, 78.
[100] A. Kumer Roy, S.-M. Kim, P. Paoprasert, S.-Y. Park, I. In, *RSC Adv.* **2015**, *5*, 31677.
[101] Ç. Defteralı, R. Verdejo, S. Majeed, A. Boschetti-de-Fierro, H. R. Méndez-Gómez, E. Díaz-Guerra, D. Fierro, K. Buhr, C. Abetz, R. Martínez-Murillo, D. Vuluga, M. Alexandre, J.-M. Thomassin, C. Detrembleur, C. Jérôme, V. Abetz, M. Á. López-Manchado, C. Vicario-Abejón, *Front. Bioeng. Biotechnol.* **2016**, *4*, DOI 10.3389/fbioe.2016.00094.
[102] C. A. García-González, M. Alnaief, I. Smirnova, *Carbohydr. Polym.* **2011**, *86*, 1425.
[103] C. Maderuelo, A. Zarzuelo, J. M. Lanao, *J Control Release* **2011**, *154*, 2.
[104] B. S. K. Gorle, I. Smirnova, M. A. McHugh, *J. Supercrit. Fluids* **2009**, *48*, 85.
[105] M. Alnaief, S. Antonyuk, C. M. Hentzschel, C. S. Leopold, S. Heinrich, I. Smirnova, *Microporous Mesoporous Mater.* **2012**, *160*, 167.
[106] I. Smirnova, S. Suttiruengwong, M. Seiler, W. Arlt, *Pharm Dev Technol* **2004**, *9*, 443.
[107] J. Salonen, L. Laitinen, A. M. Kaukonen, J. Tuura, M. Björkqvist, T. Heikkilä, K. Vähä-Heikkilä, J. Hirvonen, V.-P. Lehto, *J. Controlled Release* **2005**, *108*, 362.
[108] G. P. Littarru, L. Tiano, *Mol Biotechnol* **2007**, *37*, 31.
[109] B. Frei, M. C. Kim, B. N. Ames, *Proc Natl Acad Sci U A* **1990**, *87*, 4879.
[110] H. N. Bhagavan, R. K. Chopra, *Free Radic Res* **2006**, *40*, 445.
[111] A. Abadi, J. D. Crane, D. Ogborn, B. Hettinga, M. Akhtar, A. Stokl, L. Macneil, A. Safdar, M. Tarnopolsky, *PLoS One* **2013**, *8*, e60722.
[112] Y. Hatefi, *Adv. Enzymol. Relat. Subj. Biochem.* **1963**, *25*, 275.
[113] S. Brunauer, P. H. Emmett, E. Teller, *J. Am. Chem. Soc.* **1938**, *60*, 309.
[114] E. P. Barrett, L. G. Joyner, P. P. Halenda, *J. Am. Chem. Soc.* **1951**, *73*, 373.
[115] G. Reina, J. M. González-Domínguez, A. Criado, E. Vázquez, A. Bianco, M. Prato, *Chem. Soc. Rev.* **2017**, *46*, 4400.
[116] S. Y. Lagergren, *Zur Theorie Der Sogenannten Adsorption Gelöster Stoffe*, **1898**.
[117] G. Crini, P.-M. Badot, *Sorption Processes and Pollution: Conventional and Non-Conventional Sorbents for Pollutant Removal from Wastewaters*, Presses Univ. Franche-Comté, **2010**.
[118] Y. S. Ho, G. McKay, *Process Saf. Environ. Prot.* **1998**, *76*, 332.
[119] Y. S. Ho, G. McKay, *Process Biochem.* **7**, *34*, 451.
[120] E. Lichtfouse, J. Schwarzbauer, D. Robert, *Green Materials for Energy, Products and Depollution*, Springer Science & Business Media, **2013**.
[121] S. Nazzal, N. Guven, I. K. Reddy, M. A. Khan, *Drug Dev Ind Pharm* **2002**, *28*, 49.
[122] Y. Zhao, Y.-H. Sun, Z.-Y. Li, C. Xie, Y. Bao, Z.-J. Chen, J.-B. Gong, Q.-X. Yin, W. Chen, C. Zhang, *J. Solut. Chem.* **2013**, *42*, 764.
[123] K. Dasgupta, J. Prakash, B. M. Tripathi, *J. Nucl. Mater.* **2014**, *445*, 72.
[124] H. Shang, Y. Lu, F. Zhao, C. Chao, B. Zhang, H. Zhang, *RSC Adv.* **2015**, *5*, 75728.
[125] H. Katsikas, P. J. Quinn, *J. Bioenerg. Biomembr.* **1983**, *15*, 67.
[126] Q. H. Wang, K. Kalantar-Zadeh, A. Kis, J. N. Coleman, M. S. Strano, *Nat. Nanotechnol.* **2012**, *7*, 699.
[127] M. Acerce, D. Voiry, M. Chhowalla, *Nat. Nanotechnol.* **2015**, *10*, 313.

[128] L. Cao, S. Yang, W. Gao, Z. Liu, Y. Gong, L. Ma, G. Shi, S. Lei, Y. Zhang, S. Zhang, R. Vajtai, P. M. Ajayan, *Small* **2013**, *9*, 2905.
[129] S. Ratha, C. S. Rout, *ACS Appl. Mater. Interfaces* **2013**, *5*, 11427.
[130] S. Kück, H. Werheit, *Non-Tetrahedrally Bonded Binary Compounds II*, Springer-Verlag Berlin Heidelberg, **2000**.
[131] S. Ghatak, A. N. Pal, A. Ghosh, *ACS Nano* **2011**, *5*, 7707.
[132] G.-R. Li, Z.-P. Feng, Y.-N. Ou, D. Wu, R. Fu, Y.-X. Tong, *Langmuir* **2010**, *26*, 2209.
[133] J. B. Cook, H.-S. Kim, Y. Yan, J. S. Ko, S. Robbennolt, B. Dunn, S. H. Tolbert, *Adv. Energy Mater.* **2016**, *6*, n/a.
[134] M. A. Worsley, S. J. Shin, M. D. Merrill, J. Lenhardt, A. J. Nelson, L. Y. Woo, A. E. Gash, T. F. Baumann, C. A. Orme, *ACS Nano* **2015**, *9*, 4698.
[135] Z. Tang, Q. Wei, B. Guo, *Chem. Commun.* **2014**, *50*, 3934.
[136] S. Mulik, C. Sotiriou-Leventis, N. Leventis, *Chem. Mater.* **2007**, *19*, 6138.
[137] K. E. Dungey, M. D. Curtis, J. E. Penner-Hahn, *Chem. Mater.* **1998**, *10*, 2152.
[138] V. Pachauri, K. Kern, K. Balasubramanian, *APL Mater.* **2013**, *1*, 32102.
[139] G. Berhault, M. Perez De la Rosa, A. Mehta, M. J. Yácaman, R. R. Chianelli, *Appl. Catal. Gen.* **2008**, *345*, 80.
[140] K. S. W. Sing, *Pure Appl. Chem.* **1985**, *57*, 603.
[141] W.-C. Li, A.-H. Lu, S.-C. Guo, *Carbon* **2001**, *39*, 1989.
[142] A. Ganguly, S. Sharma, P. Papakonstantinou, J. Hamilton, *J. Phys. Chem. C* **2011**, *115*, 17009.
[143] X. Zhang, Q.-H. Tan, J.-B. Wu, W. Shi, P.-H. Tan, *Nanoscale* **2016**, *8*, 6435.
[144] H. Zeng, G.-B. Liu, J. Dai, Y. Yan, B. Zhu, R. He, L. Xie, S. Xu, X. Chen, W. Yao, X. Cui, *Sci. Rep.* **2013**, *3*, DOI 10.1038/srep01608.
[145] C. Lee, H. Yan, L. E. Brus, T. F. Heinz, J. Hone, S. Ryu, *ACS Nano* **2010**, *4*, 2695.
[146] B. E. Conway, *Electrochemical Supercapacitors*, Springer US, Boston, MA, **1999**.
[147] J. R. Miller, P. Simon, *Science* **2008**, *321*, 651.
[148] B. E. Conway, V. Birss, J. Wojtowicz, *J. Power Sources* **1997**, *66*, 1.
[149] J. Zhou, J. Lian, L. Hou, J. Zhang, H. Gou, M. Xia, Y. Zhao, T. A. Strobel, L. Tao, F. Gao, *Nat. Commun.* **2015**, *6*, 8503.
[150] M. A. Bissett, S. D. Worrall, I. A. Kinloch, R. A. W. Dryfe, *Electrochimica Acta* **2016**, *201*, 30.
[151] M. A. Bissett, I. A. Kinloch, R. A. W. Dryfe, *ACS Appl. Mater. Interfaces* **2015**, *7*, 17388.
[152] S. Das, H.-Y. Chen, A. V. Penumatcha, J. Appenzeller, *Nano Lett.* **2013**, *13*, 100.
[153] C. Zhang, A. Johnson, C.-L. Hsu, L.-J. Li, C.-K. Shih, *Nano Lett.* **2014**, *14*, 2443.
[154] K. Hung, C. Masarapu, T. Ko, B. Wei, *J. Power Sources* **2009**, *193*, 944.
[155] L. Jiang, S. Zhang, S. A. Kulinich, X. Song, J. Zhu, X. Wang, H. Zeng, *Mater. Res. Lett.* **2015**, *3*, 177.
[156] K.-J. Huang, L. Wang, J.-Z. Zhang, K. Xing, *J. Electroanal. Chem.* **2015**, *752*, 33.
[157] Y. Liu, W. Wang, H. Huang, L. Gu, Y. Wang, X. Peng, *Chem. Commun.* **2014**, *50*, 4485.
[158] I. Yang, S.-G. Kim, S. H. Kwon, M.-S. Kim, J. C. Jung, *Electrochimica Acta* **2017**, *223*, 21.
[159] K.-K. Kam, Electrical Properties of WSe2, WS2, MoSe2, MoS2, and Their Use as Photoanodes in a Semiconductor Liquid Junction Solar Cell, PhD thesis, Iowa State University, **1982**.

[160] N. H. Basri, B. N. M. Dolah, *Int J Electrochem Sci* **2013**, *8*, 257.
[161] H.-K. Song, Y.-H. Jung, K.-H. Lee, L. H. Dao, *Electrochimica Acta* **1999**, *44*, 3513.
[162] H.-K. Song, H.-Y. Hwang, K.-H. Lee, L. H. Dao, *Electrochimica Acta* **2000**, *45*, 2241.
[163] J. Bisquert, H. Randriamahazaka, G. Garcia-Belmonte, *Electrochimica Acta* **2005**, *51*, 627.
[164] R. H. Friend, A. D. Yoffe, *Adv. Phys.* **1987**, *36*, 1.
[165] Z. Gholamvand, D. McAteer, A. Harvey, C. Backes, J. N. Coleman, *Chem. Mater.* **2016**, *28*, 2641.
[166] P. Y. Chiou, A. T. Ohta, M. C. Wu, *Nature* **2005**, *436*, 370.
[167] A. Jamshidi, P. J. Pauzauskie, P. J. Schuck, A. T. Ohta, P.-Y. Chiou, J. Chou, P. Yang, M. C. Wu, *Nat. Photonics* **2008**, *2*, 86.
[168] P. J. Pauzauskie, A. Jamshidi, J. M. Zaug, S. Baker, T. Y.-J. Han, J. H. Satcher, M. C. Wu, *Adv. Optoelectron.* **2012**, *2012*, e869829.
[169] P. J. Pauzauskie, A. Jamshidi, J. K. Valley, J. H. S. Jr, M. C. Wu, *Appl. Phys. Lett.* **2009**, *95*, 113104.
[170] T.-Z. Shen, S.-H. Hong, J.-K. Song, *Nat. Mater.* **2014**, *13*, 394.
[171] A. Ashkin, J. M. Dziedzic, *Science* **1987**, *235*, 1517.
[172] Y. Liu, D. K. Cheng, G. J. Sonek, M. W. Berns, C. F. Chapman, B. J. Tromberg, *Biophys. J.* **1995**, *68*, 2137.
[173] R. Pethig, Y. Huang, X. Wang, J. P. H. Burt, *J. Phys. Appl. Phys.* **1992**, *25*, 881.
[174] N. J. Rivette, J. C. Baygents, *Chem. Eng. Sci.* **1996**, *51*, 5205.
[175] J. M. Cruz, F. J. García-Diego, *J. Phys. Appl. Phys.* **1998**, *31*, 1745.
[176] M. Esseling, *Photorefractive Optoelectronic Tweezers and Their Applications*, Springer, **2015**.
[177] C. L. H. Devlin, R. L. Ewing, E. A. Guliants, in *NAECON 2014 - IEEE Natl. Aerosp. Electron. Conf.*, **2014**, pp. 357–363.
[178] C. T. O'Konski, *J. Phys. Chem.* **1960**, *64*, 605.
[179] M. P. Hughes, *Nanoelectromechanics in Engineering and Biology*, CRC Press, Boca Raton, **2002**.
[180] C. G. Malmberg, A. A. Maryott, *J. Res. Natl. Bur. Stand.* **1956**, *56*, 1.
[181] B. Standley, A. Mendez, E. Schmidgall, M. Bockrath, *Nano Lett.* **2012**, *12*, 1165.
[182] B. Lin, J. Yu, S. A. Rice, *Phys. Rev. E* **2000**, *62*, 3909.
[183] A. M. J. Davis, *J. Eng. Math.* **1996**, *30*, 239.
[184] J. K. Valley, A. Jamshidi, A. T. Ohta, H.-Y. Hsu, M. C. Wu, *J. Microelectromechanical Syst. Jt. IEEE ASME Publ. Microstruct. Microactuators Microsens. Microsyst.* **2008**, *17*, 342.
[185] F. Vetrone, R. Naccache, A. Zamarrón, A. Juarranz de la Fuente, F. Sanz-Rodríguez, L. Martinez Maestro, E. Martín Rodriguez, D. Jaque, J. García Solé, J. A. Capobianco, *ACS Nano* **2010**, *4*, 3254.
[186] K. Zheng, W. Qin, G. Wang, G. Wei, D. Zhang, L. Wang, R. Kim, N. Liu, F. Ding, X. Xue, T. Jiang, R. Yang, *J. Nanosci. Nanotechnol.* **2010**, *10*, 1920.
[187] A. Jamshidi, S. L. Neale, K. Yu, P. J. Pauzauskie, P. J. Schuck, J. K. Valley, H.-Y. Hsu, A. T. Ohta, M. C. Wu, *Nano Lett.* **2009**, *9*, 2921.
[188] S. Drewniak, R. Muzyka, A. Stolarczyk, T. Pustelny, M. Kotyczka-Morańska, M. Setkiewicz, *Sensors* **2016**, *16*, 103.
[189] K. Erickson, R. Erni, Z. Lee, N. Alem, W. Gannett, A. Zettl, *Adv. Mater.* **2010**, *22*, 4467.

[190] R. Hill, G. Power, *Q. J. Mech. Appl. Math.* **1956**, *9*, 313.
[191] E. Loth, *Powder Technol.* **2008**, *182*, 342.
[192] W. S. Hummers, R. E. Offeman, *J. Am. Chem. Soc.* **1958**, *80*, 1339.
[193] R. Rahman, Low Energy Electrodynamics of Hydrogenated Amorphous Silicon (a-Si:H) Thin Films, PhD thesis, Colorado School of Mines, **2013**.
[194] J. Altet, A. Rubio, *Thermal Testing of Integrated Circuits*, Springer, Boston, **2002**.
[195] F. Favier, E. C. Walter, M. P. Zach, T. Benter, R. M. Penner, *Science* **2001**, *293*, 2227.
[196] R. Griessen, N. Strohfeldt, H. Giessen, *Nat. Mater.* **2016**, *15*, 311.
[197] L. Schlapbach, A. Züttel, *Nature* **2001**, *414*, 353.
[198] L. D'Souza, M. Noeske, R. M. Richards, U. Kortz, *Appl. Catal. Gen.* **2013**, *453*, 262.
[199] Á. Molnár, Ed. , *Palladium-Catalyzed Coupling Reactions: Practical Aspects and Future Developments*, Wiley-VCH Verlag GmbH & Co. KGaA, Wenheim, **2013**.
[200] W. Hong, J. Wang, E. Wang, *Int. J. Hydrog. Energy* **2014**, *39*, 3226.
[201] H. Miyake, T. Okada, G. Samjeské, M. Osawa, *Phys. Chem. Chem. Phys.* **2008**, *10*, 3662.
[202] R. Long, K. Mao, X. Ye, W. Yan, Y. Huang, J. Wang, Y. Fu, X. Wang, X. Wu, Y. Xie, Y. Xiong, *J. Am. Chem. Soc.* **2013**, *135*, 3200.
[203] Y. Yoo, I. Yoon, H. Lee, J. Ahn, J.-P. Ahn, B. Kim, *ACS Nano* **2010**, *4*, 2919.
[204] A. R. Halpern, N. Nishi, J. Wen, F. Yang, C. Xiang, R. M. Penner, R. M. Corn, *Anal. Chem.* **2009**, *81*, 5585.
[205] C. Koenigsmann, A. C. Santulli, E. Sutter, S. S. Wong, *ACS Nano* **2011**, *5*, 7471.
[206] K. J. Jeon, J. M. Lee, E. Lee, W. Lee, *Nanotechnology* **2009**, *20*, 135502.
[207] Y.-H. Chen, H.-H. Hung, M. H. Huang, *J. Am. Chem. Soc.* **2009**, *131*, 9114.
[208] X. Huang, N. Zheng, *J. Am. Chem. Soc.* **2009**, *131*, 4602.
[209] Y. Tang, R. E. Edelmann, S. Zou, *Nanoscale* **2014**, *6*, 5630.
[210] B. Lim, M. Jiang, J. Tao, P. H. C. Camargo, Y. Zhu, Y. Xia, *Adv. Funct. Mater.* **2009**, *19*, 189.
[211] C. Wang, L. Wang, R. Long, L. Ma, L. Wang, Z. Li, Y. Xiong, *J. Mater. Chem.* **2012**, *22*, 8195.
[212] H. Huang, A. Ruditskiy, S.-I. Choi, L. Zhang, J. Liu, Z. Ye, Y. Xia, *ACS Appl. Mater. Interfaces* **2017**, *9*, 31203.
[213] B. Wiley, T. Herricks, Y. Sun, Y. Xia, *Nano Lett.* **2004**, *4*, 1733.
[214] D. K. Smith, N. R. Miller, B. A. Korgel, *Langmuir* **2009**, *25*, 9518.
[215] H. Gabasch, W. Unterberger, K. Hayek, B. Klötzer, E. Kleimenov, D. Teschner, S. Zafeiratos, M. Hävecker, A. Knop-Gericke, R. Schlögl, J. Han, F. H. Ribeiro, B. Aszalos-Kiss, T. Curtin, D. Zemlyanov, *Surf. Sci.* **2006**, *600*, 2980.
[216] J. J. Arcenegui, P. García-Sánchez, H. Morgan, A. Ramos, *Phys. Rev. E* **2013**, *88*, 33025.
[217] B. J. Kirby, *Micro- and Nanoscale Fluid Mechanics: Transport in Microfluidic Devices*, Cambridge University Press, **2010**.
[218] S. M. Shivaprasad, L. A. Udachan, M. A. Angadi, *Phys. Lett. A* **1980**, *78*, 187.
[219] K. Critchley, B. P. Khanal, M. Ł. Górzny, L. Vigderman, S. D. Evans, E. R. Zubarev, N. A. Kotov, *Adv. Mater.* **2010**, *22*, 2338.
[220] T. Bhuvana, G. U. Kulkarni, *ACS Nano* **2008**, *2*, 457.
[221] D. B. Tanner, *Optical Effects in Solids*, Department Of Physics, University of Florida, **2013**.
[222] A. D. Rakić, A. B. Djurišić, J. M. Elazar, M. L. Majewski, *Appl. Opt.* **1998**, *37*, 5271.

[223] L. H. S. Gasparotto, J. F. Gomes, G. Tremiliosi-Filho, *J. Electroanal. Chem.* **2011**, *663*, 48.
[224] Y. Xiong, J. Chen, B. Wiley, Y. Xia, S. Aloni, Y. Yin, *J. Am. Chem. Soc.* **2005**, *127*, 7332.
[225] H. J. Neuburg, *Ind. Eng. Chem. Process Des. Dev.* **1970**, *9*, 285.
[226] K. E. Korte, S. E. Skrabalak, Y. Xia, *J. Mater. Chem.* **2008**, *18*, 437.
[227] Y. Xiong, I. Washio, J. Chen, H. Cai, Z.-Y. Li, Y. Xia, *Langmuir* **2006**, *22*, 8563.
[228] T. Khoperia, T. Zedginidze, *ECS Trans.* **2008**, *13*, 95.
[229] N. Nalajala, A. Chakraborty, B. Bera, M. Neergat, *Nanotechnology* **2016**, *27*, 65603.
[230] P. Zaumseil, *J. Appl. Crystallogr.* **2015**, *48*, 528.
[231] J. Reyes-Gasga, J. L. Elechiguerra, C. Liu, A. Camacho-Bragado, J. M. Montejano-Carrizales, M. Jose Yacaman, *J. Cryst. Growth* **2006**, *286*, 162.
[232] H. Chen, Y. Gao, H. Zhang, L. Liu, H. Yu, H. Tian, S. Xie, J. Li, *J. Phys. Chem. B* **2004**, *108*, 12038.
[233] H. Hofmeister, S. A. Nepijko, D. N. Ievlev, W. Schulze, G. Ertl, *J. Cryst. Growth* **2002**, *234*, 773.
[234] L. Wang, L. Wang, E. Tan, L. Li, L. Guo, X. Han, *J. Mater. Chem.* **2011**, *21*, 2369.
[235] G. S. Y. Yeh, *Pure Appl. Chem.* **1972**, *31*, 65.
[236] N. Pradal, G. Chadeyron, S. Thérias, A. Potdevin, C. V. Santilli, R. Mahiou, *Dalton Trans.* **2013**, *43*, 1072.
[237] J.-F. Zhu, G.-H. Tao, H.-Y. Liu, L. He, Q.-H. Sun, H.-C. Liu, *Green Chem.* **2014**, *16*, 2664.
[238] K. A. Huynh, K. L. Chen, *Environ. Sci. Technol.* **2011**, *45*, 5564.
[239] G. Ertl, R. Hierl, H. Knözinger, N. Thiele, H. P. Urbach, *Appl. Surf. Sci.* **1980**, *5*, 49.
[240] D. Teschner, A. Pestryakov, E. Kleimenov, M. Hävecker, H. Bluhm, H. Sauer, A. Knop-Gericke, R. Schlögl, *J. Catal.* **2005**, *230*, 186.
[241] E. Lundgren, G. Kresse, C. Klein, M. Borg, J. N. Andersen, M. De Santis, Y. Gauthier, C. Konvicka, M. Schmid, P. Varga, *Phys. Rev. Lett.* **2002**, *88*, 246103.
[242] Z. Gu, Z. Xiong, F. Ren, S. Li, H. Xu, B. Yan, Y. Du, *J. Taiwan Inst. Chem. Eng.* **2018**, *83*, 32.
[243] C. Benvenuti, P. Chiggiato, F. Cicoira, Y. L'Aminot, V. Ruzinov, *Vacuum* **2004**, *73*, 139.
[244] B. Wang, H. Idrissi, M. Galceran, M. S. Colla, S. Turner, S. Hui, J. P. Raskin, T. Pardoen, S. Godet, D. Schryvers, *Int. J. Plast.* **2012**, *37*, 140.
[245] J. Wang, Y. Yun, E. I. Altman, *Surf. Sci.* **2007**, *601*, 3497.
[246] P. A. Smith, C. D. Nordquist, T. N. Jackson, T. S. Mayer, B. R. Martin, J. Mbindyo, T. E. Mallouk, *Appl. Phys. Lett.* **2000**, *77*, 1399.
[247] L. V. Redman, A. J. Weith, F. P. Brock, *J. Ind. Eng. Chem.* **1914**, *6*, 3.
[248] S. A. Sojka, R. A. Wolfe, G. D. Guenther, *Macromolecules* **1981**, *14*, 1539.
[249] J. M. Dreyfors, S. B. Jones, Y. Sayed, *Am. Ind. Hyg. Assoc. J.* **1989**, *50*, 579.
[250] J. M. G. Cowie, *Polymers: Chemistry and Physics of Modern Materials, 2nd Edition*, CRC Press, **1991**.
[251] D. Wu, R. Fu, S. Zhang, M. S. Dresselhaus, G. Dresselhaus, *J. Non-Cryst. Solids* **2004**, *336*, 26.
[252] B. B. García, D. Liu, S. Sepehri, S. Candelaria, D. M. Beckham, L. W. Savage, G. Cao, *J. Non-Cryst. Solids* **2010**, *356*, 1620.

[253] H. R. Costantino, A. T.-Y. Chang, B. E. Kron, A. J. Sakshaug, L. A. Thompkins, A. M. Feaver, *Novel Methods for Sol-Gel Polymerization in Absence of Solvent and Creation of Tunable Carbon Structure from Same*, **2014**, US20170015559A1.
[254] J. Biener, S. Dasgupta, L. Shao, D. Wang, M. A. Worsley, A. Wittstock, J. R. I. Lee, M. M. Biener, C. A. Orme, S. O. Kucheyev, B. C. Wood, T. M. Willey, A. V. Hamza, J. Weissmüller, H. Hahn, T. F. Baumann, *Adv. Mater.* **2012**, *24*, 5083.
[255] P. B. Coleman, *Practical Sampling Techniques for Infrared Analysis*, CRC Press, **1993**.
[256] K. A. See, M. A. Lumley, G. D. Stucky, C. P. Grey, R. Seshadri, *J. Electrochem. Soc.* **2017**, *164*, A327.
[257] A. Abdel-Kader, A. A. Ammar, S. I. Saleh, *Thermochim. Acta* **1991**, *176*, 293.
[258] Y. Diao, W. P. Walawender, L. T. Fan, *Bioresour. Technol.* **2002**, *81*, 45.
[259] Y. Li, X. Zhang, R. Yang, G. Li, C. Hu, *RSC Adv.* **2015**, *5*, 32626.
[260] H. Wu, G. Chan, J. W. Choi, I. Ryu, Y. Yao, M. T. McDowell, S. W. Lee, A. Jackson, Y. Yang, L. Hu, Y. Cui, *Nat. Nanotechnol.* **2012**, *7*, 310.
[261] T. D. Hatchard, J. R. Dahn, *J. Electrochem. Soc.* **2004**, *151*, A838.
[262] O. Debieu, R. P. Nalini, J. Cardin, X. Portier, J. Perrière, F. Gourbilleau, *Nanoscale Res. Lett.* **2013**, *8*, 31.
[263] M. Gao, D. Wang, X. Zhang, H. Pan, Y. Liu, C. Liang, C. Shang, Z. Guo, *J. Mater. Chem. A* **2015**, *3*, 10767.
[264] P. Mélinon, P. Kéghélian, B. Prével, V. Dupuis, A. Perez, B. Champagnon, Y. Guyot, M. Pellarin, J. Lermé, M. Broyer, J. L. Rousset, P. Delichère, *J. Chem. Phys.* **1998**, *108*, 4607.
[265] G. Davidson, E. A. V. Ebsworth, G. M. Sheldrick, L. A. Woodward, *Chem. Commun. Lond.* **1965**, *0*, 122b.
[266] A. E. Khalfi, E. M. Ech-chamikh, Y. Ijdiyaou, M. Azizan, A. Essafti, L. Nkhaili, A. Outzourhit, *Spectrosc. Lett.* **2014**, *47*, 392.
[267] A. Cantarero, *Procedia Mater. Sci.* **2015**, *9*, 113.
[268] W. C. Ding, D. Hu, J. Zheng, P. Chen, B. W. Cheng, J. Z. Yu, Q. M. Wang, *J. Phys. Appl. Phys.* **2008**, *41*, 135101.
[269] J. Sun, G. Zheng, H.-W. Lee, N. Liu, H. Wang, H. Yao, W. Yang, Y. Cui, *Nano Lett.* **2014**, *14*, 4573.
[270] J. Yang, M. Xu, J. Wang, S. Jin, B. Tan, *Sci. Rep.* **2018**, *8*, 4200.
[271] A. C. Ferrari, J. Robertson, *Phys. Rev. B* **2000**, *61*, 14095.
[272] P. K. Chu, L. Li, *Mater. Chem. Phys.* **2006**, *96*, 253.
[273] A. C. Ferrari, S. E. Rodil, J. Robertson, *Phys. Rev. B* **2003**, *67*, 155306.
[274] W.-S. Chang, C.-M. Park, J.-H. Kim, Y.-U. Kim, G. Jeong, H.-J. Sohn, *Energy Environ. Sci.* **2012**, *5*, 6895.
[275] Y. Miroshnikov, G. Grinbom, G. Gershinsky, G. D. Nessim, D. Zitoun, *Faraday Discuss.* **2014**, *173*, 391.
[276] J. Zhong, S. Liang, K. Wang, H. Wang, T. Williams, H. Huang, Y.-B. Cheng, *J. Am. Ceram. Soc.* **2011**, *94*, 4025.
[277] A. Kleinová, J. Huran, V. Sasinková, M. Perný, V. Šály, J. Packa, in *Reliab. Photovolt. Cells Modul. Compon. Syst. VIII*, International Society For Optics And Photonics, **2015**, p. 95630U.
[278] V. P. Pshenitsyna, M. V. Kotrelev, *Polym. Sci. USSR* **1969**, *11*, 829.
[279] Q. Wu, B. Shi, J. Bareño, Y. Liu, V. A. Maroni, D. Zhai, D. W. Dees, W. Lu, *ACS Appl. Mater. Interfaces* **2018**, *10*, 3487.

[280] R. Voggu, B. Das, C. S. Rout, C. N. R. Rao, *J. Phys. Condens. Matter* **2008**, *20*, 472204.
[281] S. H. Jeong, J. Y. Koh, T. J. Kim, Y. Jung, *Bull. Korean Chem. Soc.* **2014**, *35*, 2357.
[282] D. S. M. Iaboni, M. N. Obrovac, *J. Electrochem. Soc.* **2016**, *163*, A255.
[283] M. A. Al-Maghrabi, J. Suzuki, R. J. Sanderson, V. L. Chevrier, R. A. Dunlap, J. R. Dahn, *J. Electrochem. Soc.* **2013**, *160*, A1587.
[284] T. Kim, S. Park, S. M. Oh, *J. Electrochem. Soc.* **2007**, *154*, A1112.
[285] M. N. Obrovac, L. Christensen, *Electrochem. Solid-State Lett.* **2004**, *7*, A93.
[286] H. Gao, L. Xiao, I. Plümel, G.-L. Xu, Y. Ren, X. Zuo, Y. Liu, C. Schulz, H. Wiggers, K. Amine, Z. Chen, *Nano Lett.* **2017**, *17*, 1512.
[287] X. H. Liu, L. Q. Zhang, L. Zhong, Y. Liu, H. Zheng, J. W. Wang, J.-H. Cho, S. A. Dayeh, S. T. Picraux, J. P. Sullivan, S. X. Mao, Z. Z. Ye, J. Y. Huang, *Nano Lett.* **2011**, *11*, 2251.
[288] T. Yoon, C. C. Nguyen, D. M. Seo, B. L. Lucht, *J. Electrochem. Soc.* **2015**, *162*, A2325.